The Development of an Average, Anatomically Based, Young Adult, GRIN Eye Model

by

A. David Priest

A thesis
presented to the University of Waterloo
in the fulfilment of the
thesis requirement for the degree of
Master of Science
in
Physics

Waterloo, Ontario, Canada, 2004

Author's Declaration for the Electronic Submission of a Thesis

I hereby declare that I am the sole author of this thesis. This is a true copy of the thesis, including any required final revisions, as accepted by my examiners.

I understand that my thesis may be made electronically available to the public.

Abstract

The purpose of this thesis is to describe the development of an anatomically based, young adult eye model, which includes a crystalline lens with a gradient refractive index (GRIN). This model will then be used to investigate the effect of laser refractive surgery.

The first step in this process involved developing a symmetrical eye model that was found to be a better predictor of empirical longitudinal spherical aberration than any previous model. Myopia was simulated by either a purely axial or refractive technique. While these models were found to be good predictors of the spherical aberration measured in young adults, they did not predict the total amount of high-order aberrations. The techniques used to simulate a single type of myopia caused the myopic models to become anatomically inaccurate.

To improve the eye models a biconic surface was used to quantify the anterior corneal shape as a function of myopia. A method to describe the refractive error and biconic shape parameters in Jackson Cross Cylinder terms was implemented to determine correlations. Results indicate that a biconic accurately models the average shape of the anterior corneal surface as a function of myopia.

Adopting the biconic model for the anterior corneal surface and adding average misalignments of the ocular components transformed the models from symmetrical to asymmetrical. Refractive error was now simulated by the anatomically accurate changes in both the anterior corneal shape and axial length. The asymmetrical aberrations resulted from the misalignment of the ocular components and provided a good prediction of average empirical aberrations but underestimated the aberrations of individual subjects.

Photorefractive keratectomy, a form of laser refractive surgery, was simulated by theoretically calculated and by empirically measured changes in the shape of the anterior corneal surface. Applying the change in anterior corneal shape to the asymmetrical models was used to develop postoperative models. Changes in corneal shape and model aberrations attributed to theoretical calculations do not match empirical observations. The prediction of increased high-order

aberrations in postoperative models based on empirically measured changes in the anterior corneal topography was similar to clinical results.

Average anatomically based, GRIN eye models have been developed that accurately predict the average aberrations of emmetropic and myopic young adults. These models underestimate the asymmetrical and total high-order aberrations that have been measured in individual subjects but are still useful for investigating the average effects of procedures like refractive surgery.

Acknowledgements

This thesis would not have been possible without the empirical, young adult, ocular aberration data and the corneal topography data. The aberration data was measured by Marie-Pierre Paquin, Habib Hamam, and Pierre Simonet at the Université de Montréal and analyzed by Denise King and Juan Manuel Bueno Garcia at the University of Waterloo. Rejean Munger of the University of Ottawa Eye Institute provided the corneal topography data.

Melanie Campbell and Ralph Chou, of the University of Waterloo, spent a considerable amount of time in a joint effort with the author to derive the approximations in Chapter 4 of this thesis, as well as considerable time advising on the approach of the research, methods of data analysis and the content of the thesis.

Along with Ralph Chou and Melanie Campbell, John Vanderkooy of the University of Waterloo comprised my thesis committee and provided comments on the many revisions of this thesis that were produced.

This study was supported in part by a grant to Melanie Campbell from the Natural Sciences and Engineering Research Council of Canada.

Table of Contents

List of Tables

List of Figures

Groningen, 10 November 2003

PHARMACIA

Pharmacia Groningen BV
Van Swietenlaan 5
NL-9728 NX Groningen
P.O. Box 901
NL-9700 AX Groningen
Tel +31 50 5296600
Fax +31 50 5267860
www.pharmacia.com
Bank ABN-AMRO 57.05.69.052

To whom it may concern,

I acknowledge that David Priest would like to use information that appears in the thesis titled "Gradient Index Optical Models and Spherical Aberratic of the Crystalline Lens" and written by Patricia Piers. I hereby grant him permission to reprint any information he deems necessary in his thesis.

Sincerely,

Patricia Piers

Patricia Piers

1 Introduction

For many years modelling has been used as a tool to explore the intricate workings of complex systems. The optical properties and aberrations of the human eye comprise such a system.

Our ability to sense the visual world around us is limited by the optical properties of the eye and its aberrations, particularly at larger pupils. Comprehension of our visual system can only be attained by understanding how light propagates through the eye. An accurate eye model could provide a useful tool to investigate refractive corrections like laser surgery, the process of accommodation and ophthalmoscopy.

The purpose of this thesis is to describe the development of an anatomically based, young-adult, eye model, which includes a crystalline lens with a gradient refractive index (GRIN). The eye model predicts the average, empirical, high-order aberrations as a function of myopia. The main goal for this model is to accurately predict aberrations. The model is considered to be anatomically-based since average, age-dependent empirical values are used to represent the shape, size and refractive index of its optical components whenever possible. The model will also be used to investigate laser refractive surgery.

A brief background is provided in Chapter 2 that describes aberration theory, the classification and quantification of aberrations, the optical components of the human eye and refractive error.

The modelling process is initiated in Chapter 3, where a young-adult, GRIN crystalline lens model and emmetropic symmetrical eye model, based on the work by Piers (1997) are developed. Myopia was then simulated by either purely axial or refractive techniques. The model's predicted aberrations and the empirical results from a group of emmetropic and myopic young adults were quantified with Zernike polynomials and compared.

To improve the symmetrical eye models, an accurate, asymmetrical model of anterior corneal shape, as a function of myopia, was required. Chapter 4 describes how a biconic surface was utilized to quantify the anterior corneal shape of 206 eyes. A method to describe the refractive error and

biconic shape in Jackson Cross Cylinder terms was implemented to enable the determination of correlations between metrics describing corneal topography and refraction.

In Chapter 5, the symmetric model evolves to asymmetric by adopting the biconic model of the anterior corneal surface and misaligning the ocular components by average, empirically determined values. Since the shape of the anterior corneal surface became a function of myopia, the model's axial length was used to control refractive error. Two asymmetrical models were developed to investigate the effect of corneal asymmetry. In these models, the anterior corneal surface was modeled with either a symmetrical conic or a biconic with an average amount of asymmetry. Average aberration metrics quantifying spherical aberration, coma and high-order aberrations were calculated by two techniques. The first method involved calculating the aberration metrics for each individual model or subject and then averaging across individuals. In the second method, average Zernike terms were determined before calculating the aberration metrics. Model results were compared with empirical data.

The asymmetrical model was utilized, in Chapter 6, to investigate laser refractive surgery. This procedure alters ocular aberrations by changing the shape and thickness of the cornea and was modelled by modifying the symmetrical conic cornea of the asymmetrical model. Corneal changes were simulated from both theorectical calculations (Munnerlyn, et al., 1988) and empirical measurements. Theoretical calculations were used to determine the desired depth of tissue to be removed at a point on the cornea (ablation pattern) as a function of preoperative refractive error and paraxial power of the anterior corneal surface. The postoperative cornea model was created by subtracting the ablation pattern from the preoperative cornea and quantified by the best-fit conic surface. Empirical, surgically induced changes in corneal shape were determined, as a function of preoperative refractive error, by comparing pre and postoperative topographies of the anterior corneal surface in 125 eyes that were quantified with Jackson Cross Cylinder terms. Postoperative aberrations predicted by the models were compared to empirical results.

2 Background

2.1 Aberration Theory

In geometrical optics two associated conventions, rays and wavefronts are used to describe the propagation of light waves. These concepts are defined by recalling that light travels with a constant velocity within a medium of constant refractive index (Welford, 1986). Following Welford, Chapter 2, changes in direction and speed occur when light waves encounter a change in refractive index. Rays define the path along which the light quanta travel. The time it takes light to travel from A to B is defined as,

$$t_{AB} = \frac{1}{c}\int_{A}^{B} n \quad ds \tag{2.1}$$

The integration is performed along a ray path, where ds is a distance element along the path in a medium with refractive index n and c is the speed of light in a vacuum. If n were constant between A and B then

$$t_{AB} = \frac{nAB}{c} \tag{2.2}$$

where AB is the length of the line segment between A and B.

The quantity $\int n\, ds$ defines an optical path length (OPL) (Welford, 1986). A wavefront is a surface of constant optical path length from a source point. It corresponds to a surface of constant phase and demonstrates how far light has traveled from its source in a given time. In a homogeneous medium, wavefronts radiate outward in spherical shapes that are concentric to the source. This shape is maintained until a change in the refractive medium is encountered. Rays from a source are orthogonal to the corresponding wavefront and represent normals to the wavefront surface.

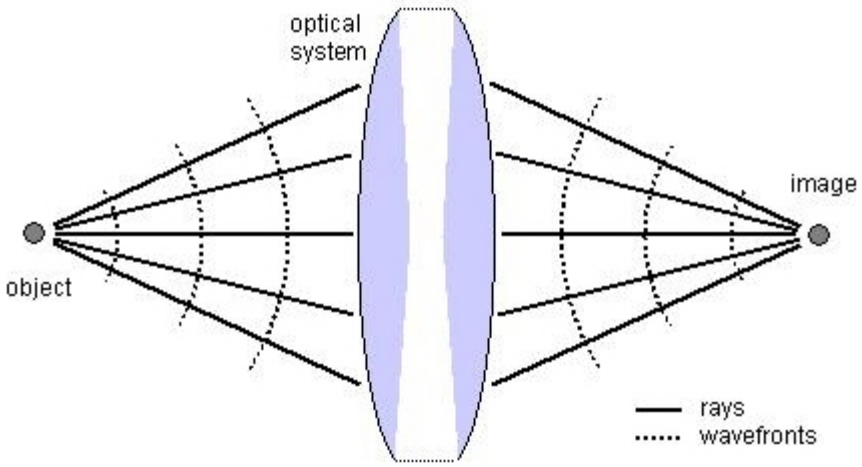

Figure 2.1: Rays and Wavefronts in an Ideal System.

A perfect image is defined such that its light distribution has the same form as that of the object. The only difference would be a change in size or orientation due to the magnification of the imaging system. An ideal image is formed when all the rays from an object point that are redirected by a perfect optical system are concurrent at a single image point. The redirected wavefronts maintain a spherical shape and become concentric about the image point. All portions of these wavefronts will converge simultaneously to the image point (Figure 2.1).

In a real optical system, the relative light distribution in image space is not identical to that in object space. The difference between these two light distributions is referred to as blur and is caused by aberrations, scatter and diffraction.

Diffraction is a spatial redistribution in the irradiance of a wave resulting from the presence of an object that alters the amplitude or phase of the wave. This causes light at the edge of a beam to be deflected out of the beam. Consequently, light in a point image tends to spread out and the amount of spread increases with decreasing width of the beam and increasing wavelength (Smith and Atchison, 1997). Diffraction provides a limit as to how good an optical system can become.

Aberrations are defined as factors that also cause the light from a point object to be imaged as a blurred spot. These effects can be explained as a distortion of the wavefonts from their initial spherical shape, the perfect wavefront, or as a departure of the rays from their ideal paths.

Aberrations are investigated by tracing real rays through the optical system and then comparing their paths and the resulting wavefront shape to those from an ideal system. The mathematical theory of aberrations shows that aberrations may be classified into different types that lead to distinct patterns in the light distribution of an image. The following sections will classify different types of aberrations and describe the mathematical theory used to quantify them.

2.1.1 Classification of Optical Aberrations

The classification of aberration types begins by dividing them into either monochromatic or chromatic aberrations. Monochromatic aberrations are associated with light that is composed of a single wavelength. Chromatic aberrations occur only in polychromatic light and are due to the dispersion of the optical medium. Since the investigations within this thesis were performed for monochromatic light, the topic of chromatic aberrations will not be discussed.

Monochromatic aberrations refer to the distinctive light patterns found in an image formed in monochromatic light. For low levels of aberration, several distinct types, referred to as Seidel or primary aberrations, have been defined (Smith and Atchison, 1997). These primary aberrations will be described by how they affect ray paths at different locations within the system aperture.

2.1.1.1 Defocus

In an ideal optical system, a perfect image can be observed at the focal plane. If diffraction and scatter are ignored and the image plane does not coincide with the focal plane then the corresponding image will be evenly blurred. In this case the optical elements have an excess or lack of refractive power for the position of the image plane. If defocus were the only type of aberration present in the system, then the wavefronts in image space would be spherical but would not be centred at the image plane. Historically, defocus has not been considered an aberration since most optical systems are built to produce a focused image on the image plane. Unfortunately the human eye does not always develop into a focused system. Consequently, defocus will be an important aberration throughout this thesis.

2.1.1.2 Spherical Aberration

Spherical aberration (SA) is a variation in focal power with radial distance from the optical axis. Consequently, rays positioned progressively farther from the optical axis within the system's aperture, focus progressively farther away or closer to the system aperture from where the central rays focus. This aberration can be interpreted as an excess or lack of peripheral refractive power, which creates a symmetrical blur halo around a point image. Figure 2.2 displays excess peripheral power causing rays to focus closer to the optical elements as ray height from the optical axis increases. When a system has more power peripherally its corresponding SA is termed undercorrected or positive. Conversely, if a system has less power peripherally then its SA is referred to as overcorrected or negative. The shape of the refractive surfaces, object position and distribution of refractive indices within an optical system all contribute to its SA. Aside from the possibility of some defocus, SA is the only aberration present in an axially symmetric optical system where:

a) refractive surface shapes are rotationally symmetrical,

b) all optical elements are centered along and perpendicular to the optical axis and

c) the object is also on-axis.

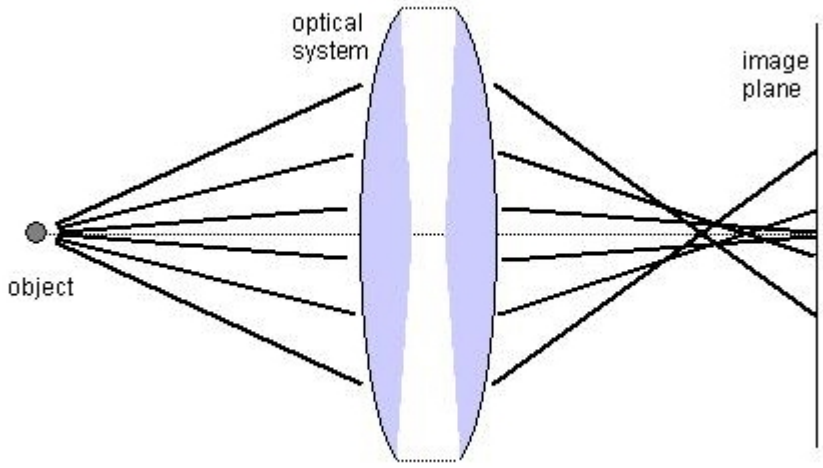

Figure 2.2: Positive Spherical Aberration

2.1.1.3 Coma

Coma is a variation of magnification with radial distance of incident rays from the optical axis. Rays at farther radial distances from the optical axis will image farther from where the central rays image. Figure 2.3 displays how this aberration blurs a point object into an asymmetrical comet-shaped image. Objects imaged through an axially symmetric system will only be affected by coma if they are positioned off-axis. Images of both on and off-axis objects will be affected by coma when they are formed through an asymmetrical optical system where:

a) the refractive surfaces have asymmetrical shapes or

b) the optical elements are misaligned with respect to the optical axis

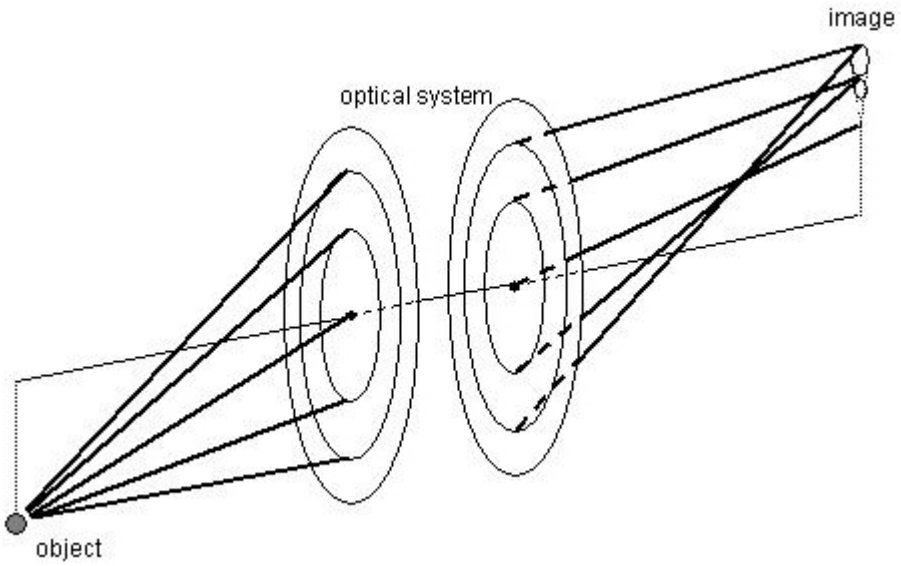

Figure 2.3: Coma (modified from Smith and Atchison, 1997)

2.1.1.4 Astigmatism

A light beam can be described as a set of ray fans where each fan has a different angular orientation within the system aperture. Astigmatism creates an angular variation in focus such that each individual ray fan focuses at a different point along the optical axis. The focal range along the optical axis is called the interval of Sturm. Its end points are the foci from two orthogonal ray fans representing the lowest and highest power. The remaining fans focus along the interval of Sturm.

Astigmatism creates a blurred image where the shape of the blur depends on the location of the image plane. When the image plane is located at one of the ends of the interval of Sturm, the image of a point object will be a line perpendicular to the focused ray fan. Point objects imaged elsewhere will appear elliptical or circular. The size and orientation of the elliptical blur changes with the position of the image plane. The blur is minimized at a point within the interval of Sturm, where it is circular. This location is called the circle of least confusion. Figure 2.4 displays the effect of astigmatism on a point object. Astigmatism affects all off-axis points but only affects on-axis points if the refracting surfaces are asymmetrical or misaligned from the optical axis.

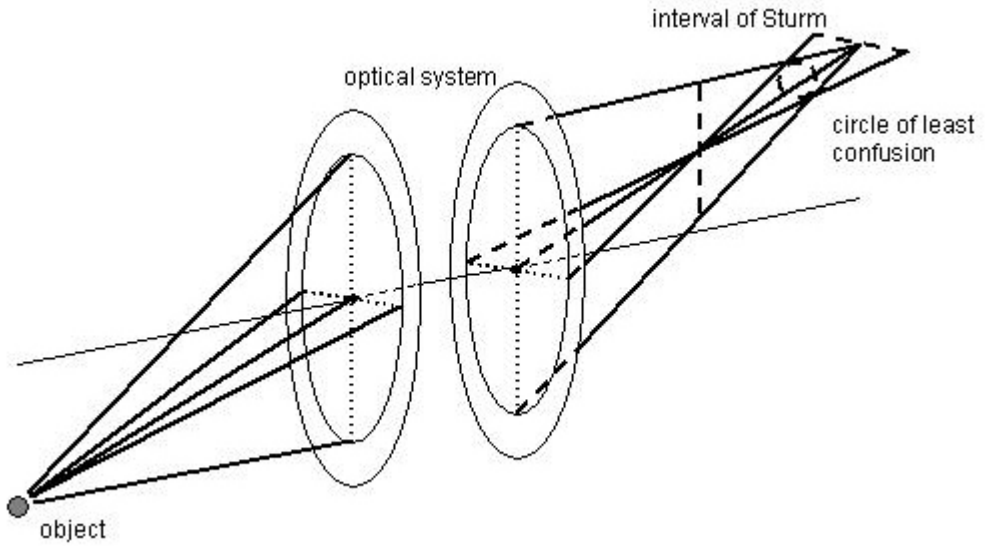

Figure 2.4: Astigmatism

2.1.1.5 Field Curvature

Field curvature causes extended objects to focus on a curved surface instead of a flat image plane. Every optical system suffers from field curvature, which is a function of the optical elements' refractive index and their surface curvatures (Smith, 2000). The image surface is called the Petzval surface and it is almost spherical near the optical axis. If a flat image surface is positioned to focus an on-axis point then the image of off-axis points will have circular blur because they are defocused at this plane. The level of defocus will increase with the distance of the point off-axis. Field curvature can be corrected with the right combination of surface shapes and refractive indicies (Smith, 2000). In some optical systems, the object or image recording surface is curved to compensate for field curvature (Smith and Atchison, 1997).

2.1.1.6 Distortion

Distortion is a variation in the system magnification across the object field. The farther a point is off-axis the larger the change in magnification. When the magnification increases with off-axis position the distortion is termed positive or pincushion distortion. When the magnification decreases it is called negative or barrel distortion. Figure 2.5 displays the effect of these two types of distortion on the image of a square.

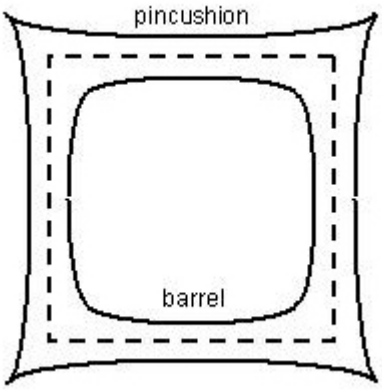

Figure 2.5: Distortion of a Square (modified from Smith and Atchison, 1997)

2.1.2 Quantification of Optical Aberrations

Aberrations are quantified by describing the error of specific rays. The rays are defined by their position within a system aperture. Various representations are used to describe the amount of error. These include longitudinal aberrations (LA), transverse aberrations (TA) and wave aberrations (W) (Figure 2.6).

2.1.2.1 Longitudinal Aberrations

The longitudinal aberration (LA) of a ray is the distance between the point where the ray intersects the optical axis in image space and the image plane.

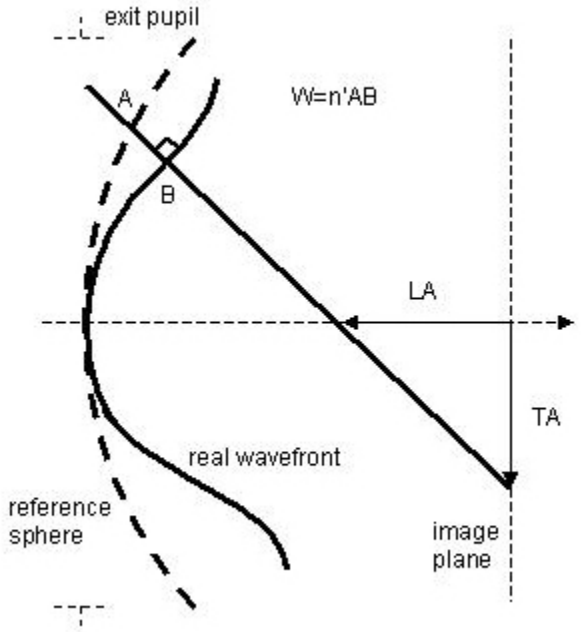

Figure 2.6: Aberration Types

2.1.2.2 Transverse Aberrations

The transverse aberration of a ray is the distance between where the ray and the optical axis intersect the image plane. Generally this distance is split into components of the corresponding coordinate system.

2.1.2.3 Wave Aberrations

The wave aberration (W) of a ray is the difference in optical path length from object to image, between the ray and an unaberrated ray. The unaberrated ray, known as the principal, chief or pupil ray, is the ray from any object point that passes through the centre of the system's entrance pupil (Born and Wolf, 1999). In Figure 2.6, W is the optical path length between point A and point B. The optical path difference (OPD) is currently the conventional technique used to measure aberrations and will be used predominately throughout the remainder of this thesis.

2.1.2.4 Wave Aberration Function and Zernike Polynomials

Aberrations affect a wavefront by distorting its shape as it passes through the optical system. The wave aberration is a measure of this distortion. If the ideal, undistorted, spherical wavefront at the exit pupil that is centred on the ideal image point is used as a reference sphere, then W is the optical path length along the ray between this reference sphere and the corresponding distorted wavefront (Figure 2.6).

W is generally different for different rays from the same object point and for different object points with the same position in the exit pupil. Therefore, the wave aberration is a function of the coordinates of the intersection point of the ray within the exit pupil ($W(x,y)$ or $W(r,\theta)$). The ray positions within the entrance pupil can also be used.

W varies smoothly between rays and therefore can be described as a power series expansion of ray position. Originally Taylor polynomials were used to describe wave aberrations but recently

various representations using Zernike polynomials have become popular. To avoid confusion, a specific set of Zernike polynomials has been proposed as the standard to be used in subsequent vision research (Thibos, et al., 2002). This convention will be described subsequently and used throughout the remainder of this thesis.

Following Thibos, et al., (2002), the Zernike polynomials are a set of functions that are orthogonal over the unit circle. They are useful for describing the error of an aberrated wavefront for an optical system with a circular pupil. Zernike polynomials are usually defined in polar coordinates (r,θ), where r is the radial coordinate ranging from 0 to 1 and θ is the azimuthal coordinate ranging from 0 to 2π. Each of the Zernike polynomials (Z) consists of three components: a normilization factor (N), a radial-dependent polynomial (R) and an azimuthal–dependent sinusoidal. A double indexing scheme is used for describing these functions, with the index n describing the highest order of the polynomial component and the index m describing the frequency of the sinusoidal component. By this scheme the Zernike polynomials are defined in equations 2.3, 2.4 and 2.5.

$$Z_n^m(r,\theta) = \begin{cases} N_n^m R_n^{|m|}(r)\cos(m\theta) & m \geq 0 \\ -N_n^m R_n^{|m|}(r)\sin(m\theta) & m < 0 \end{cases} \qquad 2.3$$

$$R_n^{|m|}(r) = \sum_{s=0}^{(n-|m|)/2} \frac{(-1)^s (n-s)!}{s![0.5(n+|m|-s]![0.5(n-|m|-s]!} r^{n-2s} \qquad 2.4$$

$$N_n^m = \sqrt{\frac{2(n+1)}{1+\delta_{m0}}} \qquad 2.5$$

δ_{m0} is the Kronecker delta function (ie. $\delta_{m0}=1$ for $m=0$, and $\delta_{m0}=0$ for $m\neq 0$). It should also be noted that the value of n is a positive integer or zero and for a given n, m can only take on values of -n, -n+2, -n+4, … n. Considering this definition the first 15 Zernike terms are displayed in Table 2.1 along with the name of their corresponding primary aberration.

Table 2.1: Listing of Zernike Polynomials inclusive to the 4th order

order (n)	frequency (m)	$Z_n^m(r,\theta)$	Aberration
0	0	1	
1	-1	$2r\sin\theta$	
1	1	$2r\cos\theta$	
2	-2	$\sqrt{6}r^2\sin 2\theta$	45° astigmatism
2	0	$\sqrt{3}(2r^2-1)$	defocus
2	2	$\sqrt{6}r^2\cos 2\theta$	0° astigmatism
3	-3	$\sqrt{8}r^3\sin 3\theta$	
3	-1	$\sqrt{8}(3r^3-2r)\sin\theta$	vertical coma
3	1	$\sqrt{8}(3r^3-2r)\cos\theta$	horizontal coma
3	3	$\sqrt{8}r^3\cos 3\theta$	
4	-4	$\sqrt{10}r^4\sin 4\theta$	
4	-2	$\sqrt{10}(4r^4-3r^2)\sin 2\theta$	
4	0	$\sqrt{5}(6r^4-6r^2+1)$	spherical aberration
4	2	$\sqrt{10}(4r^4-3r^2)\sin 2\theta$	
4	4	$\sqrt{10}r^4\sin 4\theta$	

2.1.2.5 Image Quality Criteria

Image quality criteria are used to assess how faithfully an optical system can image an object, apart from distortion. These criteria are related to the image's irradiance, which is a measure of light flux density. An image's irradiance is an important aspect of image quality since the brightness (physiological perception of irradiance) of the image is related to the ability to perceive its detail.

Geometrical optics predicts that the image of a point object focussed by an optical system with no aberrations will have infinite irradiance at the paraxial focus and zero irradiance elsewhere. Diffraction theory has shown that the real image consists of a bright central area surrounded by bright and dark rings (Airy pattern) and it provides a limit to the irradiance of the central area. In the presence of aberrations, the central peak irradiance is generally expressed as the fraction of the diffraction limit. When normalized this ratio is known as the Strehl intensity (Born and Wolf, 1999) or Strehl ratio.

Without diffraction theory, aberrations do not provide image quality information directly but they can be used to calculate some criteria. The derived criteria are usually the result of reducing a complex multi-dimensional function to a single number on a suitable scale. When using a wave aberration function the common reduction is to calculate the root-mean-square (RMS) of the wavefront error.

The RMS of a wave aberration function is a measure of the variance of the wavefront error within the pupil. When $W(r,\theta)$ is expressed with Zernike polynomials then the RMS can be calculated by

$$\mathrm{RMS} = \sqrt{\left[\int_0^{2\pi}\int_0^{1} W^2(r,\theta)\, r\, dr\, d\theta \Big/ \pi\right] - \left[\int_0^{2\pi}\int_0^{1} W(r,\theta)\, r\, dr\, d\theta \Big/ \pi\right]^2} \qquad 2.6$$

It has been shown (Smith and Atchison, 1997; Born and Wolf, 1999) that the Strehl ratio (E) of an optical system is related to the RMS of its wavefront error by

$$E \approx 1 - (2\pi/\lambda)^2 (\mathrm{RMS})^2 \qquad 2.7$$

Equation 2.7 shows that the RMS can be used as an image quality criterion, since the Strehl ratio is smaller than the ideal value by an amount proportional to the root-mean-square wavefront error (Born and Wolf, 1999). It also shows that the image irradiance is normalized to one when the RMS equals zero, which represents an aberration free system.

The relationship between the Strehl ratio and the RMS of the wavefront error is only valid for ratio values greater than 0.8 (Smith and Atchison, 1997). Wavefront aberrations in both eyes of 59 normal young adults (average age of 24 years) have been measured with a near-IR (784 nm) Hartmann-Shack aberroscope (Castejon-Mochon, et al., 2002). The average RMS of the wavefront error fit by high-order Zernike terms (>2^{nd} order) was found to be 0.15 μm for a 5 mm pupil. Considering equation 2.7, the measured RMS in this population would need to be less than 0.06 μm for the relationship between Strehl ratio and RMS to be valid. While the RMS of the wavefront error in the human eye is too large to relate it quantitatively to the Strehl ratio, it is qualitatively known that systems with larger wavefront error will produce worse image quality and RMS is still a useful metric for describing the overall size of the wavefront error.

2.2 The Human Eye as an Optical Element

The human eye is a complex optical system. Its main anatomical features are depicted in Figure 2.7. The shape, position and refractive index of these structures, described in the following sections, provide the eye with its unique imaging capabilities.

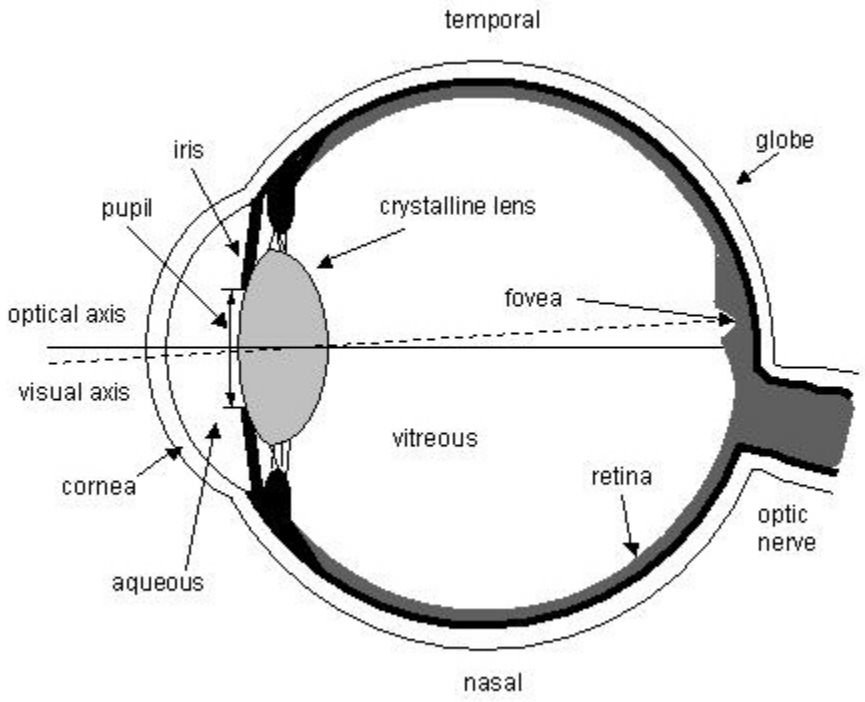

Figure 2.7: Optical Components of the Human Eye (modified from Kolb, et al., 2002)

2.2.1 Cornea

The cornea is the transparent tissue that acts as the window to the eye. It is composed of three main layers. These include the epithelium, stroma, and endothelium. Corneal thickness ranges from about 0.5 mm centrally to 0.7 mm on the periphery and consists mostly (~90%) of stroma. A thin coating of tear film covers the external corneal surface and serves to maintain the smoothness of the optical surface (Charman, 1991b).

The refractive index of the cornea has been determined to be 1.376 (Bennett and Rabbetts, 1989). Due to the large change in refractive index between air and cornea, its anterior surface makes the greatest contribution to the overall power of the eye (~60%). Corneal shape is consequently of great interest with regard to its role in determining the aberration of retinal images.

The shape of the cornea or any surface can be expressed as the perpendicular distance of surface points from a reference plane (Figure 2.8). These distances are referred to as the sag or elevation of the surface at that particular point. Surface shape can then be described by the parameters of various known shapes, whose sag best fits the surface's sag.

Describing the corneal surface with a sphere will provide an overall, average description of its shape. Spherical sag (Z_s) at a point with polar coordinate r is commonly defined by

$$Z_S(r) = R - \sqrt{R^2 - r^2} \qquad 2.8$$

where R is the radius of curvature of the spherical surface.

The radius of curvature of most corneas does not stay constant across the surface as it does for a spherical surface. Corneal curvature tends to either steepen or flatten for points radially farther from the apex. A more flexible description uses a conic shape that accounts for the possible changing curvature. Conic sag (Z_C) is commonly defined (Smith and Atchison, 1997) by

$$Z_C(r) = \frac{R - \sqrt{R^2 - (1+Q)r^2}}{1+Q} \qquad 2.9$$

R is the apical radius of curvature measured from the centre of curvature to the vertex (Figure 2.8). Q is the asphericity, which quantifies how the radius of curvature changes. When Q equals zero equation 2.9 simplifies to equation 2.8 and the defined shape is spherical. When $Q < 0$ the peripheral curvature is flatter than the central curvature and is termed prolate. When $Q > 0$ the peripheral curvature is steeper than the central curvature and is termed oblate (Figure 2.8).

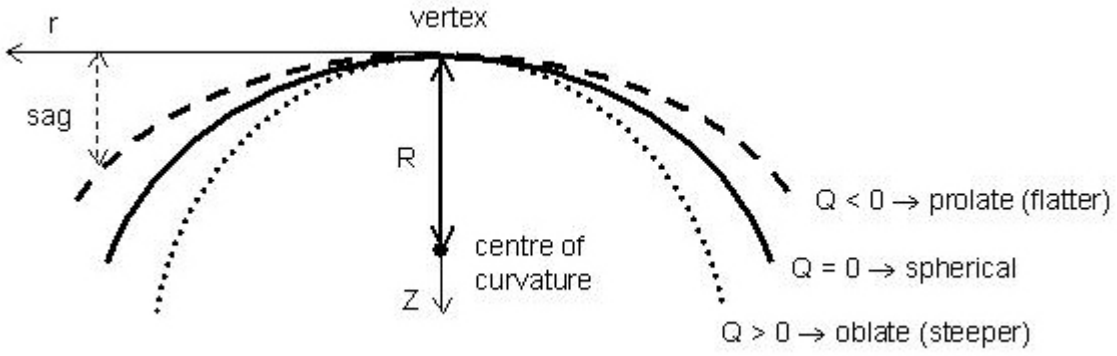

Figure 2.8: Conic surfaces

Conic sag can also be expressed as

$$Z_C(r) = \frac{r^2}{R + \sqrt{R^2 - (1+Q)r^2}} \qquad 2.10$$

While equation 2.9 is not calculable when Q= -1, equation 2.10 is always calculable and is therefore preferred for numerical calculations (Smith and Atchison, 1997).

Besides asphericity, a number of other quantities have been used to describe the radial change in curvature. These quantities are the conic constant (K), eccentricity (e) and the shape factor (p). The relationship between these quantities and the asphericity is

$$Q = K = -e^2 = p - 1 \qquad 2.11$$

Most attempts to model the cornea have utilized symmetric surfaces, but in reality, the cornea is an irregular, aspherical surface that is not rotationally symmetric. A more extensive description of corneal shape will be given in Chapter 4.

2.2.2 Aqueous Humour

Behind the cornea is the anterior chamber, which is filled with a transparent liquid called the aqueous humour. Its refractive index has been found to be approximately 1.337.

The depth of the anterior chamber is defined as the distance, measured along the eye's optical axis, from the posterior vertex of the cornea to the anterior surface of the crystalline lens, although the term anterior chamber depth sometimes includes the thickness of the cornea (Bennett and Rabbetts, 1989). This is usually the case when measurements are made with A-scan ultrasonography, which cannot resolve the posterior corneal surface. Due to a corresponding increase in the thickness of the crystalline lens, the depth of this chamber reduces throughout adult life (Charman, 1991b). An average, age-independent value of anterior chamber depth excluding corneal thickness would be 3.0 mm (Bennett and Rabbetts, 1989).

2.2.3 Pupil

The pupil is a circular opening in the iris, lying approximately tangential to the anterior lens surface. It plays the important role of aperture stop in the optical system of the eye. Consequently its contribution to the retinal image includes controlling the light flux as well as affecting image quality through its influence on diffraction, aberrations and ocular depth of focus (Charman, 1991b).

It has been determined that the major physiological role of the pupil is to control retinal illumination. The pupil diameter varies as function of the ambient lighting but is also affected by factors like age, accommodation, emotion and medication.

The pupil is not centred with respect to the rest of the eye's components and is often displaced nasally (Liou and Brennan, 1997). Research into pupil centration has revealed that it changes with changes in illumination and pupil size (Walsh, 1988; Wilson, et al., 1992). Because of the various aberrations of the eye, investigations into the effect of pupil centration and diameter on ocular optical performance found that decentration caused relatively little difference at smaller pupil sizes, while it could produce marked degradations for larger pupil sizes (Walsh and Charman, 1988).

2.2.4 Crystalline Lens

The purpose of the crystalline lens is to provide the remaining refractive power necessary to dynamically focus objects located at different distances from the eye. Through the act of accommodation, lens power is increased to enable near objects to be focused on the retina. This is accomplished by changes in lens shape, thickness, refractive index distribution and position within the globe. There are physical limits to how much these parameters can change, which provide upper and lower limits to the equivalent power of the lens and eye. The resulting range of object positions, which can be focussed clearly onto the retina, is known as the amplitude of accommodation.

The lens is composed of fine fibres stretched from the anterior to posterior pole. While retaining old fibres, the lens continues to grow throughout life by the addition of new lens fibres originating at the lens equator. Consequently the shape and size of the lens is continually changing (Charman, 1991b). The amplitude of accommodation is also affected by age. It decreases throughout life until the ability to accommodate by changing lens power is lost around the age of 50 years.

A modified form of slit lamp photography has been used to measure the shape of the lens surfaces. Results indicate that the curvature of both the anterior and posterior surfaces increase with age (Brown, 1974; Dubbelman and van der Heijde, 2001).

A farther consequence of lens growth is that the central region or nucleus of the lens is older than the outer layer or cortex. The highest refractive index (~1.41) is found in the nucleus while the lowest (~1.38) is in the cortex. The lens is a gradient-index (GRIN) optical component and its

properties cannot be fully described by classical eye models that assume homogeneity of the lens medium (Charman, 1991b).

Experimental and theoretical techniques, which were originally developed to study the index distributions in GRIN optical fibres, have been applied to human lenses. One of the more powerful techniques involves studying the deflection of a thin laser beam as it passes through the lens at different locations. Results have been used to determine the GRIN distributions (Campbell, 1984) and focal length and longitudinal spherical aberration of excised lenses. This technique has shown that the focal length increases linearly with age and the magnitude and sign of the spherical aberration change with age and accommodation (Glasser and Campbell, 1998). This information is then used to compute the refractive index distribution based on assumptions regarding the latter's form and symmetry (Piers, 1997).

The internal refractive index structure of *in vitro* human lens has also been investigated by analysing the path of a laser beam (ray tracing) (Pierscionek and Chan, 1989). This method can be accurately applied only to a lens with a circular cross-section and consequently only the refractive index distribution in the equatorial section of human lenses could be measured (Smith, 2003).

Reflectometry has also been used to measure the refractive index of *in vitro* human lenses. Measurements have been made with both an Abbe reflectometer (Piers, 1997; Clarke, et al., 1998) and a reflectometric fibre optic sensor (Pierscionek, 1994, 1997).

Magnetic resonance imaging (MRI) has also been utilized to determine the refractive index of *in vitro* human lenses (Moffat, et al., 2002). Although it is time consuming, costly and currently has limited resolution, the MRI technique holds the most promise for measuring the refractive index at any spatial location within an *in vivo* human lens (Smith, 2003).

2.2.5 Vitreous

The space between the lens and retina is filled with a transparent gel known as the vitreous. It has a refractive index of approximately 1.336 and tends to liquefy throughout adulthood. Optically, the vitreous body in the young is almost clear and free of refractive irregularities, but these can become more prevalent during old age (Charman, 1991b).

2.2.6 Retina

Anatomically, the retina is composed of thin layers of neural tissue that lines the posterior portion of the globe (Vaughan, et al., 1999). Within the retina is a layer of specialized cells, known as receptors, which transform light into electrical impulses. The nerve fibre layer transmits the impulses to the brain via the optic nerve. The retina's ability to distinguish detail is governed by the density of receptor cells. This density is not uniform over the entire retinal surface and reaches a maximum in the macular region. The macula is an approximately circular region of about 1.5 mm diameter containing a smaller central area called the fovea. It is at the fovea that the eye attains its maximum resolving power. When an eye fixates on an object the image lies on the fovea.

Optically, the retina plays the role of the imaging screen. It can be regarded as a spherical surface with a radius of curvature in the neighbourhood of 12 mm. The curvature of the retina gives it two main advantages over the flat image planes used in most optical instruments. First, the curved retina is better suited for the curved image plane created by most optical systems. Secondly the curved retina is able to cover a much wider field of view (Bennett and Rabbetts, 1989).

2.2.7 Optical Axis, Visual Axis and the Line of Sight

The centres of curvature of reflecting or refracting elements in a conventional centred system are co-linear. This line is the optical axis (Atchison and Smith, 2000). The optical surfaces of the eye may lack rotational symmetry. Their nominal centres of curvature may not lie on a common axis and the pupil centre may also be displaced. These various decentrations, asymmetries and tilts are small in most eyes and a nominal optical axis can be identified. By itself, the nominal optical axis is of no specific importance but is useful as a reference for some other axes of the eye (Atchison and Smith, 2000). The line passing through the centres of curvature of the front surface of the cornea and the back surface of the lens can be used to approximate the nominal optical axis (Le Grand and El Hage, 1980). This optical axis does not in general intersect the retina at the fovea. The intersection is found approximately 1.5 mm nasal and 0.5 mm superior to the fovea (Charman, 1991b).

Another axis, known as the visual axis, is defined as 2 parallel lines passing from the fixation point to the eye's first nodal point and from the second nodal point to the fovea. This axis is a convenient reference for visual functions since it does not depend on pupil size (Atchison and Smith, 2000). Its use has been criticized since a ray along the visual axis is not centred on the pupil and would not be the chief ray of the beam passing into the eye from the fixation target (Bennett and Rabbetts, 1989).

Close to the visual axis is another axis called the line of sight. It is defined as the line joining the fixation point and the centre of the entrance pupil. The direction of this axis is not fixed since the pupil centre may fluctuate with pupil size. This axis is very important for defining visual function since it defines the centre of the beam of light (chief ray) entering the eye (Atchison and Smith, 2000). Aberration measurements of the eye are referenced to the line of sight.

Generally, the angle between the optical axis and the line of sight defined above is called angle alpha (α) (Bennett and Rabbetts, 1989; Atchison and Smith, 2000). Since the method of measuring this angle (see Chapter 5) involves the subject fixating on a target, it may be more accurate to consider that angle alpha defines the position of the line of sight rather than the visual axis (Atchison and Smith, 2000). Typically α takes a value of about 5° in a nasal inferior direction (Charman, 1991b).

2.2.8 Refractive Error

An unaccommodated eye is properly focussed if it brings parallel rays from a distant object to a sharp focus on the retina. Such an eye is said to be emmetropic. If an eye is not emmetropic, it possesses refractive error and is termed ametropic. Ametropia is an optical defect introducing defocus and it is reasonable to assume that it can be corrected by an optical means such as spectacles or refractive surgery.

Ametropia is described by dividing it into spherical ametropia and axial astigmatism. An eye with spherical ametropia focuses images at a plane that is not coincident with the retina. Consequently, the axial length of the eye and its focal length are mismatched.

If the image plane is in front of the retina the resulting refractive error is referred to as myopia (Figure 2.9). The myopic eye can be regarded as having too much optical power for its axial length. For images to be focused on the retina, light from the object must reach the eye in a state of divergence. Without any means of optical correction, only objects at a finite distance from the eye will be well focussed. This distance is inversely proportional to the size of the refractive error in dioptres. The point conjugate with the fovea of the unaccommodated eye is called the far point. Accommodation allows a myope to focus objects at a shorter distance from the eye than the far point but not objects beyond it.

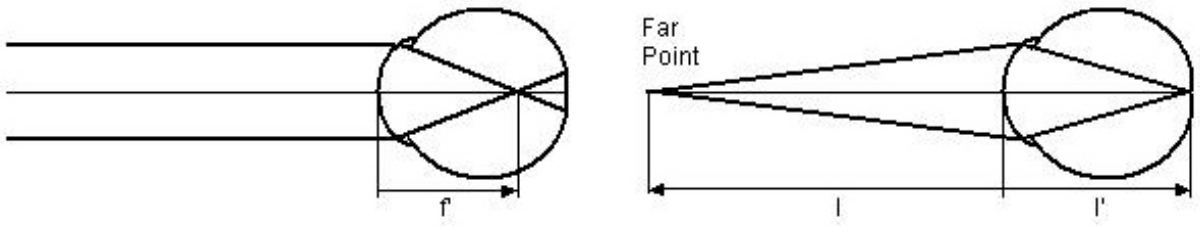

Figure 2.9: Myopia

Hyperopia is the condition where rays within the eye are intercepted by the retina before reaching focus (Figure 2.10). The unaccommodated hyperopic eye does not possess enough power for its axial length. The far point is situated behind the eye and is thus a virtual one. Consequently, light must reach the eye in a state of convergence in order to be focussed on the retina. Without some form of correction, including accommodation, hyperopes will not be able to focus any real objects on the retina.

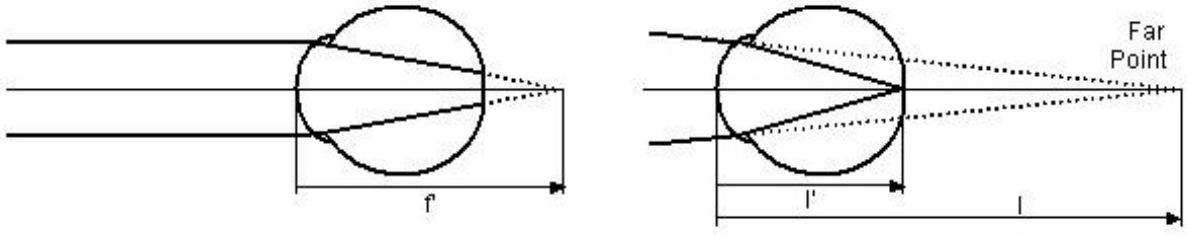

Figure 2.10: Hyperopia

When spherical ametropia is modelled it is generally distinguished to be either axial or refractive. In the former, the eye is assumed to have a standard power and any refractive error is due to a defect in the axial length. In refractive ametropia, the axial length of the model eye is assumed to have a standard value and any refractive error is attributed to an error in the refracting power.

Axial astigmatic refractive error refers to the size of an angular variation in focal power or the power equivalent to the interval of Sturm previously defined for off-axis astigmatism. The focal properties of most human eyes show at least a small degree of astigmatism. This is primarily due to the asymmetrical nature of the cornea but the shape of the crystalline lens along with misalignments of the ocular components may also have an effect.

Refractive error is quantified as the power needed to focus a ray close to the optical axis onto the retina. This is the inverse of the distance (in dioptres) from the eye's principal point to the ray's far point. This refractive error is also described by the back vertex focal power of a corrective

lens or lenses. The standard ophthalmic convention utilizes a sphero-cylindrical lens described by its spherical power (S), cylindrical power (C) and the cylinder axis (φ). This description can be partially summarized by its spherical equivalent (SE), which is the power needed to move the circle of least confusion onto the retina. A sphero-cylindrical lens' SE is related to its sphere and cylinder by

$$SE = S + \frac{C}{2} \tag{2.12}$$

When describing the eye's aberration as a wavefront error it is useful to be able to convert the defocus in the wavefront aberration function into an equivalent refractive error. The conversion was developed by examining an optical system in which defocus is the only aberration and the object is at infinity (Figure 2.11).

It has been shown that for small amounts of aberration the wave (W) and transverse aberration (TA) of a ray are related by

$$TA = -\frac{R_{ref}}{n'}\frac{\partial W(r)}{\partial r} \tag{2.13}$$

where R_{ref} is the radius of the reference sphere, n' is the image space refractive index and r represents the non-normalized radial coordinate (Welford, 1986). Since defocus is a symmetrical aberration, only the radial component is considered.

The transverse aberration can be related to the longitudinal aberration (LA) by examining Figure 2.11. This diagram shows

$$\frac{TA}{LA} = \frac{r}{R_{ref} + LA - z} \tag{2.14}$$

z is the sag of the reference sphere from the pupil plane at the point where it intersects with the ray.

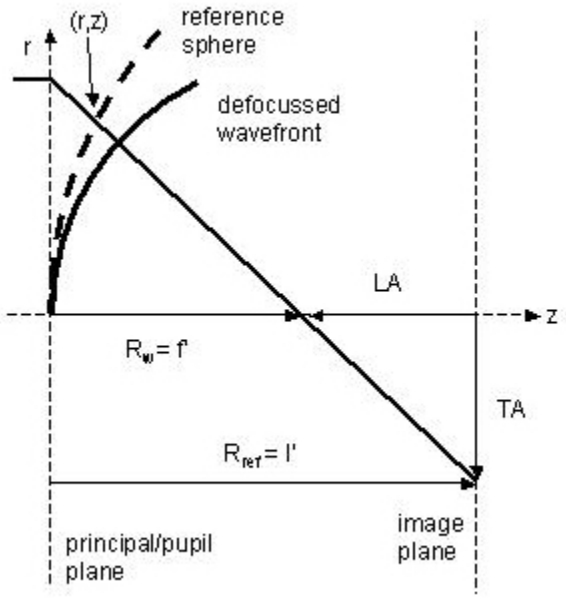

Figure 2.11: Defocused Wavefront

If z is assumed to be small then

$$LA = \frac{R_w}{r} TA \qquad 2.15$$

where R_w is the radius of curvature of the actual spherical wavefront.

The refractive error (Rx) can be related to the longitudinal aberration by first rearranging equation 2.16 into 2.17 and then inserting $Rx = 1/l, LA = f' - l', f' = R_w$ and $l' = R_{ref}$ to create equation 2.18.

$$\frac{n'}{l'} = \frac{1}{l} + \frac{n'}{f'} \qquad 2.16$$

$$\frac{1}{l} = \frac{n'(f' - l')}{f'l'} \qquad 2.17$$

$$Rx = \frac{n'LA}{R_w R_{ref}} \tag{2.18}$$

The relationship between refractive error and wavefront aberration can be seen from combining equations 2.13, 2.15 and 2.18 into

$$Rx = -\frac{1}{r}\frac{\partial W(r)}{\partial r} \tag{2.19}$$

If spherical defocus is the only aberration in the wavefront then the wave aberration function can be represented by the 2nd order, symmetrical Zernike term. With non-normalized coordinates W is

$$W(r) = \sqrt{3}Z_2^0(2(r/\rho)^2 - 1) \tag{2.20}$$

where ρ is the pupil radius. The relationship between refractive error and the defocus wavefront aberration is then

$$Rx = -\frac{4\sqrt{3}Z_2^0}{\rho^2} \tag{2.21}$$

3 Symmetrical Eye Models

3.1 Introduction

When making an initial attempt to model a complex system, it is prudent to start with the simplest possible model. If the proposed model is unable to simulate the desired properties of the complex system then it will need to be enhanced by either adjusting its existing properties or incorporating additional features. To investigate the eye's imaging capabilities, numerous attempts have been made to create a variety of different models.

Many of the eye's imaging capabilities can be calculated paraxially. In order to make these calculations, a variety of paraxial eye models have been developed (Gullstrand, 1924; Emsley, 1952; Ogle, 1968; Duke-Elder and Abrams, 1970; Fincham and Freeman, 1980; Le Grand and El Hage, 1980; Bennett and Rabbetts, 1988). The most common paraxial models use centered spherical surfaces and assume the lens is homogeneous. The main difference between these models is their choice of biometric parameters and level of simplification (Charman, 1991b). Except for Gullstrand's paraxial GRIN model (Gullstrand, 1924), schematic eyes, in which the cornea and lens are each represented by a pair of surfaces, are the most complex of the paraxial models. Simplified schematic eyes represent the cornea with a single surface. Further simplification is achieved with reduced eye models, which consist of a single refracting surface. These models do not exactly duplicate the cardinal point positions of the eye, needed for paraxial calculations, but their approximation is good. While paraxial models are perfectly adequate for many calculations in visual optics they are not designed for aberration calculations.

Advances in the knowledge of the refracting surface shapes and refractive index distributions, along with computerized ray tracing has led to the development of non-paraxial models. The simplest approach involves introducing aspheric surfaces while retaining homogenous media (Lotmar, 1971; Drasdo and Fowler, 1974; Kooijman, 1983; Navarro, et al., 1985). More elaborate models use inhomogeneous lenses. These include a variety of models in which the lens' refractive index distribution is either approximated with a finite number of shells of differing index or a smooth gradient refractive index (GRIN) (Gullstrand, 1924; Lotmar, 1971; Pomarantzeff, et al.,

1972; Watkins, 1972; Blaker, 1980; Pomarantzeff, et al., 1983; Smith, et al., 1991; Liou and Brennan, 1997; Piers, 1997).

Calculations of the longitudinal spherical aberration (LSA) of these models revealed that most of the present models estimate values that are significantly higher than empirical results (Liou and Brennan, 1996). The empirical results used by Liou and Brennan were determined by calculating the weighted average of the results from studies by Ames and Proctor (1921), Koomen, et al. (1949), Francon (1951), Ivanoff (1956), Schober, et al. (1968) and Millodot and Sivak (1979). For a ray height of 2.5 mm from the pupil centre the average LSA value was found to be 0.54 D.

These studies evaluated spherical aberration by using a ray aberration concept. They also assumed the primary aberration of the human eye to be spherical aberration. This assumption would hold true for an optical system that is rotationally symmetric about its optical axis. The human eye lacks rotational symmetry about an optical axis due to its asymmetries, such as a displaced fovea, tilts and decentrations of the refracting surfaces and pupil and asymmetries in corneal shape. Aberrations of an individual human eye rarely display rotational symmetry about the pupil centre (Charman, 1991a). The problem of ascribing all the measured aberrations to spherical aberration can be solved by using mathematical techniques to resolve aberration measurements into components from which the true amount of LSA could be inferred (Thibos, et al., 1997).

Eye models that predict LSA values similar to empirical results, are the models proposed by Thibos and co-workers (Thibos, et al., 1992, 1993; Ye, et al., 1993; Thibos, et al., 1997), Liou and Brennan (1997) and Piers (1997). The Thibos (Indiana Eye) model is a reduced eye model, which utilizes a single aspheric surface to reproduce the eye's aberrations and is consequently not anatomically accurate. When the surface asphericity was set to -0.4, this model predicted LSA of 0.95 D for a ray height of 2.5 mm which compares well to empirical data reported by Koomen, et al. (1949), Francon (1951), Ivanoff (1956) and Schober, et al. (1968).

Age has been found to change aberrations (Calver, et al., 1999; Oshika, et al., 1999; Guirao, et al., 2000; McLellan, et al., 2001), biometric parameters (Brown, 1974; Grosvenor, 1987; Kortez, et al., 1989; Goss, et al., 1990; Dubbelman and van der Heijde, 2001; Dubbelman, et al., 2001) and the optical properties of the lens (Clarke, et al., 1998; Glasser and Campbell, 1998). Consequently an eye model can only be anatomically accurate and correctly simulate aberrations for a small range of

ages. The Liou and Brennan (1997) model was designed with age dependent biometric parameters for an average age of 45 years, while its GRIN lens simulated the measurements from a 16-year-old lens (Pierscionek and Chan, 1989). For a ray height of 2.5 mm the Liou and Brennan model predicted an LSA of 0.4 D, which underestimates the corresponding average empirical value (0.54 D) they had calculated (Liou and Brennan, 1996).

Piers originally set out to develop a GRIN lens model to simulate the optical properties of young adult lenses measured by a previously developed scanning laser technique (Glasser and Campbell, 1998). Her modeling process consisted of first setting the shape and separation of the lens' refracting surfaces, along with its central refractive index as constants. She then varied the mathematical description of the GRIN and the refractive index of the lens' surface.

The laser scanning technique (Campbell and Hughes, 1981) utilizes the refraction of laser beams through different positions of excised crystalline lenses to determine their focal length and longitudinal spherical aberration (LSA). Since excised lenses assume an accommodated shape, a custom device was used to stretch the lenses to an unaccommodated state. This technique was previously used to gather data from 10 lenses from 7 subjects (Piers, 1997). These lenses ranged in age from 20 to 36 years, with an average age of 29 ± 6 years. The average focal length of the lenses was found to be 60.33 mm with a standard deviation of 5.91 mm.

The shape of the crystalline lens can be described as an asymmetric ellipsoid where the front and back sections differ. Radius of curvature (R) and asphericity (Q) or the length of the semi-axes (a and b) can be used to describe the shape of an ellipsoid. These parameters are displayed in Figure 3.1 and their relationships are shown in equations 3.1 and 3.2.

Slit-lamp photographs have been used to determine the curvature of the anterior and posterior surfaces of *in vivo* human lens (Brown, 1974). In Brown's study, radius of curvature values were presented as a function of age. Between the ages of 18 to 35 years, Brown found the anterior radius of curvature (R_{AL}) ranged from 15.17 to 13.30 mm, while the posterior radius of curvature (R_{PL}) values were between -8.36 and -7.85 mm. Piers used the median values of 14.2 and -8.10 mm for R_{AL} and R_{PL} respectively in her lens model.

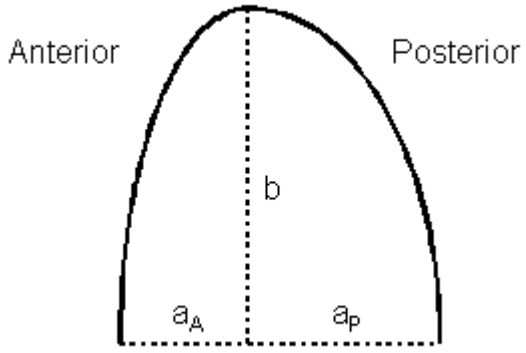

$$R = \frac{b^2}{a} \qquad 3.1$$

$$Q = \frac{b^2}{a^2} - 1 \qquad 3.2$$

Figure 3.1: Ellipsoid Shape Parameters

Recently new lens shape measurements, made with a digital slit-lamp system have been reported (Dubbelman and van der Heijde, 2001). Digital images of the contour of the vertical meridians of the lens surfaces were captured in the right eye of 102 subjects with an average age of 39 years (16 to 65). The measurements were corrected for the distortion caused by the geometry of the imaging system and the refraction of the eyes optical components. Spherical fits were performed on the central 3 mm zone. Only 65 images were analyzed for the posterior surface since its central 3 mm could not always be captured. Like Brown (1974), the radius of curvature of both the anterior and posterior surfaces were found to decrease with age (ignoring the sign). Linear regression revealed a 25-year-old lens would have radius of curvature values of 11.5 ± 0.6 and 5.9 ± 0.4 mm for the anterior and posterior surfaces respectively. Conic fits were also performed on the central 5mm of the anterior surface of the 90 lenses and the central 4 mm of the posterior surface of 41 lenses. The vertex radius of curvature of the anterior surface decreased with age. Linear regression revealed a 25-year-old lens would have a vertex radius of curvature of 11.1 mm. The anterior asphericity did not change significantly with age. Its mean value was -5.0 ± 4.7. No age dependence was found for the vertex radius of curvature and asphericity of the posterior surface. Mean values were -5.6 ± 0.6 mm and -4.0 ± 3.6.

A few earlier attempts have been made to determine the asphericity of excised crystalline lenses (Howcroft and Parker, 1977). But these measurements were made on excised lenses, which

are no longer unaccommodated and cannot be used for an unaccommodated lens model. Since no applicable data on lens asphericity existed at the time, Piers calculated her modeling values from the other parameters.

Based on the previously defined values for R_{AL} and R_{PL}, Piers calculated axial length (a) and surface asphericity (Q) of the anterior and posterior sections after taking b to be 4.6 mm, which was half of the scan diameter used in the laser scanning measurements. The asphericities of the anterior and posterior surfaces of her lens model were 8.53 and 2.10 respectively. The central thickness of the anterior and posterior sections of her lens model was 1.49 and 2.61 mm respectively.

These shape parameters produce a lens with an axial thickness of 4.1 mm. Lens thickness has been examined with ultrasonagraphy and slit-lamp photography in 100 near emmetropic subjects with an age range from 18-70 years (44.5 ± 14.9 years) (Kortez, et al., 1989). This study found that both methods produced nearly identical results, lens thickness increased linearly with age and their regression equations predicted a 25-year-old lens would have an axial thickness of 3.77 ± 0.14 mm. Another study, utilizing ultrasonography, found a mean lens thickness of 3.48 ± 0.21 mm in 30 emmetropic subjects that ranged in age from 15 to 49 years (26.4 ± 5.9 years) (Carney, et al., 1997). This study did not attempt to correlate lens thickness with age.

Previously mentioned digital slit-lamp images have also been used to determine lens thickness as a function of age (Dubbelman, et al., 2001). Measurements, on 90 subjects with an average age of 39 years showed a significant increase in axial lens thickness with age. Linear regression revealed a 25-year-old lens would have an axial lens thickness of 3.52 ± 0.12 mm.

Measurements of the refractive index at the centre and surface of 18 young adult crystalline lenses have also been performed (Piers, 1997; Clarke, et al., 1998). The central index was found to have an average value of 1.406. The surface index was found to vary significantly between 1.37 and 1.39. The surface measurements were not as reliable as the central measurements since there is a very rapid change in the refractive index close to the lens surface. Due to this variability, Piers used the average central value as a constant while the surface index was used as a variable.

Laser ray tracing data, in the equatorial plane of human lenses, revealed that the refractive index profile was relatively flat over the central two-thirds and decreased sharply in the cortical

region (Pierscionek and Chan, 1989). Measurements with a fibre optic sensor discovered a similar refractive index profile along the optical axis (Pierscionek, 1995). The laser ray tracing data within the equatorial plane from (Pierscionek and Chan, 1989) has been reanalysed to reveal a central index of 1.403 and an edge index of 1.337 (Smith, 2003). Measurements of the surface index with a fibre sensor revealed anterior surface index values ranging from 1.364 to 1.381 for the anterior surface and 1.338 to 1.357 for the posterior surface (Pierscionek, 1994). The difference between these results may be due to the fact that the laser ray tracing method measured the refractive index at the equatorial plane while the fibre sensor measurements were for the polar regions (Smith, 2003).

A more extensive investigation of surface index profiles has found that the anterior pole and equatorial edge indices were strongly age-dependent while the posterior pole index did not change with age (Pierscionek, 1997). At 20 years of age, these results predicted refractive indicies of 1.387 for the edge of the anterior pole and 1.339 for the equatorial edge. The refractive index of the posterior pole was found to be 1.395. Central index values ranging from 1.402 to 1.404 were also found.

Magnetic resonance micro-imaging has been used to map out the refractive index distribution throughout the sagittal plane of 18 human lenses ranging in age from 14 to 82 years (Moffat, et al., 2002). In this study the edge index was found to be around 1.36 with a very slight age-dependence of 0.00003 per year. The core index was found to be strongly age-dependent, ranging from 1.43 to 1.41. Smith (2003) has described how the core results are unexpected since the core consists of older fibres that have lost their water content. For the index to decrease, the crystalline proteins must somehow change to a different state with a lower index or become rehydrated.

Once her constants had been selected, Piers created six models with different variations of GRIN. These models included continuous gradient models, shell models and core models. The refractive index of the lens surface was varied for each model until its focal length matched the average empirical value of the young adult lenses. Through this process she found that a shell gradient model, where the lens has a shell of constant index surrounding a gradient core, produced LSA values that most closely resembled the empirical values of the young adult lenses.

Piers then proceeded to develop six eye models by positioning her lens models behind a symmetrical cornea. The dimensions of the anterior surface were taken from a previous study (Kiely, et al., 1982). This study found an average anterior corneal radius of curvature (R_{AC}) of 7.7 mm and an asphericity (Q_{AC}) of -0.26. The results of this study were chosen because they have been used in most eye models since the data was published. A more detailed discussion of the corneal surface shape will be given in Chapter 4.

There is considerably less information on the shape of the posterior corneal surface than the anterior surface. The first attempt to determine posterior corneal shape, involving a significant number of subjects, utilized a slit-lamp technique (Lowe and Clark, 1973). This study found mean values of 7.65 and 6.46 mm for the anterior and posterior corneal radii in the vertical meridian of 92 eyes from 46 normal subjects with an age range from 23 to 77 years (mean of 61 years). No correlation was found between either the anterior or posterior radius of curvature and age.

A new method of using Purkinje images has been compared to the slit-lamp method on 15 eyes (Royston, et al., 1990). Average posterior corneal radii were found to be 6.35 and 6.40 mm for the slit-lamp and Purkinje image techniques. The Purkinje image technique was then used to study the normal variation in the posterior corneal surface (Dunne, et al., 1992). This study reported that the mean radius of curvature of the posterior corneal surface (R_{PC}) was 6.45 mm for 60 young eyes (22.0 ± 3.3 years) and 6.25 mm for 20 old eyes (74.6 ± 5.6 years). It was suggested that the difference between the young and old groups was due to a predominance of myopes in the young group (mean sphere –2.05 D) and hyperopes in the old group (mean sphere 0.92 D).

Measurements of the anterior surface, with a photokeratscope, and corneal thickness, with an optical pachometer, have been used to estimate the shape of the posterior surface (Rivett and Ho, 1991). In 42 eyes of 21 subjects, described as young adults, Rivett, et al. found the R_{PC} had mean values of 6.16 mm and 6.10 mm in the right and left eyes. Posterior asphericity (Q_{PC}) was found to have mean values of –1.49 and –1.52 for right and left eyes.

In another study posterior corneal shape was calculated from an algorithm based on the shape of the anterior corneal surface and corneal thickness measurements (Patel, et al., 1993). Anterior corneal shape was measured with a commercially available photoelectric keratoscope. Ultrasonic pachymetry was used to determine corneal thickness. Measurements were made on 20

normal subjects ranging in age from 19 to 23 years. Average R_{PC} and Q_{PC} was found to be 5.80 ± 0.42 mm and -0.36 ± 0.37 for the vertical meridian. Along the horizontal meridian average R_{PC} and Q_{PC} was found to be 5.82 ± 0.40 mm and -0.48 ± 0.30. Average central corneal thickness was 533 ± 19 μm.

Utilizing the same technique as Patel, et al.(1993), Lam and Douthwaite (1997) calculated the apical radius of curvature and asphericity of the posterior corneal surface in 60 Chinese university students. The subjects' age was not reported. The mean R_{PC} and Q_{PC} were found to be 6.51 ± 0.40 mm and -0.66 ± 0.38.

A commercial apparatus incorporating a scanning slit has been developed to directly measure the topography of the anterior and posterior corneal surfaces (see Chapter 4 for more details). This instrument (Orbscan II, Baush and Lomb) has been used to evaluate the corneal topography in 94 normal eyes from 51 subjects (Liu, et al., 1999). This study found that, over a central 5 mm diameter, the mean R_{AC} was 7.71 mm and the mean R_{PC} was 6.49 mm. The age of the subjects in this study were not reported.

The Orbscan II has also been used to study how laser refractive surgery affects the shape of the posterior corneal surface (Seitz, et al., 2001). This study included 57 eyes from 29 subjects with a mean age of 33 ± 9 years (19 to 53). Their mean spherical equivalent refractive error was -5.07 ± 2.81 D (-1 to -15.50). Preoperatively the mean radius of curvature and asphericity of the posterior corneal surface were found to be 6.22 ± 0.22 mm and -0.02 ± 0.07 respectively. Postoperative corneal shape will be discussed in Chapter 6.

Recently digital slit-lamp images have been used to quantify the shape of the anterior and posterior corneal surfaces in the right eye of 83 subjects aged 16 to 62 years (mean 37 ± 12) (Dubbelman, et al., 2002). Digital photography was used to capture the contour of the vertical meridians of the corneal surfaces. The shapes of the meridians were defined by fitting a conic to the cornea's central 7 mm. The posterior surface measurements were corrected for the distortion caused by the geometry of the imaging system and the refraction of the anterior corneal surface. The average radius of curvature values were 7.78 ± 0.27 mm and 6.40 ± 0.28 mm for the anterior and posterior surfaces respectively. Average anterior and posterior asphericity values were -0.18 ±

0.18 and -0.38 ± 0.27. Only the posterior asphericity values were found to correlate with age (r=-0.32, p=0.003). Linear regression predicted a 25-year-old cornea would have a posterior asphericity of -0.28 ± 0.15.

The depth of the aqueous chamber has been found to decrease with age (Fontana and Brubaker, 1980; Grosvenor, 1987; Kortez, et al., 1989; Dubbelman, et al., 2001). Fontana, et al., measured a mean anterior chamber depth of 3.2 ± 0.3 mm for 196 near emmetropic eyes that ranged in age from 21-30 years. For an age group from 20-29 years, which consisted of 46 near emmetropic eyes, Grosvenor found the aqueous had a mean depth of 3.5 mm. These results were obtained with slit-lamp photography and aqueous depth was measured from the posterior corneal surface to the anterior surface of the lens.

Utilizing ultrasonography, Kortez, et al. (1989) reported a regression equation that predicts a 25-year-old eye would have an aqueous chamber depth of 3.85 ± 0.15 mm. The ultrasonography study by Carney, et al., reported a mean aqueous chamber depth of 3.60 ± 0.37 mm. Linear regression, based on digital slit-lamp images by Dubbelman, et al. (2001), predicted a 25-year-old lens would have an axial aqueous chamber depth of 3.62 ± 0.14 mm. These studies measured the central aqueous chamber depth as the distance from the anterior corneal surface to the anterior surface of the lens. Corneal thickness could be removed from these measurements by subtracting the average central corneal thickness of 0.5 mm (Charman, 1991b).

The average axial length of the eye of young adults has been found to be 24.1 mm (Grosvenor, 1987) and 23.68 ± 0.71 mm (Carney, et al., 1997).

Piers chose to use an R_{PC} of 6.5 mm and a Q_{PC} of 0 in her model. She also set her aqueous depth to 3.05 mm from the posterior surface of the cornea. The emmetropic axial length of this model was 23.9 mm.

Instead of utilizing the average empirical LSA data calculated by Liou and Brennan, Piers derived new empirical values by calculating the weighted average of wavefront aberration measurements by Howland and Howland (1977), Walsh and Charman (1985), Campbell, et al. (1990) and Collins, et al. (1995). These studies described their measurements with either Zernike or

polynomial functions and were chosen since they provide a more accurate prediction of the ocular LSA (Piers, 1997). At a ray height of 2.5 mm the average LSA from these studies was found to be 0.21 D.

While comparing her models to the new empirical data, Piers (1997) found that a model with a single, continuous gradient with variable ellipticity is the best match to the average ocular longitudinal spherical aberration derived from wavefront measurements. This resulted in a contradiction since her best lens model contained a shell gradient. Further research is required to determine a lens and corresponding eye model that utilize the same GRIN to predict empirical aberrations.

The best Piers' eye model predicted LSA of 0.10 D for a 2.5 mm ray height, which underestimates the new empirical data. The literature results Piers used to derive the new empirical data were collected from a variety of studies that included subjects with unknown ages. Consequently, no model has been shown to be both anatomically accurate and predict the aberrations, including refractive error, for a given age group. Since Piers introduced her model, new aberration data on young adult subjects has been reported (He, et al., 2000; Marcos, et al., 2000; Bueno, et al., 2002; Castejon-Mochon, et al., 2002; Paquin, et al., 2002; Cheng, et al., 2003).

To my knowledge the Piers lens and eye models are the most anatomically accurate young adult models that have been published. But her lens and eye models, that produced the best match to empirical LSA data, have different forms of the GRIN. Also her lens is thicker and the depth of her aqueous is smaller than average empirical values.

The purpose of this chapter is to describe the development of rotationally symmetric, anatomically accurate, unaccommodated, young adult lens and emmetopic eye models, based on the work of Piers. These models were designed to utilize the same form of GRIN to simulate the lens measurements and ocular aberration data used by Piers (Piers, 1997; Glasser and Campbell, 1998). New model aberrations will be compared to previously described new young adult aberration data. Since the new young adult aberration data has been described as a function of myopia, the symmetrical eye model was extended to simulate myopia.

3.2 Methods

Optical eye models were created by assembling parameters that describe the shape, position and refractive index on either side of the refracting surfaces into the optical design software program CodeV. Figure 3.2 is an example of a myopic eye model in CodeV. Appendix A contains the c-code that was used to calculate the GRIN from within CodeV. The entrance pupil was set to have a 5 mm diameter and aberrations were generated at a wavelength of 632 nm. This value was chosen since 632 nm is the wavelength of red HeNe lasers, which are commonly used to empirically measure the wavefront aberrations of human subjects. The eye model's wavefront aberrations were described with Zernike polynomials.

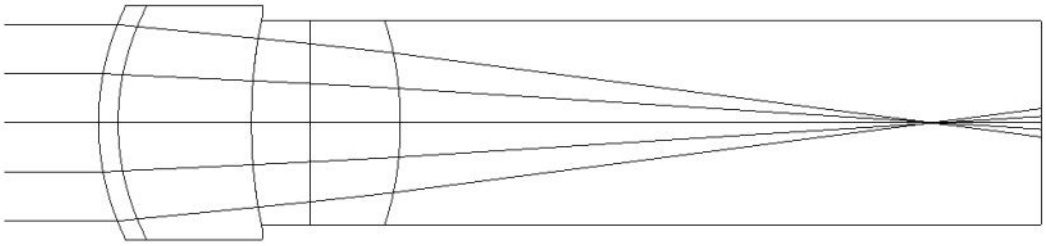

Figure 3.2: CodeV representation of a -8D refractive myopic eye model

3.2.1 GRIN Crystalline Lens Model

The foundation of this eye model is a unique GRIN crystalline lens that is similar to one of the lens models developed by Piers (Piers, 1997). Both of our lens models were designed to simulate the optical properties of young adult lenses measured by a previously developed scanning laser technique (Glasser and Campbell, 1998).

Since the surfaces of human embryonic lenses have a spherical shape while adult lenses are elliptical, it has been assumed that the lens contains a spherical gradient near its centre and an elliptical gradient near the surface (Piers, 1997). Consequently a logical model of the GRIN would consist of elliptical isoindicial surfaces that start by matching the asphericity at the surface and vary

to spherical at the lens centre. This is also the gradient form that was found to be the best model for the optics of the rat crystalline lens and eye (Campbell and Hughes, 1981).

When Piers (1997) investigated different variations of the GRIN in a simple symmetrical eye model, she found that the GRIN described by equations 3.3 and 3.4 produced the best match to the longitudinal spherical aberration of human eyes. Since the ultimate goal of this modeling process is to design an accurate eye model, I chose to use this GRIN in both my lens and eye models. Consequently my lens model's GRIN will differ from the GRIN in the best model found by Piers.

$$n(r,z) = n_C - \left(\frac{n_C - n_S}{b^2}\right)\left((1 + k(r,z))z^2 + r^2\right) \qquad 3.3$$

$$k(r,z) = k_S\left(\frac{z^2}{a^2} + \frac{r^2}{b^2}\right) \qquad 3.4$$

n(r,z) is the refractive index of the lens at the position defined by coordinates r and z. r is the distance from the optical axis and z is the distance along the optical axis. The centre of the lens is the coordinate system's origin. n_c is the index at the centre of the lens while n_s is the surface index. k is the asphericity of the isoindicial surfaces and it varies from zero at the lens centre to k_s at the lens surface. k_s is equal to the asphericity of the surface shape (Q). Since the lens is modeled as an asymmetric ellipsoid, the axial thickness (a) and consequently the shape of the isoindicial surfaces are different for the anterior and posterior portions of the lens (Figure 3.3).

The LSA of the Piers lens with the previously defined GRIN, predicted values that were not as overcorrected as the empirical data (Figure 3.4). I tried to create a model with the appropriate amount of overcorrected LSA, by varying the refractive index and shape parameter values used by Piers with the constraint that the focal length of the lens model must match the average empirical value of the young adult lens data used by Piers (1997).

The effect of centre and edge refractive index on the LSA of the lens model was investigated by varying the values used by Piers in a lens model with her shape parameters. This process consisted of selecting values for n_c that were both larger and smaller than the value of 1.406 that was used by Piers. Corresponding values for n_s were then set to give the model a focal length of 60 mm.

The results of this modelling process were used to determine the core refractive index value (n_c) in all subsequent models.

To find the shape parameters for a new model with the desired properties, a process was implemented that differed from the approach taken by Piers. This process involved first selecting values for the lens thickness (LT) and R_{AL}. Similar to Piers, b was set at 4.6 mm. The following equations were then used to calculate shape parameters.

$$a_A = \frac{b^2}{R_{AL}} \tag{3.5}$$

$$a_P = LT - a_A \tag{3.6}$$

$$R_{PL} = \frac{b^2}{a_P} \tag{3.7}$$

Equation 3.2 was then used to determine Q_{AL} and Q_{PL}. The surface refractive index (n_s) was set to give the models a focal length of 60 mm. The initial values for LT and R_{AL} were varied until a model was found that provided a good prediction of the empirical lens LSA.

3.2.2 Symmetrical Eye Model

Once an appropriate lens model had been developed, an attempt was made to create an emmetopic, symmetrical eye model. This model was designed to provide a closer prediction to the empirical LSA values, used by Piers, than her model's predictions. This was accomplished by varying Piers choices for the shape and position of the cornea. The new model's biometric parameters were then compared to empirical results.

For the symmetrical model, the anterior and posterior corneal surfaces were modeled with axially symmetrical aspheric shapes. Similar to Piers, the parameters of the anterior surface were taken from the study by Kiely, et al. (1982). The shape of the posterior corneal surface and depth of the aqueous (AD) were used as variables in the modeling process.

R_{PC} and AD were varied to set the focal length such that the emmetropic model had an axial length of 24 mm. Q_{PC} was then varied until the eye model predicted the empirical LSA values that were used previously by Piers (1997).

3.2.2.1 Myopia

Two techniques (axial and refractive) were used to add myopic refractive error to the emmetropic model. Applying axial defocus involves increasing the overall axial length (AL) of the model. This was achieved by increasing the depth of the vitreous while maintaining the refractive components. Decreasing the radius of curvature (R_{AC}) of the anterior corneal surface, while keeping all other parameters constant, was used to simulate refractive defocus. The size of the model's refractive error (Rx) was determined from its Z_2^0 Zernike coefficient and equation 2.21. Aberrations were calculated when the object point was positioned both at infinity and at the far point of the model.

3.2.2.2 Aberration Subjects

The model's wavefront aberrations were compared to previously measured data from the right eyes of 29 young adults with natural pupils. Information on this group is displayed in Table 3.1. This group was selected from 32 subjects whose aberrations were measured on a Hartmann-Shack aberroscope with a red HeNe laser (λ = 632 nm) at the University of Montreal (Paquin, et al., 2002) when the wavefront measurements were analyzed at the University of Waterloo (Bueno, et al., 2002). The 29 subjects were selected since this group had aberration measurements at both 5 and 7 mm pupils. The myopic subjects wore their best-corrected spectacles because this measurement technique cannot determine wavefront aberrations if significant amounts of defocus are present. Analysis was performed at a 5 mm pupil diameter within a naturally dilated pupil in low illumination and wavefront error was described with Zernike polynomials. It has been shown that Hartmann-Shack aberroscope measurements will be affected by the presence of best-corrected spectacles (Campbell, et al., 2003). The data I compare my models to have not been corrected for this phenomenon since data on vertex distance was unavailable.

Table 3.1: Statistics of the Aberration Subjects

	Mean ± Standard Deviation	Range
Age (years)	21 ± 3	19 to 32
Spherical Equivalent (D)	-3.25 ± 2.50	0.0 to -9.25
Cylinder (D)	-0.25 ± 0.30	0.0 to -1.25

3.3 Results

3.3.1 GRIN Crystalline Lens Model

The first attempt at modifying the Piers lens model involved varying the refractive index values used in the GRIN function in a lens model with Piers' shape parameters. When n_c was decreased from the Piers' value of 1.406, n_s also had to decrease for the lens model to maintain the proper focal length. This caused the LSA of the model to move in the undercorrected direction. Increasing n_c, above 1.406, caused the LSA to become more overcorrected. To create a lens model with Piers' shape parameters and the previously defined GRIN that predicted the empirical lens LSA required index values that were no longer within empirical limits. Consequently I decided to keep n_c at the average empirical value of 1.406 used by Piers in all future models. The failure of the Piers' model to predict empirical LSA with empirical refractive index values indicates that the either the GRIN distribution or the shape parameters in this model are not accurate. Later discussions will show that it is likely the lens surface asphericities that are unrealistic.

The modification of the lens model's shape parameters was initiated by developing a series of models with an axial thickness of 3.6 mm and R_{AL} values that were within the range found by Brown (1974) for 18 to 35 year old lenses. The LSA of these models was overcorrected but not as overcorrected as the empirical lens data and the corresponding R_{PL} values were approximately 2 mm outside the range measured by Brown.

The next step taken was to create a series of thicker lenses. A lens thickness of 3.8 mm was selected to match the value for a 25-year-old lens predicted by Kortez, et al., (1989). These models predicted lens LSA values within the empirical limits. From this group, I chose the model with Brown's median value for R_{AL} as the Priest lens model. This model has refractive index parameter values of 1.406 and 1.377 for n_c and n_s respectively. Table 3.2 compares the shape parameters of the Priest and Piers models. Figures 3.3 and 3.4 display the isoindicial surfaces of my lens model. Figure 3.5 shows the LSA of the Priest and Piers models compared with empirical data.

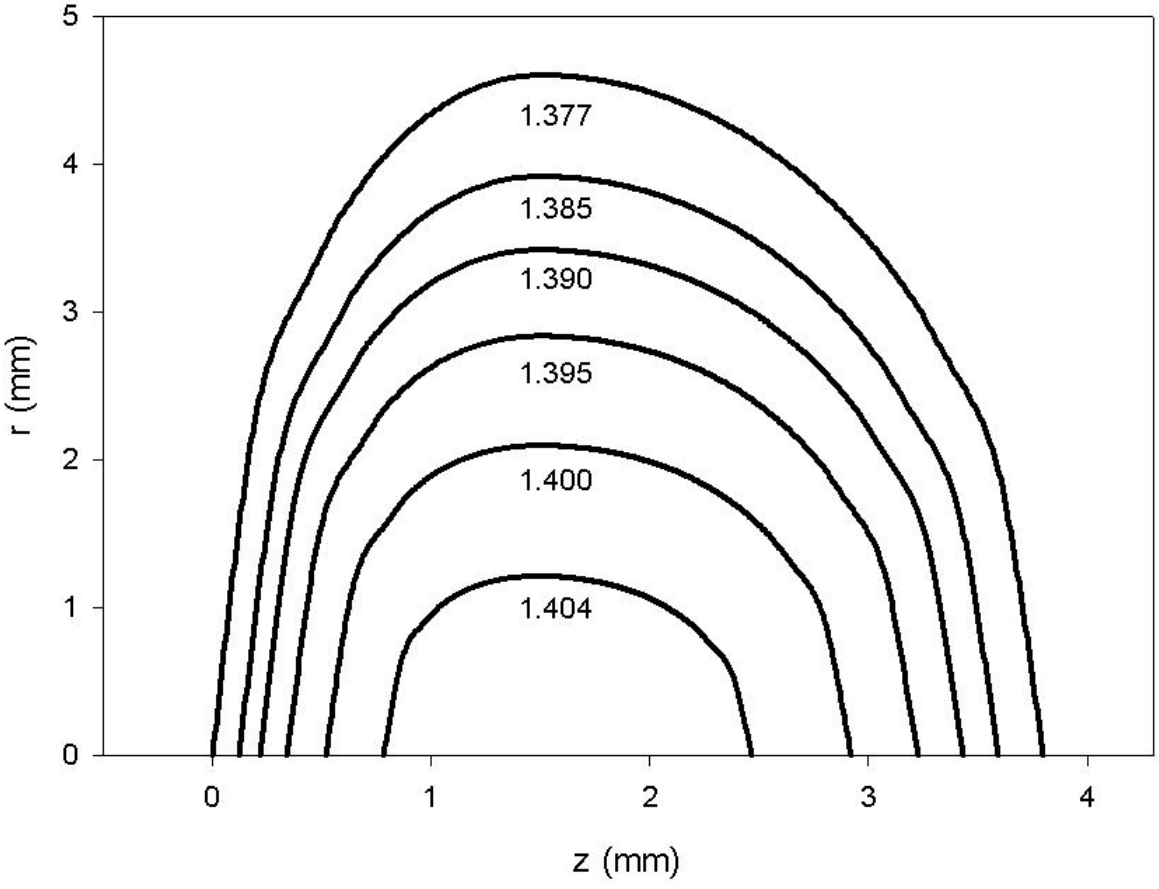

Figure 3.3: Isoindicial surfaces of the Priest GRIN crystalline lens model. r is the radial component in a polar coordinate system while z represents distance along the optical axis from the anterior surface.

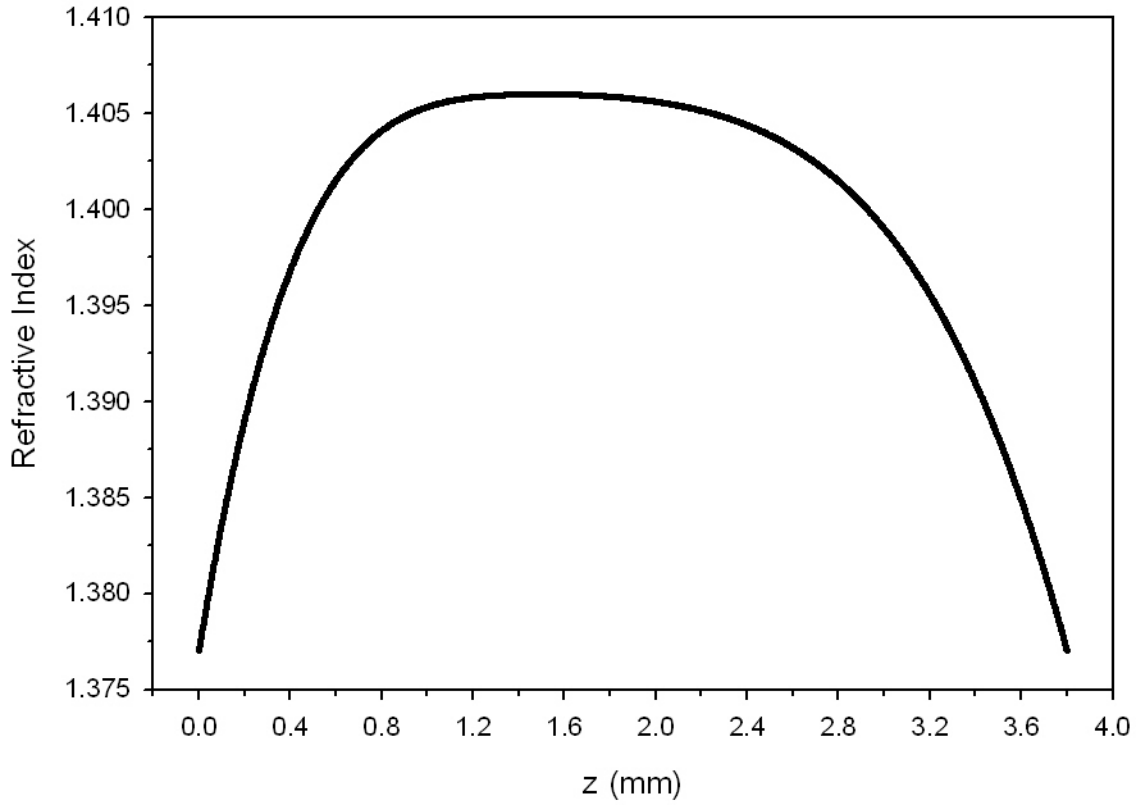

Figure 3.4: Refractive index profile of the Priest model along the optical axis. z represents the distance along the optical axis from the anterior surface (z=0) to the posterior surface (z=3.8).

Table 3.2: Lens Parameters of the Priest and Piers Models. The parameters shown here that are used to calculate the GRIN are also repeated again in Appendix A.

Model	R_a (mm)	Q_a	a_a (mm)	R_p (mm)	Q_p	a_p (mm)	b (mm)	n_c	n_s
Priest	14.2	8.53	1.49	-9.16	2.97	2.31	4.6	1.406	1.377
Piers	14.2	8.53	1.49	-8.10	2.10	2.61	4.6	1.406	1.378

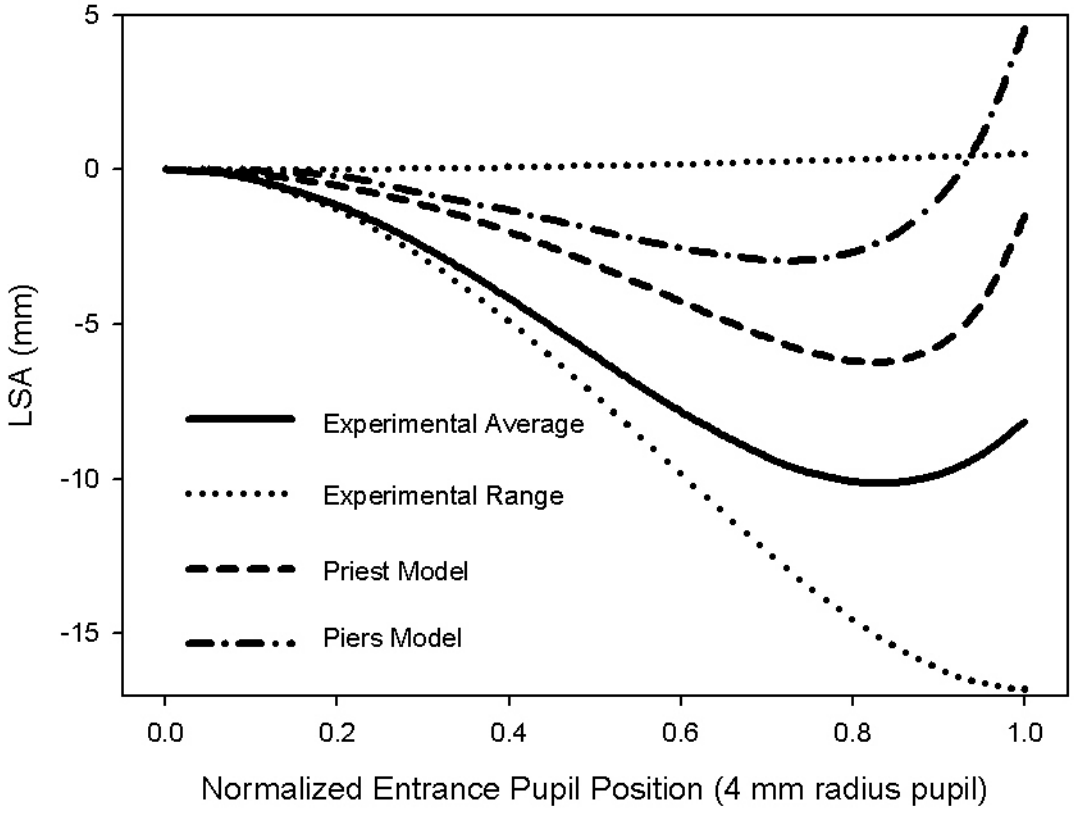

Figure 3.5: LSA of Experimental Results and Crystalline Lens Models. Experimental and model data from Piers has been reprinted with permission.

3.3.2 Symmetrical Eye Model

Table 3.4 shows the parameters I chose to use in my emmetropic, symmetrical eye model. AL is the axial distance between optical surfaces and n represents the refractive index. Figure 3.6 displays the ocular LSA of my model, the Piers model and the empirical data. The Priest model predicted LSA of 0.24 D for a 2.5 mm ray height. Table 3.5 shows how the emmetropic model was changed to create the myopic models. Linear regression revealed that the axial length of the models with axial defocus increased by 0.45 mm with every dioptre of myopic refractive error. Similarly, the central radius of curvature in the refractive defocus models was found to decrease by 0.13 mm for every dioptre of myopia.

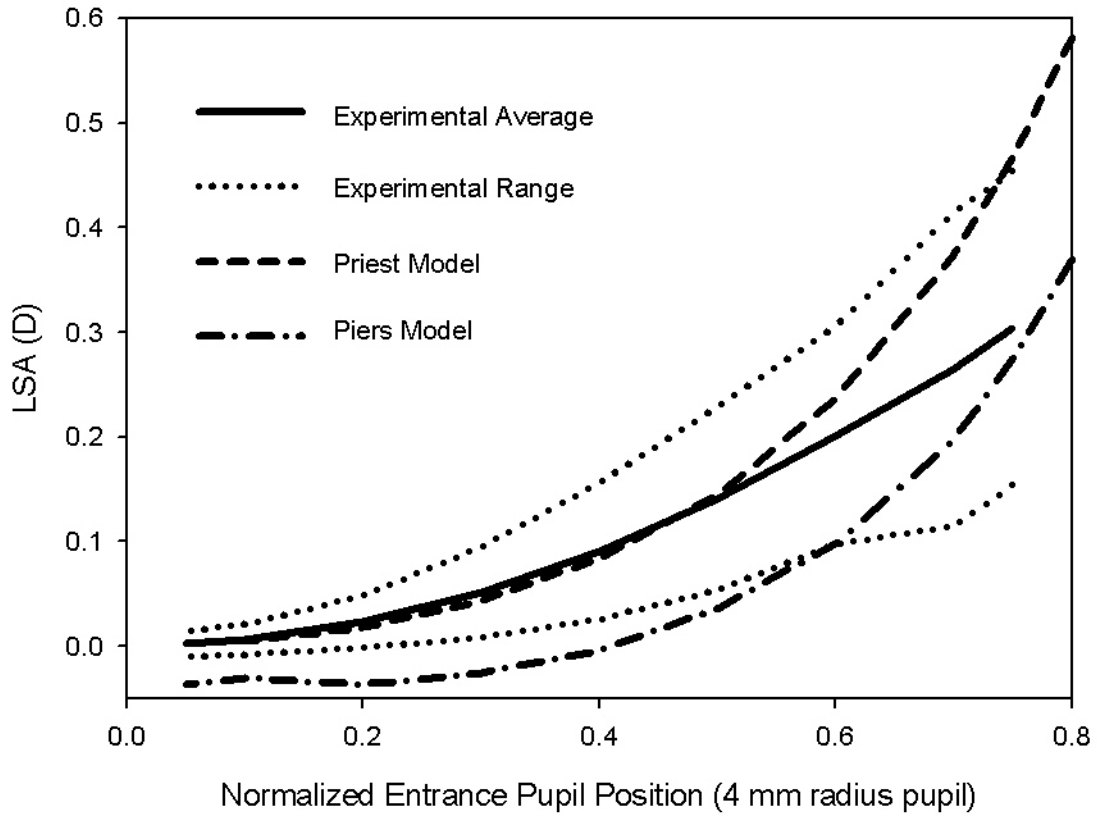

Figure 3.6: LSA of Empirical Data and Emmetropic Symmetrical Eye Models. Experimental and model data from Piers has been reprinted with permission. Empirical values determined by Piers (1997) by calculating the weighted average of wavefront aberration measurements by Howland and Howland (1977), Walsh and Charman (1985), Campbell, et al. (1990) and Collins, et al. (1995).

Table 3.4: Emmetropic Model Parameters of the Priest Eye Model. GRIN calculation is outlined in Appendix A.

Surface	R (mm)	Q	AL (mm)	n
Anterior Cornea	7.7	-0.26	0.5	1.376
Posterior Cornea	6.3	-0.30	3.4	1.336
Anterior Lens	14.2	8.53	3.8	GRIN
Posterior Lens	-9.16	2.97	16.3	1.336

Table 3.5: Myopic Model Parameters

Rx	Axial Model		Refractive Model	
	AL (mm)	Z_4^0 (μm)	R_{AC} (mm)	Z_4^0 (μm)
0	24.00	0.031	7.700	0.031
-1	24.41	0.033	7.552	0.041
-2	24.79	0.035	7.409	0.052
-3	25.20	0.037	7.271	0.064
-4	25.61	0.039	7.136	0.076
-5	26.05	0.041	7.007	0.089
-6	26.50	0.043	6.882	0.103
-7	26.97	0.045	6.760	0.118
-8	27.46	0.047	6.643	0.133
-9	27.97	0.050	6.529	0.149
-10	28.51	0.052	6.418	0.165

3.3.3 Wavefront Aberrations of the Symmetrical Eye Model

Wavefront aberrations of the myopic models were quantified with a series of Zernike polynomials for a 5 mm pupil. Since the model has symmetrical surfaces and is centered on the optical axis, it has only symmetrical aberrations. These include defocus (Z_2^0) and spherical aberration ($Z_4^0 \& Z_6^0$). The Z_6^0 term was found to be insignificant since it was always less than 10% of the Z_4^0 term.

Although moving the object to a model's far point was found to remove the model's defocus it had little affect on the spherical aberration. The largest change observed was a decrease of 1.8% for the -10D refractive model. This indicates that symmetrical myopic eye models can be created with their object positioned at infinity without affecting the model's aberrations.

Figure 3.7 displays the spherical aberration (SA) and high-order RMS (3^{rd} and 4^{th} order terms) for the wavefront aberrations of the young subjects compared to the model's results. The subject's SA is not dependent on refractive error ($p=0.63$). The SA of both the axial and refractive models increase linearly with refractive error. Linear regression revealed that the SA of the axial defocus model increased at a rate of 0.002 μm/D of myopia ($p<0.0001$). The SA of the refractive model was found to increase at rate of 0.013 μm/D of myopia ($p<0.0001$). While there is a statistically significant increase in the SA of both types of models all predicted values are contained within 2 standard deviations of the subject's mean SA. Since the SA data from the young subjects and the refractive model passed a normality test but failed an equal variance test, a Mann-Whitney Rank Sum Test was used to compare their means. The resulting p-value of 0.79 revealed there is not a statistically significant difference between the mean SA of the young subjects and mean SA of the refractive model. The SA data from the subjects and axial model failed a normality test. Consequently, a Mann-Whitney Rank Sum Test was used to compare the median values of these two groups. The p-value of 0.02 revealed there is a statistically significant difference between the median values of the young subjects and the axial model.

The rate at which SA increased with myopia for the empirical and model data was compared by analyzing the slopes of their linear regressions with t-tests. The SA of the refractive model increased with myopia at a statistically significantly higher rate ($p<0.01$) than the axial model. Compared to the empirical data, the difference in the rate of increase in SA with myopia for both the refractive ($p=0.17$) and axial ($p=0.64$) models were not statistically significant.

The high-order RMS from both models is significantly less than that measured for the subjects.

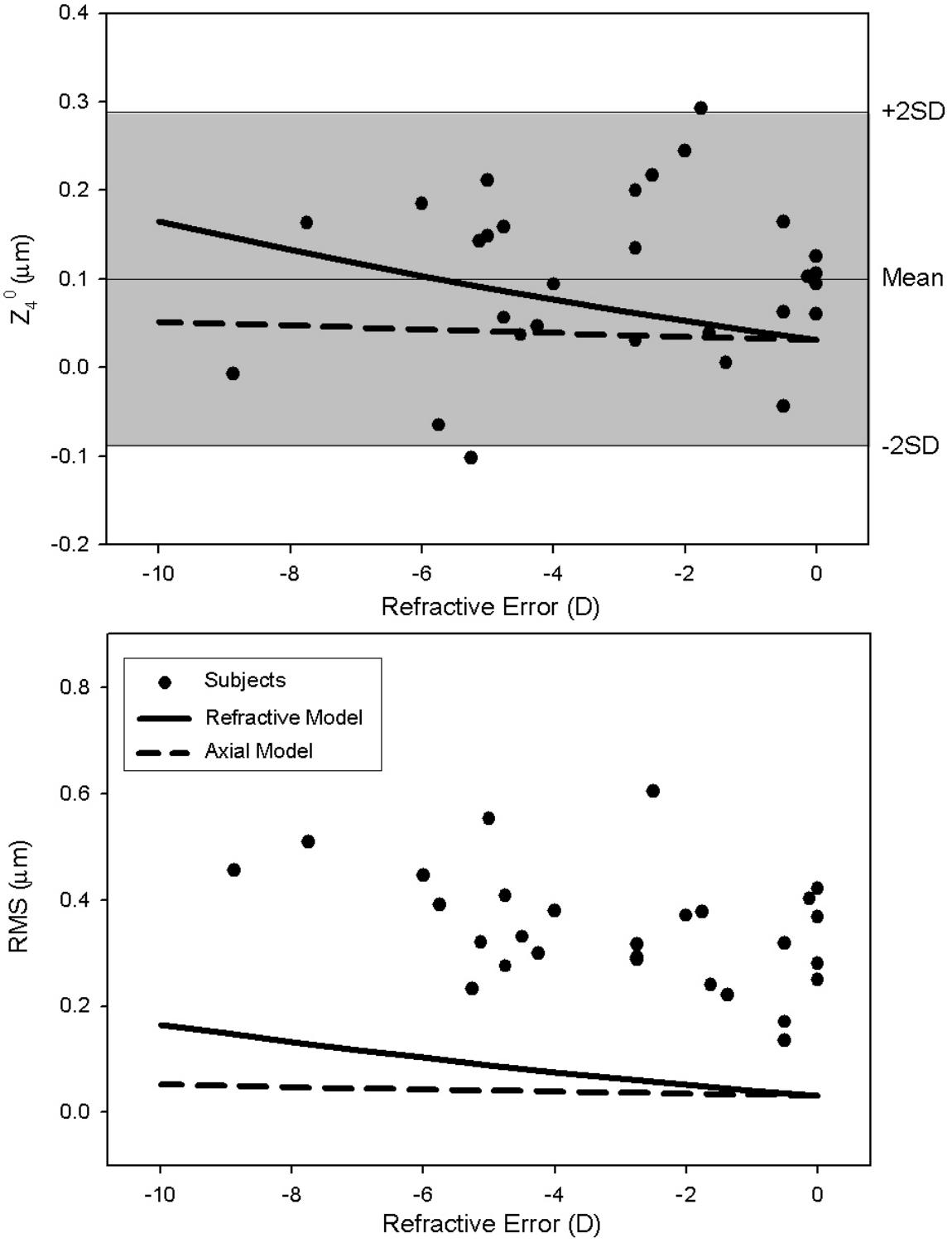

Figure 3.7: Aberrations of the subjects and the symmetrical models. The shaded region highlights the mean and 2 standard deviations of the empirical SA.

3.4 Discussion and Conclusions

Piers developed crystalline lens and eye models by fixing the shape parameters and varying the form of the GRIN. While her best eye model is relatively good at predicting ocular empirical LSA values, when compared to previous models, some of its biometric parameters, like lens thickness (4.1 mm) and anterior chamber depth (3.05 mm), do not have average values. She also found that different mathematical forms of the GRIN produced her best lens and eye models. These results were a consequence of the approach she used to develop her models. To develop an eye model with average biometric parameters that was a better predictor of LSA, a different methodology was needed. Instead of fixing the shape parameters and varying the form of the GRIN, like Piers, I chose to fix the GRIN and vary the shape parameters. This approach was chosen so that the lens and eye models, I developed, would use the same GRIN.

Previous GRIN models (Smith, 2003) use polynomial equations of different orders to calculate their GRIN. The refractive index values, calculated from the GRIN equation chosen for the model developed here, are more constant over the inner two thirds and decrease more sharply near the surface than values calculated from a polynomial equation. Consequently the GRIN used here more closely estimates the shape of the refractive index profile determined by Pierscionek (1995) than models with a polynomial GRIN.

My model was designed to predict the empirical LSA data that Piers (1997) had calculated. Model predictions were then compared to newer empirical wavefront aberration data (Bueno, et al., 2002; Paquin, et al., 2002). Since the model presented here was originally developed, newer empirical wavefront aberration data has been published (He, et al., 2000; Marcos, et al., 2000; McLellan, et al., 2001; Porter, et al., 2001; Castejon-Mochon, et al., 2002; Cheng, et al., 2003). If the model was redesigned to predict the newer wavefront aberrations, its biometric parameters or GRIN might have to change. This could affect the model's anatomical accuracy.

Newer measurements of empirical biometric parameters have also been published since this model was developed. If these measurements had been incorporated, the predicted aberrations and anatomical accuracy of the model would change.

The values for R_{AL} and R_{PL}, used by Piers, were based on the slit-lamp measurements of Brown (1974). Glasser and Campbell (1999) have discussed how slit-lamp measurements of an ocular surface are necessarily made through the optical components that precede them. They describe how the anterior lens surface measurements are influenced by the cornea and anterior chamber depth while the posterior lens surface measurements are additionally biased by the optics of the lens. Brown made corrections for an average central corneal curvature, but slit-lamp imaging is done through the peripheral corneal where the asphericity of the cornea and possible age-dependent changes in corneal curvature and anterior chamber depth could be sources of systematic errors in measuring the anterior lens surface curvature. The posterior lens surface measurements are additionally influenced by the unknown gradient refractive index of the lens. Since Brown provided no corrections for the lens gradient, his values for R_{AL} are considered to be more accurate than his values for R_{PL}. Consequently I chose to use the same constant value for R_{AL}, like Piers, while R_{PL} was used as a variable in my modeling process.

Using this methodology, I chose to use a R_{PL} value of –9.16 mm. This value differs from Brown's median value of –8.10 mm, used by Piers, and is 0.8 mm beyond his range of experimental values. Since I used the same relationship between shape parameters in my lens model as Piers had, changing the R_{PL} value caused my lens to be thinner. The axial length of my lens is 3.8 mm, which is closer to the young adult average value of 3.77 ± 0.14 mm (Kortez, et al., 1989) than the axial length of the Piers model at 4.1 mm. Even though my R_{PL} value is different than Brown's data, my lens model's thickness and predicted LSA values are closer to empirical averages than the Piers model.

Recently published lens shape data (Dubbelman and van der Heijde, 2001) have found that average radius of curvature and asphericity values are 11.1 mm and -5.0 for the anterior surface. Average radius of curvature and asphericity values of the posterior surface were found to be -5.6 mm and -4.0. The radius of curvature (14.2 mm and -9.16) and asphericity values (8.53 and 2.97) that I used for the anterior and posterior surfaces of my lens model are quite different from the results of Dubbelman and van der Heijde. This indicates that calculating the asphericity of the lens surfaces based on the asymmetric ellipsoid model that was used does not create an anatomically accurate lens. If their measurements had been available when this modelling was initiated they could have been utilized to create an anatomically accurate lens model. Even though this lens model has

now been found to be anatomically inaccurate, the methodology used to create is still valid and may still be a good foundation for eye models since it predicts empirically determined lenticular LSA.

Using my newly developed lens model I was able to create an emmetropic eye model that predicted the empirical LSA values calculated by Piers better than the models proposed by Piers, Liou and Brennan and Thibos (Figure 3.8). The difference with the Thibos model can be explained by realizing that their model was selected to predict a different set of empirical LSA data than the empirical LSA data calculated by Piers. Besides the lens models, the differences between the Priest and Piers eye models included the shape of the posterior corneal surface and depth of the aqueous.

To produce an emmetropic axial length of 24 mm, I chose to use an R_{PC} of 6.3 mm and an AD of 3.4 mm. The Piers model had an emmetropic axial length of 23.9 mm with a R_{PC} of 6.5 mm and an AD of 3.05 mm. The axial lengths of these models are slightly below the average young adult value of 24.1 mm found by Grosvenor (1987). Average empirical values for R_{PC} have been found to range between 5.8 and 6.5 mm (Lowe and Clark, 1973; Royston, et al., 1990; Rivett and Ho, 1991; Dunne, et al., 1992; Patel, et al., 1993; Lam and Douthwaite, 1997; Liu, et al., 1999; Seitz, et al., 2001; Dubbelman, et al., 2002). In most of these studies the age of the subjects was either not reported or no age dependence was found. The values used in the Piers and Priest models are both within the range of empirical R_{PC} values. The AD value of 3.4 mm used in the Priest model is closer to average young adult empirical values of 3.2 ± 0.3 mm (Fontana and Brubaker, 1980), 3.5 mm (Grosvenor, 1987), 3.35 ± 0.15 mm (Kortez, et al., 1989) and 3.10 ± 0.37 mm (Dubbelman, et al., 2001) than the value of 3.05 mm used in the Piers model.

During my modeling, I determined a Q_{PC} of –0.3 produced a model that was the best predictor of the LSA of the wavefront data used by Piers. This value is significantly different from the value of 0 used by Piers. Average empirical Q_{PC} values of -1.5 (Dunne, et al., 1992), -0.44 (Patel, et al., 1993), -0.66 (Lam and Douthwaite, 1997) have been determined from measurements of the anterior corneal surface shape and corneal thickness. My Q_{PC} value is close to the average, empirical, young adult value of -0.28 ± 0.15 found by Dubbelman, et al. (2002) with a digital slit lamp technique.

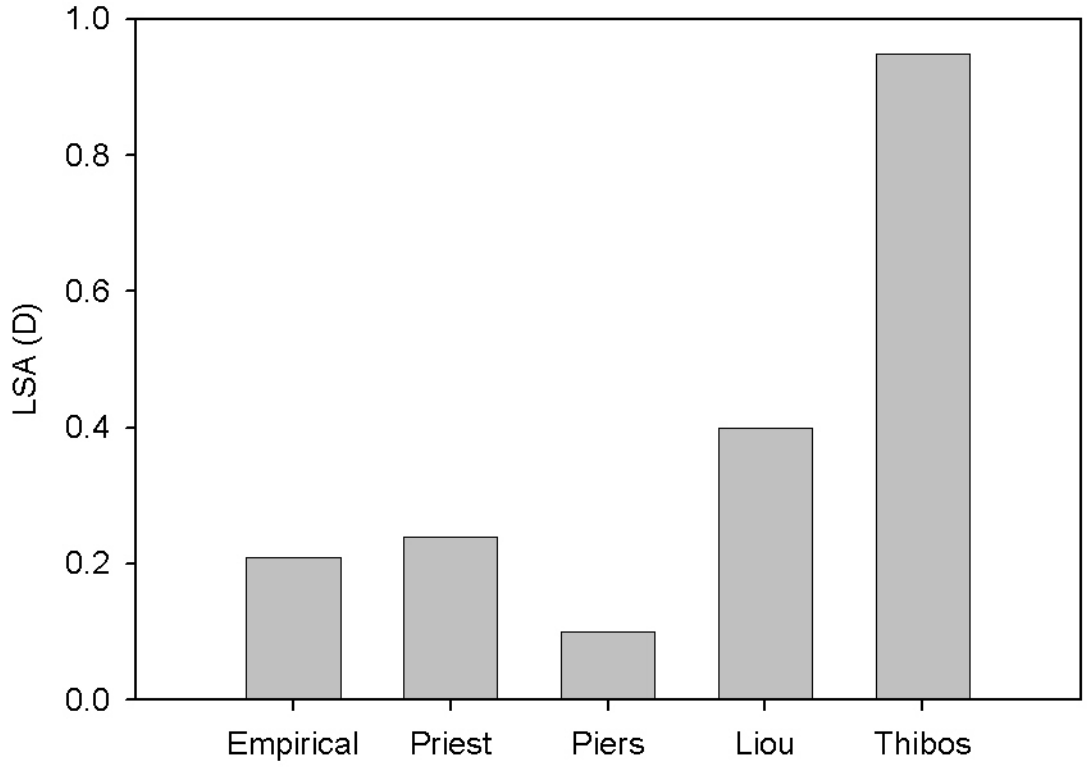

Figure 3.8: Empirical and model LSA for a ray height of 2.5 mm. The empirical values shown here were calculated by Piers (1997). The model from Thibos, et al (1997) was designed to predict empirical LSA data that was older than the data used by Piers.

The empirical wavefront data that I compared my myopic models against were measured through spectacle corrections (Bueno, et al., 2002). Consequently, this aberration data is a combination of the spectacle lens and the eye. While spectacle lenses are expected to have negligible on-axis aberrations (Atchison, 1985), Bueno, et al. (2002) and Campbell, et al. (2003) have described how increasing negative spectacle power could cause Hartmann-Shack aberroscope measurements to increase. They calculated that such an effect would remove up to 20% of the increase they observed in the RMS of the high-order aberrations with increasing myopia.

Cheng, et al. (2003) investigated the effect of spectacle lens correction by using a commercial ray-tracing program to compute the aberrations of trial lenses. They determined that negative trial lenses produced negative spherical aberration, which tend to cancel a very small portion of the

positive spherical aberration of the eye. But this compensation was not large enough to be significant.

Bueno, et al (2002) also describe how the change in the vergence of the light caused by the spectacle lens is equivalent to changing the position of the far point of the eye which could cause a real change in the ocular aberrations with increasing myopia. This idea was investigated by determining my model's aberrations when the object was moved to the model's far point. The result that object position had little to no effect (<2% decrease) on the higher order aberrations was surprising since it goes against the current theory. For most optical systems, the wavefront aberration will usually be different for rays from different object points with the same position in the exit pupil (Smith and Atchison, 1997). Cheng, et al. (2003) found that the SA predicted by a single surface model will significantly increase with axial myopia that is corrected with spectacle lenses. Since this result does not match empirical results, a single surface model with axial myopia cannot adequately predict the aberrations of myopes (Cheng, et al., 2003).

These models are the same as most optical systems except for the GRIN. To investigate if the GRIN was balancing the expected change in aberrations from the change in object position, I calculated the aberrations for the myopic models after replacing the GRIN with the constant refractive index value of 1.416 used in the Gullstrand-Emsley schematic eye. When the lens model had a constant refractive index, changing the vergence of the incoming light was seen to change the aberrations by up to -4.5% for a -10D refractive model. The corresponding change in aberrations for the corresponding GRIN models was only -1.8%. This indicates that the GRIN was balancing the expected change in aberrations with changing object position by a small amount.

The results of Bueno, et al. (2002), shown here for a 5 mm pupil, have been found to be consistent with previous literature. In a study of 37 subjects (0 to -7D, 17-30 years, 4.5 mm pupil) Collins, et al. (1995) used a crossed-cylinder objective aberroscope to find that spectacle-corrected myopes had lower 4^{th} order terms than emmtropes. However, these results could be misleading since the aberrations in at least a third of the myopic subjects were too large to be measured by this technique and were excluded. He and colleagues (2000) also found that spherical aberration did not change as a function of ametropia in a study of 70 subjects (11-29 years) measured with a spatially resolved refractometer. Marcos, et al. (2000) used a laser ray tracing technique on 22 dilated eyes (23-33 years, -0.6 to -13D, 6.6 mm pupil) and found a significant increase in the spherical aberration

term with myopia. This is similar to the results found by Bueno, et al. (2002) for a dilated 7 mm pupil, which have not been shown here.

The proposed symmetrical models provide a good estimate of the spherical aberration of young adults with natural pupils. Even if the subjects had their high-order RMS values compensated for spectacle magnification, the models would still not contain enough total aberrations to simulate the amount of high-order aberrations observed in young adults. This is not surprising since symmetrical spherical aberration is the only high-order aberration in the symmetrical models and the high order aberrations of human subjects are dominated by asymmetrical aberrations like coma (Charman, 1991b).

Consider the standard reduced eye model, which has a power of 60 D and an emmetropic axial length of 22.2 mm (Bennett and Rabbetts, 1989). Paraxial calculations show that axial myopia is induced in these models by increasing the axial length by 0.37 mm/D and decreasing the radius of curvature of the refracting surface by 0.09 mm/D induces refractive myopia. These values differ from the rates for axial myopia (0.45 mm/D) and refractive myopia (0.13 mm/D) that were found for the models introduced here. These differences illustrate how a GRIN model differs from a reduced model.

Measurements of the biometric parameters in myopic subjects have shown that there is a statistically significant relationship between the refractive error and both the axial length and curvature of the anterior corneal surface (Carney, et al., 1997). Linear regression of Carney's results predicted that a refractive error of -10 D would correlate with an anterior corneal radius of curvature of 7.4 mm and an axial length of 26.8 mm. A comparison to the values used in the myopic models show that creating defocus by either a purely axial or refractive method causes the models to no longer be anatomically accurate.

Carney, et al. (1997) also found that the asphericity of the anterior corneal surface correlated with myopic refractive error. Adding this relationship to the myopic models could enhance their ability to predict the aberrations of myopic subjects.

While the refractive myopic models were found to provide a good prediction of the amount of SA in young adults, the axial myopic models did not. Both models predict a small variation in SA

with refractive error. This suggests that the combinations of corneal power and axial changes inherent in myopia produce little change in SA with refractive error. Any measured change in aberrations may be due to additional changes in shape and GRIN parameters. Axial models could be developed that predict the SA values closer to the mean of the empirical data by adjusting the asphericity of the posterior corneal surface. But this could have adverse effects on the SA predicted by refractive models with the same corneal shape parameters. Regardless it has been shown that rotationally symmetric, GRIN myopic eye models, which accurately predict the SA in young adults, can be developed. But these models do not possess the same amount of total aberrations as young adult myopes and are not anatomically accurate because in the real eyes both corneal power and axial length differ from emmetropia. Consequently their use as a tool to investigate the eye's imaging capabilities will be limited. In order for them to be more useful they need to possess the appropriate amount of asymmetrical aberrations and accurately simulate how myopia develops.

4 Corneal Topography and Myopia

4.1 Introduction

To improve the myopic eye models, introduced in the last chapter, they need to become more anatomically accurate and predict the correct amount of rotationally asymmetric aberrations. In the last chapter, the corneal surfaces were modeled with a symmetric surface but normal corneas have a characteristic asymmetry in the surface shape that can produce a corresponding astigmatic refractive error. To accurately describe this shape, a rotationally asymmetric surface should be used. Myopia was simulated, in Chapter 3, to be either purely axial or refractive. The anatomical changes in axial length and corneal shape, from these simulations, do not correspond with previous measurements (Carney, et al., 1997). An accurate simulation of myopia would utilize the true changes in corneal shape as a function of refractive error.

Many attempts have been made to quantify corneal shape with a variety of surfaces and mathematical functions. A description of these studies will be given in the next section. Unfortunately they do not provide all the necessary information to improve the models from Chapter 3. To my knowledge, there is not a single study that describes both corneal shape with an asymmetrical surface and correlates shape parameters with myopia.

It has been suggested that a biconic model would provide a useful representation of the corneal surface (Schwiegerling and Snyder, 1998). A biconic surface shape is defined with conic profiles that change with meridian. The central curvature and asphericity of the conic profiles varies between the values from two perpendicular meridians. If a biconic surface can accurately describe corneal shape then its use in an eye model may allow the model to predict some of the rotationally asymmetric aberrations that have been observed clinically.

To facilitate mathematical processing and statistical analysis, it has been shown that a sphero-cylinder correction (refractive error) can be described by a function with orthogonal components known as Jackson Cross Cylinders (JCC) (Thibos, et al., 1994). If a biconic surface can

also be mathematically described with JCC components, then these descriptions could be useful in determining correlations between corneal shape and refractive error.

Previously, clinical measurements of corneal topography have mainly depended on specularly reflected images from the anterior corneal surface. Only a small amount of information exists about the shape of the posterior corneal surface. New techniques of measuring corneal topography have recently become clinically available. The PAR Corneal Topography System (PAR CTS) utilizes diffusely reflected images and has been found to be more accurate than the specular reflection techniques used in previous studies of corneal shape (Priest and Munger, 1998). Images of a slit, formed by light scattered from the anterior and posterior corneal surfaces, have been used to provide a measure of the anterior and posterior corneal topography (Mejia-Barabosa and Malacara-Hernandez, 2001). Commercially, this technology is applied in an instrument called the Orbscan II, which has also been shown to accurately predict the shape of calibrated surfaces (Cairns, et al., 2002). Utilizing measurements from these instruments may provide a more accurate description of both corneal surfaces.

This chapter will describe an analysis of the corneal topographies from a large group of emmetropes and myopes, measured on either the PAR CTS or Orbscan II. Analysis of these measurements will be used to investigate whether a biconic provides a more accurate representation of corneal shape than simpler geometric surfaces. A JCC based function will be used to describe the corneal shape. This description will be used to show how shape parameters change as a function of myopia.

4.2 Background

For more than a century it has been known that the cornea is the major refractive element of the eye. Numerous attempts have been made to qualitatively and quantitatively assess both corneal shape and power.

Originally corneal curvature was estimated by matching the size of images reflected from a subject's cornea with those produced from calibrated spheres (Belin and Misery, 1999). This method takes advantage of the fact that the cornea reflects like a mirror, where its radius of curvature determines paraxial magnification. If an object of known size is placed a known distance from the cornea then the radius of curvature can be deduced from the size of the reflected image (Rubin, 1993). Utilizing this principle, the keratometer was developed. This instrument determines the average corneal curvature from two sets of diametrically opposed points (~ 3mm apart) on the central cornea (Belin and Misery, 1999).

Since the keratometer only analyzes a small portion of the corneal surface, efforts to obtain qualitative information about the shape of the entire cornea led to the development of keratoscopic imaging. The technique of keratoscopy involves analysing the shape of an image reflected from the corneal surface. Usually the target object is a series of circular concentric rings referred to as a Placido disk. In general, the reflective rings will appear minified (closer together) on steeper sections of the cornea and magnified (farther apart) on flatter areas. Corneal astigmatism will cause the image to appear as a series of elongated ovals. Irregularities in the corneal surface will produce deformed images. A significant limitation of this technique is its precision. Small irregularities that produce significant visual defects cause only minor deformations in the reflected images. The limitations of this technique made it clear that more sensitive and quantitative measurement techniques and descriptions of corneal shape were needed (Belin and Misery, 1999).

4.2.1 Corneal Shape Descriptions

Quantitative descriptions of corneal shape are usually made in terms of the surface's curvature or elevation as a function of spatial coordinates (x, y or r, θ). These functions are commonly plotted as colour-coded contour maps or three-dimensional surfaces for visual inspection.

Early attempts to quantify surface shape began with the evolution of keratometry and keratoscopy into a new instrument, which will be discussed in the next section. This technique provides an estimate of the surface tangent at numerous points. Surface shape, at a particular point, is then expressed as the curvature or radius of curvature of a reference sphere with the same tangent as the point in question (Belin and Misery, 1999). For display purposes, a paraxial calculation is used to transform radius of curvature values into refractive power.

The first description to utilize this technique is generally referred to as axial curvature. Axial curvature is constrained such that the reference sphere's centre of curvature must lie on the optical axis. In this representation, surface shape is described by the distance from a surface point to the optical axis along the normal to the curve at that point. In strict mathematical terms, this description behaves quite differently from curvature, as it will underestimate areas of relatively greater curvature and overestimate areas of relatively lesser curvature. This is due to the fact that the axial curvature formulation is a smoothing function that flattens out the steepest areas and steepens the flattest areas (Roberts, 1996). Due to this limitation, surface shapes tend to be smooth and localized changes in curvature and peripheral data are poorly represented. For central areas this description provides a reasonable approximation of refractive power (Belin and Misery, 1999).

A second curvature description is called tangential, instantaneous or local curvature. It is similar to axial curvature except that the centres of curvature of the reference spheres do not have to fall on the optical axis. The positions of the centres of curvature depend on the intersection of the normals from neighbouring points. This representation is a true depiction of surface curvature. It reflects local changes and peripheral shape better than axial curvature but it is not a good depiction of refractive power (Belin and Misery, 1999).

Compared to the curvature descriptions, elevation is a more straightforward measure of the true surface shape. It is defined as the separation of the actual surface from a reference surface. These distances are also referred to as the sagital height or sag of the surface. The simplest reference surface is a plane perpendicular to the optical axis of the system, which is commonly through the corneal vertex. While this description provides a good overall representation of the surface shape, it does not visually convey subtle yet optically important features such as radial asymmetry. Since the cornea is approximately spherical, a useful reference surface is the sphere that has the minimum deviation from the actual surface. By using this best-fit sphere as the reference surface, subtle changes in the corneal surface are visually magnified and more readily apparent to an observer (Belin and Misery, 1999). The difference between these representations of the same surface is apparent in Figure 4.1.

A mathematical relationship exists between the curvature descriptions and elevation of the surface. Axial curvature is based on the first-order derivatives of the surface elevation, while tangential curvature is related to the elevation by second-order derivatives (Belin and Misery, 1999). It is a relatively straightforward process to determine the curvature of a surface by differentiating its elevation data. Conversely, elevation data cannot be determined by integrating curvature data without first making some assumptions about the surface's form and continuity. Consequently, elevation referenced to an arbitrary fixed plane has been proposed as the standard description since it defines surface shape in the simplest terms without any assumptions (Applegate, et al., 1995). This description should be used for any attempts to quantify corneal shape or compare measurement techniques and will be used exclusively in this thesis.

Corneal surface shape can be quantified by comparing measured topographies to known surfaces. The parameters that describe the shape of the known surface that best fits the topography can also be used to describe the cornea's shape. A best-fit surface is found by minimizing the difference between the known and the measured surface.

In Chapter 2, spherical and rotationally symmetric conic surfaces were introduced as descriptors of corneal surface shape (equations 2.8, 2.9 and 2.10). But the cornea is not rotationally symmetric. Utilizing a complex, rotationally asymmetric surface descriptor may be more accurate.

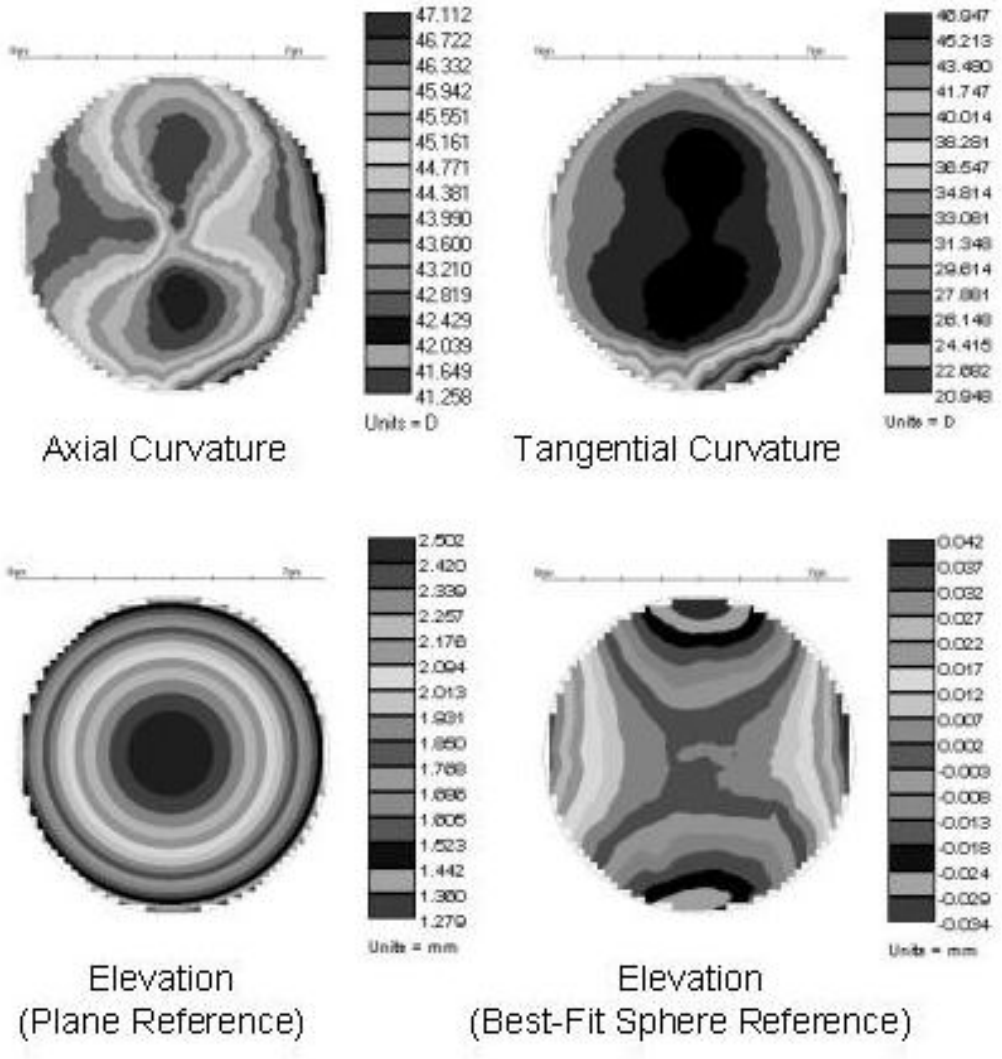

Figure 4.1: Different topographic descriptions of the same anterior corneal surface from the PAR Corneal Topography System

The central topography from a normal cornea can generally be described by the position and curvature of its steepest and flattest (principal) meridians, which are separated by 90° (Long, 1982). This variation in the central radius of curvature (R) can be described by a function that varies sinusoidally with the azimuthal angle (θ) as

$$R(\theta) = R_1 \cos^2(\theta - \theta_1) + R_2 \sin^2(\theta - \theta_1) \qquad 4.1$$

where R_1 and R_2 are the radius of curvature of the principal meridians and θ_1 denotes the position of R_1.

The relationship defined in equation 4.1 can be used to transform a spherical surface into a new rotationally asymmetric surface. This new surface is defined by two spherical profiles situated on perpendicular meridians and I refer to it as a bisphere. I define bispheric sag (Z_{BS}) as

$$Z_{BS}(r,\theta) = R_1 \cos^2(\theta - \theta_1) + R_2 \sin^2(\theta - \theta_1) - \sqrt{(R_1 \cos^2(\theta - \theta_1) + R_2 \sin^2(\theta - \theta_1))^2 - r^2} \qquad 4.2$$

where r and θ are the radial and angular components of a polar coordinate system. θ_1 is the angular offset of the bisphere's principal meridians from the xy-coordinate axes. Along meridian $\theta = \theta_1$ the surface has a spherical profile defined by a radius of curvature of R_1. The profile along the perpendicular meridian ($\theta = \theta_1 + 90°$) is a spherical section with a radius of curvature of R_2. Between these principal meridians the radius of curvature varies between R_1 and R_2. In the special case where $R_1 = R_2$ equation 4.2 simplifies to the spherical equation defined in equation 2.8.

The bispherical surface can be made more complex by symmetrically aspherizing it. This is accomplished by adding an asphericity parameter (Q). The sag of a bispherical surface with a single asphericity parameter (Z_{BS1Q}) is

$$Z_{BS1Q}(r,\theta) = \frac{(R_2 \cos^2(\theta - \theta_1) + R_1 \sin^2(\theta - \theta_1))r^2}{R_1 R_2 + \sqrt{R_1^2 R_2^2 - ((1+Q)(R_2^2 \cos^2(\theta - \theta_1) + R_1^2 \sin^2(\theta - \theta_1)))r^2}} \qquad 4.3$$

For this surface R_1 and R_2 represent the apical radius of curvature along the principal meridians. The asphericity parameter describes how the curvature along any meridian changes for points away from the apex similar to a conic surface.

Another more complicated surface can be defined if the asphericity parameter from the BS1Q surface varies between the two principal meridians along with the apical curvature. This surface is a termed a biconic since it is defined by two conic profiles situated on the principal meridians. Biconic sag (Z_{BC}) is defined as

$$Z_{BC}(r,\theta) = \frac{(R_2 \cos^2(\theta-\theta_1) + R_1 \sin^2(\theta-\theta_1))r^2}{R_1R_2 + \sqrt{R_1^2R_2^2 - ((1+Q_1)R_2^2\cos^2(\theta-\theta_1) + (1+Q_2)R_1^2\sin^2(\theta-\theta_1))r^2}} \qquad 4.4$$

θ_1 is now the angular offset of the biconic's principal meridians from the xy-coordinate axes. Along meridian $\theta = \theta_1$ the surface has a conic profile defined by a central radius of curvature of R_1 and an asphericity of Q_1. The profile along the perpendicular meridian ($\theta = \theta_1 + 90°$) is a conic section with a central radius of curvature of R_2 and an asphericity of Q_2. Between these principal meridians the radius of curvature at the apex varies between R_1 and R_2 and the asphericity varies between Q_1 and Q_2 (Schwiegerling and Snyder, 1998). In the special case where $R_1 = R_2$ and $Q_1 = Q_2$ equation 4.4 simplifies to the symmetrical conic defined in equation 2.10.

4.2.2 Topography Measurement Techniques

Increases in computing speed and optical technology such as digital video, along with the emergence of refractive surgery have led to the modern techniques used to measure corneal topography. The current techniques can be categorized by the optical phenomenon used in their measurement such as specular reflection, diffuse reflection or scattered light (Mejia-Barabosa and Malacara-Hernandez, 2001). This section will not describe all the possible measurement techniques that have been developed, but only the most common methods that are used clinically.

The specular reflection technique assumes the anterior corneal surface reflects like a convex mirror and is utilized most frequently in videokeratoscopy. This technology is the evolution of both keratometry and keratoscopy. It measures topography by projecting an illuminated Placido disk onto the corneal surface. A digital camera focussed on the image plane of the cornea captures the reflected image (Figure 4.2). Instrumental optics are designed so that each ring segment is imaged by a small region of the cornea. Analysis of the size and/or displacement of each individual ring segment in the captured image provide a measurement of the angle of the reflected light incident on the corresponding corneal surface. This information is used to calculate an estimate of the surface tangent.

A variety of different commercial videokeratoscopes have been developed with their own unique implementations of the technique. The original algorithms used to reconstruct the corneal surface were spherically biased (Roberts, 1994). These algorithms along with the limitations of axial curvature and the transfer of curvature data into elevation are a significant source of systematic error.

One of the more popular, early, videokeratoscopes is the Topographic Modeling System (TMS) (Tomey Corp.). Its original configuration, the TMS-1 has been utilized for various studies of corneal shape, which will be described in later sections and chapters. It has been shown that the TMS-1's elevation topography provides of good description of uniform, spherical surfaces but is unable to accurately represent non-uniform surfaces that contain changes in curvature (Applegate, et al., 1995; Priest and Munger, 1998). Subsequent improvements in the software of the TMS-1 have been shown to improve its ability to accurately measure rotationally symmetric conic surfaces (Hilmantel, et al., 1999). Since the cornea possesses an irregular, aspherical surface that is not rotationally symmetric any estimates of its shape by the TMS-1 may contain a significant amount of error.

Diffuse reflection techniques determine surface topography by analyzing the distortion of a known pattern projected onto the unknown surface. These techniques provide a direct measurement of elevation topography and do not suffer from the assumptions needed to derive corneal shape from curvature data. In theory, this advantage should provide a more accurate representation of surface shape than videokeratoscopy.

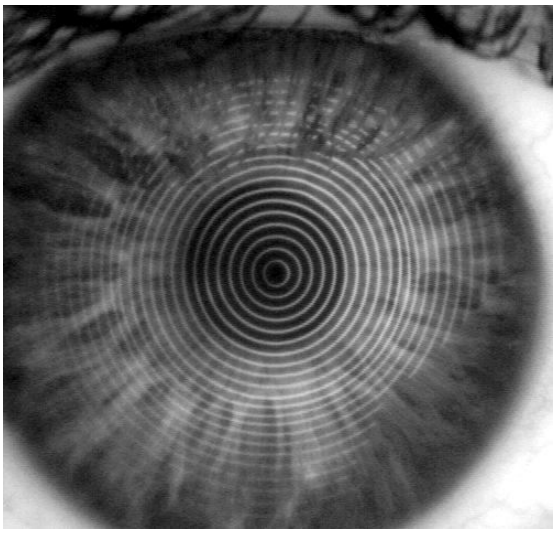

Figure 4.2: Image of Placido rings reflected from the corneal surface.

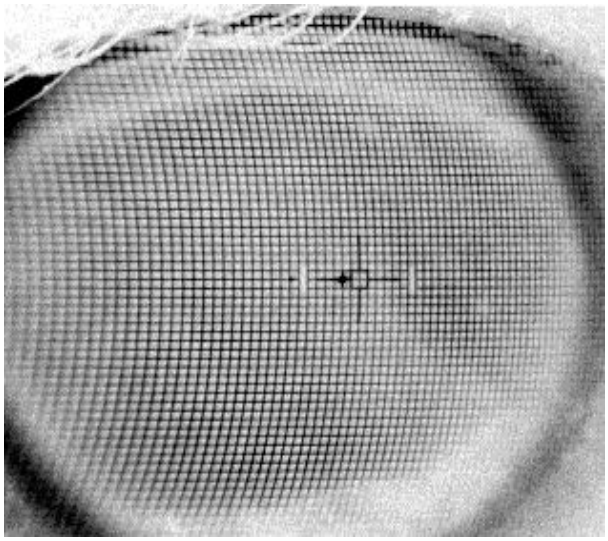

Figure 4.3: Diffusely reflected PAR grid image

One implementation of utilizing diffuse reflection is the PAR Corneal Topography System (PAR Vision Systems Corp.). It projects a two-dimensional grid with a sampling density of approximately 0.2 mm onto a cornea infused with fluorescein. Illumination through a blue excitation filter is used to stimulate fluorescence at the anterior surface of the cornea. Consequently, the cornea is an extended source emitting an image of the grid distorted by the corneal surface (Figure 4.3). Measurement of the grid is observed, by a CCD camera, through a yellow barrier filter to eliminate specular reflections. Corneal elevation at any point on the grid can be determined from the geometry of the measured grid position and instrumental optics.

Quantification of PAR measurements has shown it to provide an accurate description of both uniform and non-uniform shapes. Compared to the TMS-1, it provides a significantly more accurate representation of surfaces containing changes in curvature (Priest and Munger, 1998). Consequently, it promises better accuracy when measuring corneal surfaces.

A similar technique of utilizing scattered light evolved from the slit-lamp. The slit-lamp is a diagnostic instrument that projects a sharp, bright image of an adjustable slit over any portion of the eye. When the slit image passes through the cornea, it splits into a specular reflection and a

refracted beam. The refracted beam penetrates the surface and is scattered by the tissue of the cornea. Since the scattering phenomenon in the tissue of the cornea is stronger than in the aqueous, the image of the light in the cornea layer is observed as a curved bright band (Figure 4.4). The outer and inner edges of this band are said to correspond to the anterior and posterior surfaces of the cornea (Mejia-Barabosa and Malacara-Hernandez, 2001). An image of the scattered light can be used to determine the elevation topography of the anterior and posterior corneal surfaces based on the geometry of the optical system.

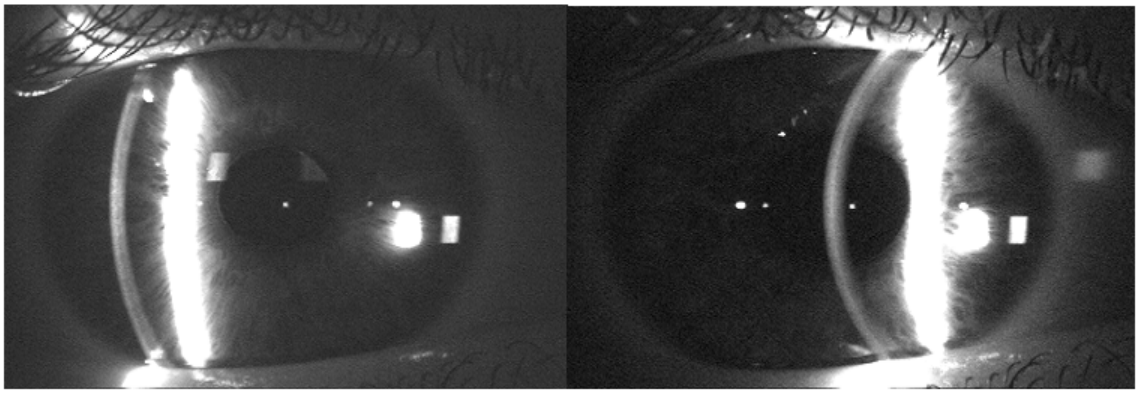

Figure 4.4: Orbscan Slit Images

This technique has been combined along with videokeratascopy in a clinical instrument called the Orbscan II (Baush and Lomb). Its optical acquisition head projects a vertical light slit onto the cornea, which is scanned across the eye from both the left and right sides. Twenty slit projections are sequentially acquired for each scan across the eye, providing a total of 40 interlaced images for computer analysis in several seconds. A tracking system monitors involuntary eye movements and mathematically accounts for them to piece together the mathematical surface being analyzed. The edges of the slit beam image are analyzed in all of the 40 images to detect both the anterior and posterior corneal surfaces. Elevation topography is then constructed from this data.

Analysis of calibrated spherical, conical and toroidal (bispherical) surfaces have shown that the Orbscan II can accurately measure the shape of a stationary surface that scatters light evenly

(Cairns, et al., 2002). This study did not address variables such as eye movement, light scatter, tear inconsistencies and surface irregularity would could effect the ability of the Orbscan II to accurately measure the anterior corneal surface of a human eye.

The performance of the Orbscan II on normal human corneas was evaluated by measuring the anterior corneal surface of 22 subjects (Cho, et al., 2002). Two repeated readings were taken by one examiner followed by a single measurement by a second examiner. The results indicated that two repeated measurements of the central power of the anterior corneal surface could differ by up to 2.5 D. Measurements of central power by two different examiners could differ by up to 3.5 D. The authors suggested that the repeatability and reproducibility of the Orbscan II is clinically unacceptable and the poor results could be caused by a lack of proper alignment between instrument and subject throughout the measurement process.

The accuracy of posterior corneal surface measurements made by the Orbscan II has not been established.

4.2.3 Previous Studies

Along with the emergence of techniques to measure corneal topography, there have been numerous attempts to investigate the variation in corneal shape within the human population. The accuracy of each study is limited by the measurement techniques used and the analysis that was performed. Within the past two decades several studies have examined corneal shape.

In the study by Kiely et al. (1982), the shapes of the anterior corneas from 176 eyes (88 subjects) were measured with an autocollimating photokeratoscope. The subjects' ages were evenly distributed between between 16 and 80 years and their refractive error was from -5 to 5 D. Measurements were first quantified by fitting each with a symmetrical conic surface. The average apical radius of curvature (R) was 7.72 ± 0.27 mm (7.06 to 8.64). The mean asphericity (Q) was -0.26 ± 0.18 (-0.76 to 0.47). A statistically significant, positive correlation was found between the R and Q values. Steeper central corneas were found to flatten out more rapidly.

To quantify the asymmetry of the anterior cornea, the measured data was also fit with a non-rotationally symmetric conic surface where the R and Q vary sinusoidally with meridian. The model assumed the maximum and minimum values of the R and Q lie in mutually orthogonal directions and was defined with equations similar to 4.23, 4.24 and 4.30. The range of the meridional R and Q values were from 6.94 to 8.74 mm and 1.28 to -1.44, respectively. There was a tendency (74% of the eyes) for the larger R-values to occur in the region of the horizontal meridian (±45°), which is referred to clinically as "with-the-rule astigmatism". 78% of the eyes had a difference between R-values of ≤ 0.3 mm. 80% of the eyes had a difference of ≤ 0.5 between the maximum and minimum Q-values but no specific trend was found for maximum Q to favour one meridian to another. The results indicated that R and Q of individual corneas can vary with azimuthal angle and an asymmetric conic could provide a more accurate representation of corneal shape than a symmetrical conic.

Guillon et al. (1986) reported on a study where the shapes, measured with a photokeratoscope, of the steepest and flattest meridians were described with a conic profiles. Profiles were determined by separately finding the best-fit conic for the principal meridians. This study included 220 eyes from 110 subjects. The subjects had a mean age of 33 ± 11 years (17 to 60). Their mean spherical refractive error was -1.0 ± 2.4 D (-15.0 to 3.5). Mean cylindrical error was -0.8 ± 1.0 D (0.0 to 5.0). Mean central radius of curvature was found to be 7.87 ± 0.25 mm (7.14 to 8.54) for the flattest meridian and 7.70 ± 0.27 mm (7.03 to 8.86) for the steepest meridian. The mean difference between R-values of the steepest and flattest meridians was found to be 0.17 ± 0.13 mm. The orientation of the flattest meridian revealed that 85.5% of the eyes exhibit "with the rule astigmatism". The mean asphericity of the flat and steep meridians was reported as -0.17 ± 0.13 (-0.79 to 0.20) and -0.19 ± 0.16 (-0.89 to 0.16) respectively. This study found the average difference between asphericity values of the flattest and steepest meridians was only 0.02 ± 0.15.

In a similar study, Douthwaite, et al. (1999) used a commercial videokeratoscope (EyeSys) to quantify the conic parameters of the principal meridians of the anterior corneal surface in 98 subjects. Their median age was 36 years (20 to 59). The refractive error of these subjects was not reported. The data analyzed from 90 right eyes revealed that the mean apical radius of curvature and asphericity of the near horizontal principal meridian were 7.93 ± 0.23 mm and -0.22 ± 0.12

respectively. The mean conic parameters (R & Q) for the near vertical principal meridian were found to be 7.80 ± 0.22 mm and -0.15 ± 0.15. Almost identical results were found for the corresponding data in 97 left eyes, which were not significantly different. A highly significant difference was observed between the two principal meridians in any individual eye. Within the age range in this investigation, age did not correlate with either the apical radius of curvature or asphericity of the principal meridians of the anterior corneal surface.

Recently, Douthwaite (2003) reanalysed his previous data set to determine if tilt in the corneal surface, with respect to the optical axis of the videokeratoscope, was affecting his measurement of apical radius of curvature and aphericity. His results revealed average tilts of 2.09 ± 3.02° for the near horizontal and 0.17 ± 4.58° for the near vertical principal meridians. The measured tilt did not affect apical radius of curvature measurements but asphericity decreased. The average asphericity was found to be -0.23 ± 0.10 and -0.18 ± 0.13 for the near horizontal and near vertical principal meridians of the right eye data. Similar results were found for the left eye data. No attempt was made to determine if the change in asphericity was statistically significant.

One of the limitations of the previous studies was no attempt was made to correlate shape parameters with refractive error. Carney et al. (1997) investigated this relationship. Their study included 113 eyes with a mean age of 27 ± 6 years (15 to 52). Spherical equivalent refractive error (SE) had a mean of -2.29 ± 2.15 D (-9.88 to 0.25). Refractive error was determined with manifest refraction. Corneal topography was measured with a TMS-1 and fit with a symmetrical conic surface. The mean apical radius of curvature was found to be 7.68 ± 0.27 mm (no range was reported). Mean asphericity was -0.33 ± 0.23 (-1.03 to 0.29). Results revealed that there is a statistically significant positive correlation between R and SE ($p = 0.008$). A statistically significant, negative correlation was found between Q and SE ($p = 0.005$). This study did not find a correlation between Q and R. ($p = 0.28$).

The correlation between refractive error and the central refractive power of the anterior corneal surface was also found in an investigation of 176 subjects (Goss, et al., 1997). This study included 53 emmetropes (-0.25 to 1.00 D), 115 myopes and 8 hyperopes. The mean age of the subjects was 26 ± 5 years (21 to 44). The power and refractive error of the near vertical principal meridian was determined by keratometry and retinoscopy. On average, myopes were found to have

steeper corneas (more power) than emmetropes ($p = 0.008$). A statistically significant correlation was found between refractive error and central corneal curvature in the measured meridians ($p < 0.001$).

Correlations between parameters describing refractive error and anterior corneal shape have also been investigated in a study involving 287 eyes from 150 subjects (Budak, et al., 1999). The average age of these subjects was 41 ± 12 years (8 to 71) and their mean spherical equivalent refractive error was -2.41 ± 3.70 D (-20.00 to 6.87). The subjects' refractive error was determined with manifest refraction and their anterior corneal topography was measured with a videokeratoscope (EyeSys). Shape parameters were defined as the effective (mean) refractive power of the central 3 mm diameter and anterior corneal asphericity was the mean value within the central 4.5 mm diameter. The mean effective refractive power and asphericity of the anterior corneal surface was found to be 43.86 ± 1.65 D (38.14 to 50.00) and -0.03 ± 0.23 (-0.90 to 0.82) respectively. Weak correlations were found between higher effective refractive power and lower asphericity values ($r = 0.15$) and myopic spherical equivalent refraction ($r = 0.21$). Highly myopic eyes (< -6.0 D) were found to have anterior corneal surfaces with significantly higher effective refractive power than eyes with moderate myopia (-2.0 to -6.0 D) or hyperopia (> 1.0 D) ($p < 0.001$). No correlation was found between asphericity and spherical equivalent refraction ($p = 0.21$) but eyes with moderate myopia had larger (more positive) asphericities than emmetropic eyes ($p = 0.003$).

Average changes in biometric parameters have also been observed with the progression of myopia in adolescents (Horner, et al., 2000). In this study, refractive error (subjective refraction), axial length (a-scan ultrasonography) and conic shape of the anterior corneal surface (videokeratoscopy) were observed, in 48 subjects, for 5 years. At the beginning of the study, the subjects ranged in age from 11 to 13 years, had mean myopia of -2.74 ± 1.51 D and mean asphericity of -0.08 ± 0.12 D. Central radius of curvature values were not reported. Over the period investigated, myopia increased by an average of 1.46 D, average axial length increased by 0.56 mm and asphericity increased by an average of 0.014. The change in axial length and asphericity were both found to individually correlate with the change in spherical equivalent refractive error. The contribution of the central radius of curvature to the increase in myopia was insignificant.

Attempts have been made to use rotationally asymmetric, geometric shapes to quantify the shape of the anterior corneal surface (Langenbucher, et al., 2002b; Langenbucher, et al., 2002c). One study uses a 3-dimensional ellipsoidal surface and determines the central curvature and asphericity of the principal meridians from the size of their semi-axes (similar to equations 3.1 and 3.2) (Langenbucher, et al., 2002b). In the other study a biconic surface (similar to equation 4.4) was used (Langenbucher, et al., 2002c). Both studies used their respective methods to quantify the shape of the anterior corneal surface by fitting videokeratoscopy measurements after keratoplasty.

Methods have been developed to fit corneal topography data with mathematical functions such as Fourier series (Hjortdal, et al., 1995; Raasch, 1995), Zernike polynomials (Schwiegerling, et al., 1995; Iskander, et al., 2001a), radial polynomials (Iskander, et al., 2002) and wavelets (Langenbucher, et al., 2002a). These techniques are particularly useful to characterize surfaces that do not resemble geometrical shapes. Fourier series have been used to analyze the amount of irregular astigmatism in rings of videokeratoscopic axial curvature data for normal, keratoconic and post surgery eyes (Hjortdal, et al., 1995; Raasch, 1995; Olsen, et al., 1996; Keller, et al., 1998; Oshika, et al., 1998; Hayashi, et al., 2000). Wavelets have been used to characterize the shape of corneas suffering from keratoconus (Langenbucher, et al., 2002a). Iskander et al. (2001b) have shown that a fourth order expansion of Zernike polynomials is generally sufficient to describe a normal cornea while kerataconic corneas that are significantly deformed require a larger number of terms. Zernike polynomials have also been used to analyze corneal shape after transplant surgery (Langenbucher, et al., 1999). While Zernike polynomials can describe the shape of normal corneas, it has been shown (Smolek and Klyce, 2003) that Zernike polynomials up to the tenth order do not accurately describe corneal aberrations in cases of keratoconus and postoperative keratoplasty.

Zernike polynomials have also been used to study how corneal shape changes with age (Guirao, et al., 2000). In this study, the average central radius of curavture (R) and asphericity (Q) of the cornea was calculated from a fourth order Zernike expansion of videokeratographic height data by

$$R = \frac{r_0}{2(2\sqrt{3}Z_2^0 - 6\sqrt{5}Z_4^0)} \qquad 4.5$$

$$Q = \sqrt{\left(8R^3 / r_0^4\right)\left(6\sqrt{5}Z_4^0\right)} - 1 \qquad 4.6$$

where r_0 is the maximal radial extent of the surface (Guirao and Artal, 2000). Measurements were obtained from 59 near emmetropic ($|SE| < 2D$) subjects of three age ranges: young (20-30 years), middle-aged (40-50 years) and old (60-70 years). The average corneal radius of curvature was found to decrease with age while the cornea became more spherical. Similar results were found in a study that fit videokeratoscopic data from the horizontal meridian of 20 young (14 to 33 years) and 20 older (45 to 84 years) subjects with a conic section (Pardhan and Beesley, 1999).

In a recent study, Preussner, et al (2003) compared how accurately a rotationally asymmetric conic shape and Zernike series of different orders fit topography measurements of the anterior corneal surface. Their rotationally asymmetric conic model was defined by first fitting a conic section to the height data of 360 semi-meridians from the topographic measurement of a videokeratoscope (Technomed C-scan). Their analysis was restricted to data from the central 6 mm of the corneal surface. Meridional central radius of curvature values were determined by averaging the values from semi-meridians spaced 180° apart. A $\cos^2$ function was fit to the meridian data to find the central radius of curvature (R_1, R_2) and orientation (θ_1) of the steepest and flattest (principal) meridians. It was assumed that R_1 and R_2 were positioned orthogonally. Finding the average sag of the measured surface, at 0.3 mm intervals from the centre, and fitting these values with a conic section determined an average asphericity (Q). The resulting asymmetric conic model, defined by R_1, R_2, θ_1, and Q, is similar to the bispherical surface with 1 asphericity parameter that I defined in equation 4.3. The topography data was also fit with two Zernike series (models). These series were inclusive to 4th order terms (Z4) and 8th order terms (Z8), which included 15 and 45 parameters respectively. The analysis was applied to the topography data of 100 normal eyes from 100 subjects with a mean age of 62 ± 18 years (18 to 88). The average root-mean-square differences between model predictions and measured height data was used to determine how accurately each model represented the measured data. The Z8 series provided a more accurate representation than the Z4 series but the asymmetric conic model was more accurate than either Zernike series. The authors suggest that in an individual case with strong deformation a Zernike model would clearly provide a better approximation but normally there is no need to approximate the shape of the anterior corneal surface with a Zernike polynomial series.

4.2.4 Jackson Cross Cylinder Description of Refractive Error

Refractive errors of the eye are specified by the power of the correcting lens required to render the eye emmetropic. The standard ophthalmic convention utilizes a sphero-cylinder lens described by its spherical power (S), cylinder power (C) and the cylinder axis (φ). Unfortunately, this description is not well suited for mathematical manipulation or statistical analysis (Thibos, et al., 1994).

The problem occurs for two reasons. First, the astigmatic component is specified in polar form, which is not convenient for even the simplest statistical computations. Secondly, a sphero-cylinder lens is not simply the sum of a spherical lens of power S and a cylindrical lens of power C. These components are not independent of each other since a cylindrical lens contains some spherical power. To solve this problem a Fourier analysis approach has been suggested (Harris, 1990, 1991, 1992; Thibos, et al., 1994).

Following Thibos et al., the optical power of a sphero-cylindrical lens varies sinusoidaly with meridian. Consequently, a simple Fourier series with a single harmonic component like

$$\mathrm{RE}(\theta) = \mathrm{S} + \mathrm{C}\cos^2(\theta - (\varphi + 90°)) \qquad 4.7$$

can be used to describe a subject's refractive error (RE). The 90° term is necessary since the angle φ describes the position of the cylinder axis and a cylinder's power axis is situated perpendicular to the cylinder axis.

In Fourier analysis, the trigonometric identity in equation 4.8 is used to transform equation 4.8 into equation 4.9

$$\cos^2(\phi) = (1 + \cos(2\phi))/2 \qquad 4.8$$

$$\mathrm{RE}(\theta) = \mathrm{S} + \frac{\mathrm{C}}{2} + \frac{\mathrm{C}}{2}\cos(2(\theta - (\varphi + 90°))) \qquad 4.9$$

Equation 4.9 displays the refractive error as a formal Fourier series, which contains a constant term (S+C/2) plus one harmonic term (C/2 cos(2(θ-(φ+90°)))). The benefit of the Fourier approach is that the constant term is mathematically independent of the cosine term since the basis functions of a Fourier series are mutually orthogonal.

Similar to the conventional description, the terms of the Fourier series also correspond to physical lenses. The constant term is a spherical lens while the cosine term describes the power profile of a Jackson cross-cylinder (JCC) lens of power C/2 with its axis inclined at the angle φ+90°. A JCC lens is made from a combination of a cylinder of positive power and a negative cylinder of the same power positioned perpendicularly.

To remove the remaining angular parameter in equation 4.9, the JCC lens can be replaced by two JCC lenses, one at axis 0° and the other at axis 45°. Mathematically this is achieved by using the trigonometric identity in equation 4.10 to transform equation 4.9 into equation 4.11.

$$\cos(\theta-\phi)=\cos(\theta)\cos(\phi)+\sin(\theta)\sin(\phi) \qquad 4.10$$

$$\mathrm{RE}(\theta)=\mathrm{RE}_{\mathrm{M}}+\mathrm{RE}_{\mathrm{J0}}\cos(2\theta)+\mathrm{RE}_{\mathrm{J45}}\sin(2\theta)$$

$$\text{where}\quad \mathrm{RE}_{\mathrm{M}}=\mathrm{S}+\frac{\mathrm{C}}{2} \qquad 4.11$$

$$\mathrm{RE}_{\mathrm{J0}}=\frac{\mathrm{C}}{2}\cos(2(\varphi+90°))$$

$$\mathrm{RE}_{\mathrm{J45}}=\frac{\mathrm{C}}{2}\sin(2(\varphi+90°))$$

By utilizing this Fourier analysis, any arbitrary refraction (sphero-cylinder lens) can be expressed as the sum of a spherical lens and two JCCs. Based on the refraction data, the spherical lens will have a power of RE_M. This is the mean power value and is commonly known as the spherical equivalent (SE). One of the JCC lenses will be orientated with the axis of the positive cylinder at 0° with a power of RE_{J0}. The other JCC lens has the axis of its positive cylinder at 45° and a power of RE_{J45}. These three power values can be used to completely describe any arbitrary

sphero-cylindrical lens. They do not have an angular component, are independent of each other and consequently do not suffer from the problems associated with the sphero-cylinder description.

In this chapter corneal topographies, measured with newer commercial instruments, will be quantified with biconic surfaces. A new description of corneal curvature, analogous to the JCC description of refractive error will be developed. Biconic surface and refractive error parameters will be expressed with JCC terms and compared with each other to determine if any correlations exist. The results will then be used, in the next chapter, in an attempt to develop more accurate eye models.

4.3 Methods

The corneal topographies used in this investigation were obtained from either myopic laser refractive surgery patients or emmetropic young adults. Their topographies were measured, at the University of Ottawa Eye Institute, on either the PAR CTS or Orbscan II. The refractive error of these subjects was determined by manifest refraction.

Topographies were obtained from a total of 206 eyes from 118 subjects. 159 eyes from 93 subjects were measured on the PAR CTS. Measurements on 47 eyes from 25 subjects were from the Orbscan II.

To test the efficacy of the fitting procedure (section 4.3.1) height data from a group of 12, randomly selected topographies were fit with spherical, conic, bispherical, bispherical with a single asphericity parameter and biconic surfaces. The RMSE from each fit were compared. F-tests were performed to determine if increased accuracy provided by the more complex surfaces was statistically significant. For simplicity, this procedure will be referred to as the shape test for the remainder of this thesis.

On the basis of the results of the first 12, the 206 topographies were fit with a biconic surface. A new terminology was developed so that the refractive error of the subjects and the results from their biconic fits could be described in Jackson Cross Cylinder terminology (section 4.3.2). The biconic JCC parameters were tested to determine if the necessary approximation was accurate enough. In cases where the difference between the approximation and the actual surface was deemed to be too large, the topographies were removed from the remaining analysis.

Initially all refractive error and corneal shape descriptions were in the conventional right-handed coordinate system. In this system, the positive x-axis is directed nasally for OD eyes while the negative x-axis points nasally for OS eyes. Due to a tendency to bilateral symmetry between OD and OS eyes, a descriptive function (F(x,y)) with odd symmetry about the y-axis would make F(x,y) for an OD eye the same as F(-x,y) for an OS eye (Thibos, et al., 2002).

To facilitate the analysis of OD and OS eyes together, a binasal coordinate system was used. In this system the positive x-axis is directed nasally for all eyes (Jalie, 1984). The transformation to a binasal system involves changing the sign of all x coordinates ($x \rightarrow -x$) for data from OS eyes. Since the refractive error and corneal shape are ultimately described with JCC terms, the transformation to a binasal system was accomplished by reversing the sign on all the J45 terms for all OS eyes. This transformation is similar to the one proposed by Thibos, et al. (2002) for comparing the aberrations of OD and OS eyes described with Zernike polynomials.

The statistical software package Stata 7 (Stata Corporation) was used to calculate correlation coefficients between the shape and refractive error parameters. To determine if any correlations were statistically significant, linear regression with a Huber/White robust estimate of variance was used. This was justified because, in many cases, data points were from the two eyes of the same subject, which cannot be considered to be independent of each other even though they originate from different eyes. This test pools the data from a single subject into a cluster and then treats the clusters as if they are independent of each other.

4.3.1 Fit Procedure

Most commercial corneal topographers provide a method of exporting their elevation data in a numerical format. The PAR CTS exports its data points in a rectangular array with approximately 0.2 mm spacing. Its reference plane is situated behind the cornea so the corneal apex has the highest elevation.

The Orbscan II system can export height data in a variety of formats. A format very similar to the one employed by the PAR CTS was chosen. The main difference was the Orbscan II specified the corneal apex as the origin of their spatial coordinate system.

A similar coordinate system was set up for the PAR CTS data by specifying the data point with the highest elevation (apex) as the origin. Data points lying within 2.5 mm radius of the apex were used in the fitting procedure.

To eliminate the assumption that the specified points were the actual corneal apex, coordinate offsets (x_o, y_o, z_o) were added to the fit equations so the apex of the best fit surfaces were not forced to coincide with the apex of the measured data. Polar coordinates (r, θ) were then defined as

$$r^2 = (x - x_o)^2 + (y - y_o)^2 \qquad 4.12$$

$$\theta = \arctan\left(\frac{y - y_o}{x - x_o}\right) \qquad 4.13$$

where x_o and y_o describe the offset of the surface apex from the origin of the coordinate system.

The fit equations used were similar to the sag equations of the previously defined surfaces (Z_S, Z_C, Z_{BS}, Z_{BS1Q} or Z_{BC}, equations 2.8, 2.10, 4.2 - 4.4) except for an offset (z_o) that represents the distance of the surface apex from the reference plane. As an example the fit equation for a biconic was

$$Z(r,\theta) = z_o - Z_{BC}(r,\theta) \qquad 4.14$$

To determine the residual variation of the data that was not fitted by the equations, the Root Mean Squared Error (RMSE) was calculated as

$$RMSE = \sqrt{\frac{\sum_{i=1}^{N} (residual_i)^2}{N}} \qquad 4.15$$

$Residual_i$ is the measured data minus the fit prediction at an individual data point. N is the total number of data points. The size of the RMSE indicates how closely the reference surface resembles the experimental data.

The parameters of the fit equations are determined, in custom software, by using a simplex algorithm to minimize the differences between the measured data and fit prediction. The simplex algorithm is very good at finding local minimum but it requires the fit parameters to be initialized

with appropriate values to find the best fit. The importance of the starting values depends on the number of parameters or degrees of freedom in the fit. For the rotationally symmetric surfaces there are only 4 or 5 parameters to fit and it was found that the value of the starting parameters had no affect on the results of the fit. The rotationally asymmetric surface fits have from 6 to 8 fit parameters. By varying the starting parameters and observing the RMSE, it was found that the simplex algorithm must be initialized with a good estimate of θ_1, to find the rotationally asymmetric surface prediction with the smallest RMSE.

Based on the following observations, a routine was devised to determine suitable estimates of R_1, R_2 and θ_1. The central topography from a normal cornea can be defined by the position and curvature of its steepest and flattest (principal) meridians, which are normally separated by 90° (Long, 1982). The predicted curvature from a spherical fit will lie near the average of the curvatures from the principal meridians. Consequently, the residuals from a spherical fit will have a characteristic "saddle-like" shape (Figure 4.5). Residuals from corneal areas that are flatter than the corresponding areas of the spherical fit will be positive. Conversely, steeper corneal areas will have negative spherical fit residuals. If the spherical fit residual surface is circumnavigated at a constant small radius from the origin, a sinusoidal pattern, with a frequency of 2 cycles/revolution, will be observed. Figure 4.6 displays this pattern of fit residuals measured from an emmetropic subject approximately 2mm from the corneal apex. Characterizing this pattern with a sinusoidal function will lead to estimates of R_1, R_2 and θ_1.

The procedure used to fit a biconic surface to corneal topographies is initiated by fitting a sphere to the measured data. A ring of data is then extracted from the residuals of the spherical fit at a constant radius (1.9 mm ≤ r ≤ 2.1 mm). This data is then fit with the cosine function

$$F(\theta) = F_0 + A \cdot \cos(2(\theta - \phi)) \qquad 4.16$$

A is the amplitude of the cosine function. F_0 represents a constant offset. ϕ is the angular offset which represents the location of the positive peak in the cosine fit. This peak corresponds to the position of the flattest meridian and is a good estimate of θ_1.

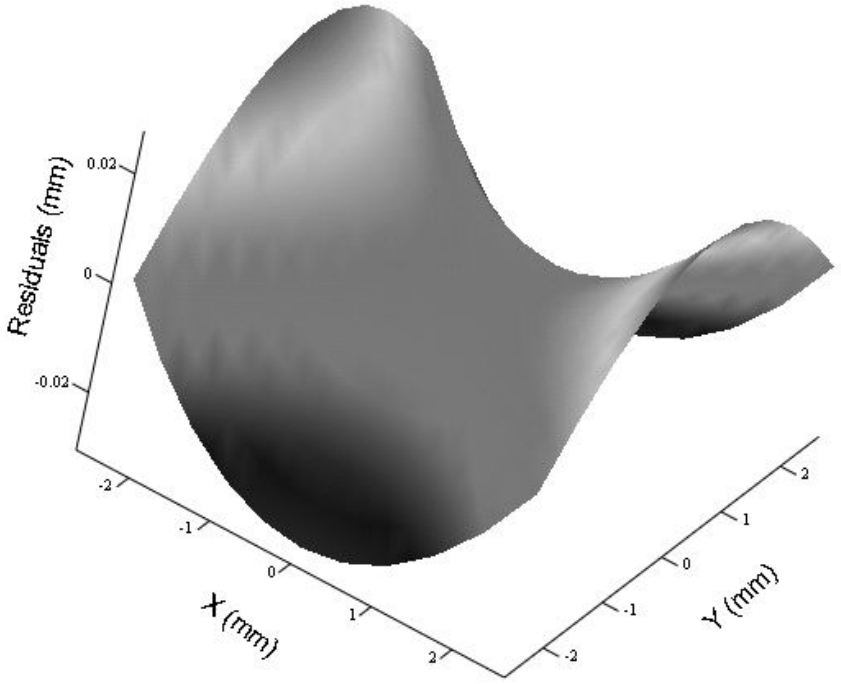

Figure 4.5: Residual surface of a spherical fit from a biconic surface

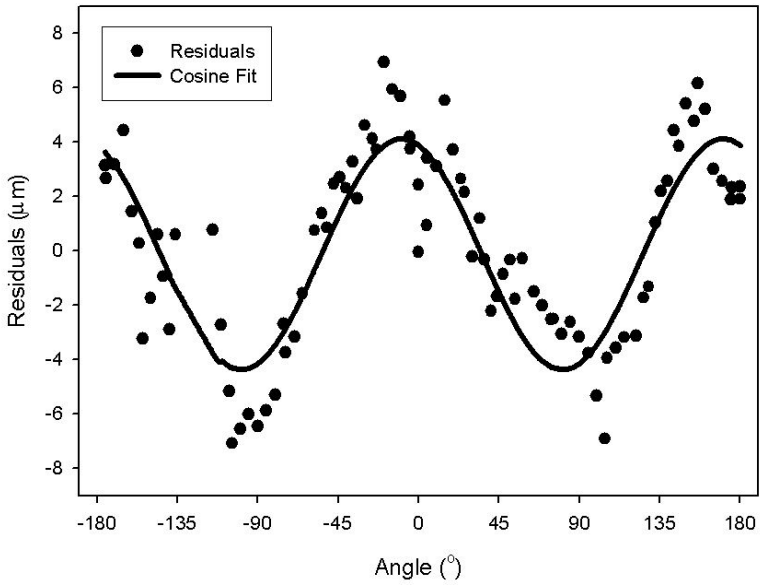

Figure 4.6: Ring of residual data from a spherical fit of an emmetropic subject measured on the PAR at approximately 2 mm from the corneal apex. The solid line is the best fit of a cosine function (equation 4.16) to the measured data.

To further enhance the biconic fitting procedure, estimates of R_1, the larger radius of curvature, and R_2 were made based on the amplitude of the cosine function and the radius of curvature of the spherical fit surface (R_S). This was accomplished by first assuming both principal meridians had a spherical profile ($Q_1 = Q_2 = 0$). If this were true then the amplitude of the cosine function would be the difference in sag values, at r = 2 mm, between the principal biconic meridians and the spherical fit surface and defined as

$$A = z_o - (R_1 - \sqrt{R_1^2 - 2^2}) - (z_o - (R_S - \sqrt{R_S^2 - 2^2})) \quad 4.17$$

$$-A = z_o - (R_2 - \sqrt{R_2^2 - 2^2}) - (z_o - (R_S - \sqrt{R_S^2 - 2^2})) \quad 4.18$$

R_1 and R_2 can then be estimated from

$$R_1 = \frac{(A - R_S + \sqrt{R_S^2 - 4})^2 + 4}{-2(A - R_S + \sqrt{R_S^2 - 4})} \quad 4.19$$

$$R_2 = \frac{(A + R_S - \sqrt{R_S^2 - 4})^2 + 4}{2(A + R_S - \sqrt{R_S^2 - 4})} \quad 4.20$$

Estimates of the asphericity parameters were based on previously published values of average corneal shape. Estimates of the coordinate offsets were determined from the spacing of the measured data and the position of the reference plane used by the topographic systems. The estimates of the biconic parameters were then used as the starting point, which allowed the simplex algorithm to find the best fit for each surface.

4.3.2 Jackson Cross Cylinder Theory for Corneal Shape

Once the corneal shape parameters have been established, comparisons will be made between them and the subject's refractive error to determine if any significant relationships exist.

To make comparisons between refractive error and corneal shape, it is logical to describe the corneal surface in terms of its refractive power. Since paraxial corneal shape varies sinusoidally with meridian, like refractive error, an attempt will be made to try to describe corneal shape with a function consisting of JCC components.

Surface shape is related to paraxial refractive power by

$$P(\theta) = \frac{n' - n}{R(\theta)} = c(\theta) \cdot (n' - n) \qquad 4.21$$

where c is the paraxial surface curvature, which is the reciprocal of the radius of curvature (R). n and n' denote the refractive indicies on either side of an interface. For the anterior corneal surface n is the refractive index of air (1) and n` is the cornea's refractive index (1.376).

The JCC description of the corneal surface is developed from the biconic sag equation (4.4). In terms of surface curvature, it appears as

$$Z_{BC}(r,\theta) = \frac{(c_1 \cos^2(\theta - \theta_1) + c_2 \sin^2(\theta - \theta_1))r^2}{1 + \sqrt{1 - ((1+Q_1)c_1^{\,2}\cos^2(\theta - \theta_1) + (1+Q_2)c_2^{\,2}\sin^2(\theta - \theta_1))r^2}} \qquad 4.22$$

where c_1 and c_2 are the paraxial surface curvatures along the principal meridians.

Following Schwiegerling and Snyder (1998), equation 4.22 can be written as

$$Z_{BC}(r,\theta) = \frac{c(\theta)r^2}{1 + \sqrt{1 - (1+Q(\theta))(c(\theta))^2 r^2}} \qquad 4.23$$

$$c(\theta) = c_1 \cos^2(\theta - \theta_1) + c_2 \sin^2(\theta - \theta_1) = c_1 + (c_2 - c_1)\sin^2(\theta - \theta_1) \qquad 4.24$$

$$Q(\theta) = \frac{(1+Q_1)c_1^{\,2}\cos^2(\theta-\theta_1) + (1+Q_2)c_2^{\,2}\sin^2(\theta-\theta_1)}{(c(\theta))^2} - 1 \qquad 4.25$$

where $c(\theta)$ and $Q(\theta)$ represent the central curvature and asphericity along the meridian at angle θ.

By applying the same procedure that was used with the refractive error, the JCC paraxial power profile of the corneal surface, near the vertex where Q ~ 0, can be determined as

$$P(\theta) = P_M + P_{J0}\cos(2\theta) + P_{J45}\sin(2\theta)$$

$$\text{where} \quad P_M = (n'-n)\left(\frac{1}{R_2} + \frac{1}{2}\left(\frac{1}{R_1} - \frac{1}{R_2}\right)\right) \qquad 4.26$$

$$P_{J0} = (n'-n)\left(\frac{1}{2}\left(\frac{1}{R_1} - \frac{1}{R_2}\right)\right)\cos(2\theta_1)$$

$$P_{J45} = (n'-n)\left(\frac{1}{2}\left(\frac{1}{R_1} - \frac{1}{R_2}\right)\right)\sin(2\theta_1)$$

The asphericity variation, equation 4.25, cannot simply be decomposed with Fourier analysis. To describe $Q(\theta)$ with JCC terms will require an approximation. Consider the difference between the maximum and minimum curvature values ($\delta c = c_2 - c_1$). The denominator in equation 4.25 becomes

$$\left(c(\theta)\right)^2 = c_1^{\,2} + 2\cdot\delta c\cdot c_1\sin^2(\theta-\theta_1) + \delta c^2\sin^4(\theta-\theta_1) = c_1^{\,2}\left[1 + \delta c/c_1\sin^2(\theta-\theta_1)\right]^2 \qquad 4.27$$

Equation 4.25 can be written as

$$Q(\theta) = \frac{Q_1\cos^2(\theta-\theta_1) + Q_2\sin^2(\theta-\theta_1)) + \delta c/c_1\sin^2(\theta-\theta_1)\left(Q_2\cdot\left(2+\delta c/c_1\right) + \delta c/c_1\cos^2(\theta-\theta_1)\right)}{\left[1+\delta c/c_1\sin^2(\theta-\theta_1)\right]^2} \qquad 4.28$$

To simplify equation 4.28 its denominator is approximated as a binomial series and expanded in orders of $\delta c/c_1$ (equation 4.29). Orders greater than 2 have been dropped since their contribution to the overall value is negligible.

$$Q(\theta) \approx Q_1 \cos^2(\theta-\theta_1) + Q_2 \sin^2(\theta-\theta_1)) + 2\delta c/c_1 \left(Q_2 - Q_1\right)\sin^2(\theta-\theta_1)\cos^2(\theta-\theta_1) \qquad 4.29$$

If it assumed that $\delta c/c_1\left(Q_2 - Q_1\right)$ is small then equation 4.25 or 4.28 can be approximated by

$$Q(\theta) \approx Q_1 \cos^2(\theta-\theta_1) + Q_2 \sin^2(\theta-\theta_1) \qquad 4.30$$

If the assumption is applicable, the Fourier analysis can be applied to equation 4.30 and the asphericity variation can be described by

$$Q(\theta) \approx Q_M + Q_{J0}\cos(2\theta) + Q_{J45}\sin(2\theta)$$

$$\text{where} \quad Q_M = Q_2 + \frac{Q_1 - Q_2}{2} \qquad 4.31$$

$$Q_{J0} = \frac{Q_1 - Q_2}{2}\cos(2\theta_1)$$

$$Q_{J45} = \frac{Q_1 - Q_2}{2}\sin(2\theta_1)$$

Assumption validity was established by deriving an expression for the error in the approximation of Q and determining when the approximation would result in a significant difference in shape and consequently aberrations of the real and approximated surfaces.

By examining equations 4.25 and 4.30, the largest difference in asphericity and consequently surface shape and aberrations between the real and approximated surfaces will occur when $\theta - \theta_1 = 45°$. Along this meridian, surface shape can be described by the profile of a symmetrical conic where its central curvature (c), real and approximate asphericities (Q_R & Q_A) are

$$c = \frac{c_1 + c_2}{2} \qquad 4.32$$

$$Q_R = \frac{2(Q_1 c_1^{\,2} + Q_2 c_2^{\,2}) + (c_1 - c_2)^2}{(c_1 + c_2)^2} \qquad 4.33$$

$$Q_A = \frac{Q_1 + Q_2}{2} \tag{4.34}$$

The error in the approximation was found by first rewriting equation 4.33 as

$$Q_R = \frac{Q_1 + Q_2(1+\delta c/c_1)^2 + (\delta c/\sqrt{2}c_1)^2}{2(1+\delta c/2c_1)^2} \tag{4.35}$$

where $\delta c = c_2 - c_1$. The bracket in the denominator in equation 4.35 was then expanded as a binomial series.

$$Q_R = \frac{Q_1 + Q_2(1+\delta c/c_1)^2 + (\delta c/\sqrt{2}c_1)^2}{2}\left(1 - \frac{\delta c}{c_1} + \frac{3}{4}\left(\frac{\delta c}{c_1}\right)^2 + \cdots\right) \tag{4.36}$$

The error in the approximation is found by expanding equation 4.36 in orders of $\delta c/c_1$ (equation 4.37). Orders greater than 2 have been dropped since their contribution to the overall value is negligible.

$$Q_R = \frac{Q_1 + Q_2}{2} + \frac{Q_2 - Q_1}{2}\left(\frac{\delta c}{c_1}\right) + \frac{2 + 3Q_1 - Q_2}{8}\left(\frac{\delta c}{c_1}\right)^2 \tag{4.37}$$

The error term ($Q_E = Q_R - Q_A$) is seen to be

$$Q_E = \frac{Q_2 - Q_1}{2}\left(\frac{\delta c}{c_1}\right) + \frac{2 + 3Q_1 - Q_2}{8}\left(\frac{\delta c}{c_1}\right)^2 \tag{4.38}$$

It can be seen that the error term will be small when the variation of the asphericity times the percentage change in curvature is small, and the square of the fractional curvature variation is small. Consider the average values measured by Douthwaite, et al. (1999), (R_1 = 7.93 mm, R_2 = 7.80 mm, Q_1 = -0.22, Q_2 = -0.15). For these values δc = 0.002 mm^{-1}, $\delta c/c_1$ = 0.017 and Q_2-Q_1 =0.07. In terms of surface power the average difference between principal meridians is 0.79 D. Along the meridian bisecting the principal meridians, Q_R= -0.1844, Q_A = -0.1850 and Q_E = 0.0006. The difference between equations 4.33 and 4.37 is less than 0.1% of the value of Q_R, which shows that

using a binomial series expansion to calculate the asphericity approximation (Q_A) and the corresponding error (Q_E) is accurate for an average cornea.

$Q_R \approx Q_A$ will be a valid assumption if the aberrations of the real and approximated surfaces are not significantly different. A significant difference in aberrations can be determined by considering that an optical system is relatively aberration free if the Strehl ratio is greater than 0.8 (Smith and Atchison, 1997). In terms of the system's RMS it follows, from equation 2.7, that

$$(\mathrm{RMS})^2 < \lambda^2 / 20\pi^2 \qquad 4.39$$

If equation 4.39 is written in terms of the RMS and the denominator is rounded to an integer then

$$\mathrm{RMS} < \lambda / 14 \qquad 4.40$$

This is known as the Maréchal criterion (Smith and Atchison, 1997).

The largest difference in aberrations between the real and approximated surfaces is along the $\theta - \theta_1 = 45°$ meridian. The surface shape along this meridian is described by the profile of a symmetrical conic. The largest difference in aberrations will be estimated by comparing the SA of these symmetrical conic surfaces.

In general the aberrations of an optical system (W) can be quantified with a polynomial function. If the object is an on-axis point at infinity and the optical system consists of a symmetrical surface then the Taylor series expansion of high-order aberrations described by Smith and Atchison (1997) can be simplified to

$$W(r) = w_{4,0} r^4 \qquad 4.41$$

Schwiegerling and Synder (1998) have shown that

$$w_{4,0} = \frac{1}{8}\left(\frac{c^3 (n-1)(1+n^2 Q)}{n^2} \right) \qquad 4.42$$

for a conic surface with central curvature of c, asphericity of Q and a refractive index of n.

If a system's wavefront can be defined by equation 4.41, it can be shown by using equation 2.6 that

$$(\mathrm{RMS})^2 = {4(W_P)^2}\Big/{45} \qquad 4.43$$

where W_P is the wavefront error at the pupil edge. The criterion for this system to be aberration free can be expressed as

$$|W_P| < \frac{\lambda}{4} \qquad 4.44$$

This condition is sometimes referred to as the "quarter wavelength" rule (Smith and Atchison, 1997). I assume that if the real and approximate corneal surfaces differ in their optical path difference at the pupil edge (W_P) by less than ¼λ, they produce equivalent results and the approximation will not significantly change the aberrations.

Since the shape of any meridian in a biconic surface can be described with a conic function, the OPD along this meridian can be determined from equations 4.41 and 4.42. To determine if the difference in shape resulting from the asphericity assumption, given in equation 4.30, caused a significant change in aberrations, the OPD was calculated from equations 4.41 and 4.42, along the $\theta - \theta_1 = 45°$ meridian, for both the real and approximated surfaces of each subject. This calculation was performed at the pupil edge (r = 2.5 mm) where the OPD will be maximum, using the refractive index of the cornea (n = 1.376). The shape parameters (c, Q_R, Q_A) were calculated from the fit parameters (c_1, c_2, Q_1, Q_2) by using equations 4.32, 4.33 and 4.34. The absolute difference between the OPD (ΔW) of the real and approximated surfaces was then determined and expressed in wavelength units (λ = 633 nm). If any specific case was found to have ΔW > ¼λ along the $\theta - \theta_1 = 45°$ meridian assuming a 4th order variation of W, the JCC surface approximation was deemed to be invalid for this subject and it would not be appropriate to describe the biconic representation of their corneal shape with JCC terms. This analysis will also be used to set an upper limit on an acceptable value for Q_E.

4.4 Results

The results from the shape test show that the RMSE (Table 4.1) decreased for each subject as the complexity of the fit equations increased. The corresponding F-tests (Table 4.2) revealed that for each subject, a surface that is not rotationally symmetric produced a fit that was statistically significantly more accurate than the symmetric surfaces. The F-tests reveal that, in 8 of the 12 subjects a biconic surface provided a statisitically significantly better fit than the less complex surfaces. In 2 of the 12 subjects the biconic surface did not produce a statistically significantly better fit than the bispherical surface with a single asphericity parameter but these fit surfaces were statistically significantly better than the less complex surfaces. Likewise in another 2 of the 12 subjects the biconic and bispherical with one asphericity parameter did not produce a statistically significantly better fit than the bispherical.

Table 4.1: Shape Test Subject Information and RMSE Values

Subject	Age (years)	Eye	Sphere (D)	Cylinder (D)	Axis (°)	RMSE Values (μm)				
						S	C	BS	BS1Q	BC
1	30	OD	0.00	0.00	--	1.681	1.679	1.509	1.508	1.504
2	28	OD	-0.25	0.25	100	3.399	3.396	2.758	2.753	2.743
3	35	OD	-1.50	1.00	90	2.993	2.990	2.492	2.490	2.464
4	36	OD	-2.75	1.75	172	2.272	2.251	0.866	0.809	0.806
5	25	OD	-2.50	0.00	--	2.164	2.159	1.211	1.202	1.176
6	46	OD	-2.75	0.50	170	3.353	3.314	3.074	3.030	2.925
7	43	OD	-5.00	1.00	95	2.981	2.978	0.955	0.953	0.952
8	32	OD	-5.25	0.00	--	2.205	2.190	1.929	1.911	1.910
9	36	OD	-6.25	0.00	--	1.900	1.898	0.839	0.834	0.830
10	32	OD	-7.00	0.50	55	1.791	1.791	1.431	1.431	1.423
11	51	OD	-7.75	0.50	115	2.668	2.664	1.032	1.027	1.025
12	34	OD	-8.50	2.50	115	5.381	5.380	1.905	1.897	1.824

Table 4.2: Shape Test F-test Results. The shaded cells highlight cases where a more complex surface provides a statistically significantly better fit. For each subject a non-rotationally symmetric surface provided a statistically significantly better fit than the symmetric surfaces.

Subject	S vs. C		S vs. BS		C vs. BS		BS vs. BS1Q		BS vs. BC		BS1Q vs. BC	
	F	p-value	F	p-value	F	p-value	F	p-value	F	p-value	F	p-value
1	1.7	0.188	80.0	<0.001	--	--	1.1	0.285	2.2	0.108	--	--
2	1.2	0.268	172.8	<0.001	--	--	2.2	0.130	3.7	0.025	--	--
3	1.6	0.205	146.6	<0.001	--	--	1.1	0.293	7.7	<0.001	--	--
4	12.7	<0.001	--	--	3789.9	<0.001	96.5	<0.001	--	--	5.7	0.017
5	2.9	0.084	716.2	<0.001	--	--	9.5	0.002	--	--	29.5	<0.001
6	15.2	<0.001	--	--	106.1	<0.001	19.2	<0.001	--	--	47.5	<0.001
7	1.1	0.286	2889.7	<0.001	--	--	2.1	0.142	2.1	0.122	--	--
8	216.3	<0.001	--	--	187.3	<0.001	12.0	<0.001	--	--	0.6	0.437
9	1.1	0.285	1365.5	<0.001	--	--	8.3	0.004	--	--	5.3	0.020
10	0.1	0.781	184.0	<0.001	--	--	0.1	0.713	3.5	0.029	--	--
11	2.0	0.149	1844.0	<0.001	--	--	7.0	0.008	--	--	1.8	0.178
12	0.2	0.667	2261.1	<0.001	--	--	5.2	0.022	--	--	52.8	<0.001

Of the 159 eyes from 93 subjects measured with the PAR CTS only 8 eyes from 8 different subjects were found to have a $\Delta W > \frac{1}{4}\lambda$ when the asphericity approximation, needed to describe their biconic fits in JCC terms, was tested (Table 4.3). The ΔW for these eyes were all less than 0.3λ. When P_1 and P_2 are the powers in each of the principal meridians, the error in the asphericity approximation (Q_E), the change in the paraxial power ($\Delta P = P_2 - P_1$) and the asphericity ($\Delta Q = |Q_2 - Q_1|$) between principal meridians, of the biconic fits to the anterior corneal topography measurements, in each of these cases are much larger than the average values of $Q_E = 0.004 \pm 0.005$, $\Delta P = 1.21 \pm 0.85$ D and $\Delta Q = 0.38 \pm 0.32$ for the rest of the subjects. The value of the error term Q_E (equation 4.33) in each case was smaller than 0.04.

To determine if the PAR CTS and Orbscan II provide equivalent results, a comparison was made between their measurements of the same eye. Two eyes from two different subjects had three consecutive measurements taken on each instrument. The measurements were all found to pass the asphericity approximation test. The comparison was performed with a repeated measures analysis of variance. This test revealed that there was a statistically significant difference in the P_{J0} and Q_{J0}

parameters (p-values of .01 and .004, power of .99 and 1.0 respectively) in the first eye that was tested. No statistically significant difference was found for the remaining shape parameters of the first eye and in all the shape parameters of the second eye (p-values > .05, power < 0.8). In only the two instances where a statistically significant difference was found, was the power of the performed test greater than the desired power of 0.8. The results of these tests did not inspire enough confidence to believe that these instruments provided equivalent measurements and consequently the measurements made with the Orbscan II have been excluded.

Table 4.3: Cases that Violate the ¼ λ Rule. ΔW is the maximum absolute difference between the OPD of the real and approximated surfaces. Q_E is the error in the asphericity approximation. ΔP and ΔQ are the change in the paraxial power and asphericity between the principal meridians.

Sub	Eye	Sphere (D)	Cylinder (D)	ΔW (λ)	Q_E	ΔP (D)	ΔQ
1	OD	-2.75	0.50	0.274	0.038	2.50	1.55
2	OS	-4.25	1.00	0.251	0.039	3.75	0.97
3	OS	-4.50	0.75	0.261	0.036	3.34	1.07
4	OD	-5.00	0.75	0.277	0.038	5.23	0.80
5	OD	-6.00	1.00	0.254	0.039	4.46	0.81
6	OS	-6.25	1.00	0.255	0.036	3.54	0.99
7	OD	-7.00	0.50	0.260	0.035	3.42	1.02
8	OS	-11.00	2.25	0.287	0.038	3.95	1.01

Statistics on the remaining 151 eyes from 92 subjects and results from their biconic fits are shown in Table 4.4. The correlation coefficients relating the JCC terms of the refractive error and biconic corneal shape are shown in Table 4.5. The linear regression results, from relationships with correlation coefficients with an absolute value that was approximately 0.2 or greater, are shown in Table 4.6 and were further tested for significance. The relationships with statistically significant correlations ($p<0.05$) are displayed in Figures 4.7 and 4.8.

Coefficients were also calculated to test for correlations between age and the JCC components of refractive error and anterior corneal shape. Results from the 151 eyes, whose anterior corneal shape was approximated with JCC components, revealed that a statistically significant correlation was found only between age and RE_M ($p = 0.025$). The age and RE_M

dependence was caused by the fact that the emmetropic eyes (RE_M > -1 D) in this group were all less than 30 years old. If the analysis was repeated after removing the 8 emmtropic eyes from 5 subjects the dependence between age and RE_M disappeared ($p = 0.5$). The correlations between age and the remaining JCC terms were still not statistically significant.

It should be noted that the age of the 151 eyes was not evenly distributed through its range (Figure 4.9). Any dependence that exists between age and the JCC components of the anterior corneal shape could be masked since a large majority of the eyes were between 30 and 40 years old. A second test for age dependence was performed on a group with a more even age distribution (Figure 4.10) and a smaller range of refractive errors. Correlation coefficients were calculated and tested for significance for the 48 eyes from 26 subjects whose RE_M was less than -2 D and greater than -4 D. For this group of eyes no statistically significant age dependence was found with any of the JCC components of refractive error or anterior corneal shape.

Table 4.4: Age, refractive error and biconic parameters of the 151 eyes whose topography was described with JCC terms.

	Age (years)	SE (D)	Cylinder (D)	R_1 (mm)	Q_1	R_2 (mm)	Q_2	θ_1 (°)
Average	38	-4.95	0.68	7.76	-0.24	7.60	-0.11	0.9
SD	9	2.20	0.68	0.24	0.31	0.28	0.32	17.9
Minimum	17	-9.75	0.00	8.44	0.56	8.44	0.66	62.3
Maximum	62	0.00	2.50	7.08	-1.42	7.01	-1.01	-48.6

Table 4.5: Correlation Coefficients. The highlighted coefficients were deemed large enough to test for statistical significance.

	RE_{J0}	RE_{J45}	P_M	P_{J0}	P_{J45}	Q_M	Q_{J0}	Q_{J45}
RE_M	-0.382	-0.146	-0.270	0.346	0.074	-0.202	-0.028	-0.093
RE_{J0}		0.222	0.186	-0.730	-0.017	0.124	0.049	0.076
RE_{J45}			-0.120	-0.162	0.043	0.075	0.011	0.135
P_M				-0.248	-0.033	-0.056	-0.025	0.084
P_{J0}					-0.033	-0.084	-0.481	-0.059
P_{J45}						-0.019	0.151	-0.198
Q_M							0.133	0.313
Q_{J0}								-0.043

Table 4.6: Linear Regression Results

Independent	Dependent	F(1,92)	p-value	R^2	Slope	Intercept
RE_M	RE_{J0}	14.68	< 0.001	0.146	-0.070	-0.149
RE_M	P_M	8.20	0.005	0.073	-0.203	48.085
RE_M	P_{J0}	12.55	0.001	0.120	0.081	-0.099
RE_M	Q_M	6.78	0.011	0.041	-0.023	-0.285
RE_{J0}	RE_{J45}	3.58	0.062	0.049		
RE_{J0}	P_M	2.65	0.107	0.035		
RE_{J0}	P_{J0}	148.58	< 0.001	0.532	-0.886	-0.318
P_M	P_{J0}	5.96	0.017	0.062	-0.078	3.345
P_{J0}	Q_{J0}	28.62	< 0.001	0.231	-0.212	-0.155
P_{J45}	Q_{J45}	4.75	0.032	0.059	-0.103	-0.010
Q_M	Q_{J45}	8.23	0.005	0.098	0.147	0.008

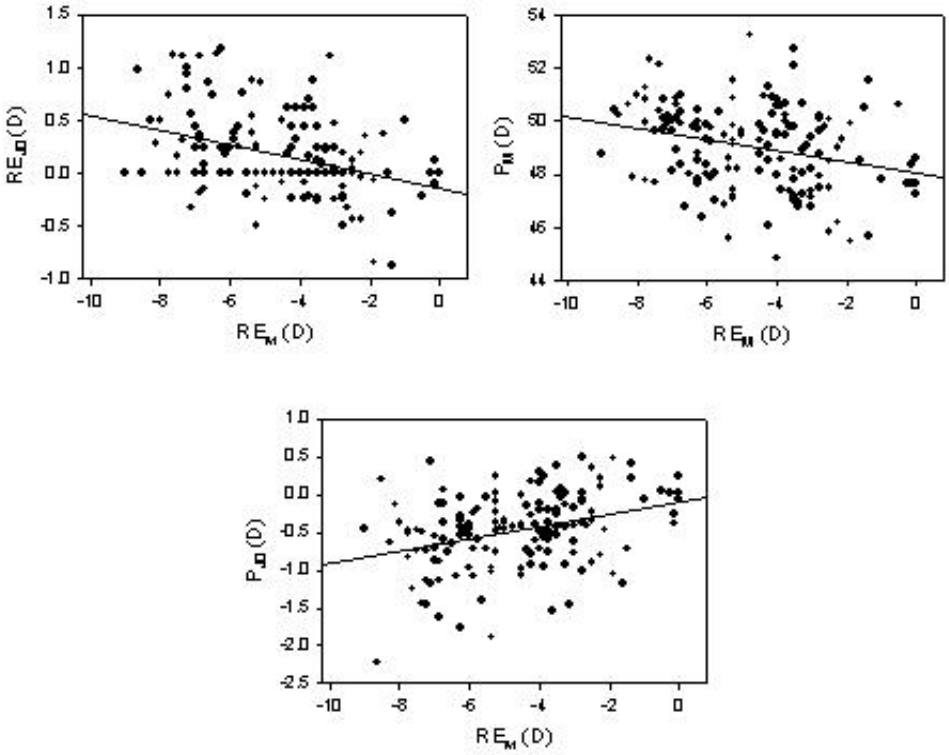

Figure 4.7: Data and Linear Fits for RE_{J0} vs. RE_M, P_M vs. RE_M, and P_{J0} vs. RE_M

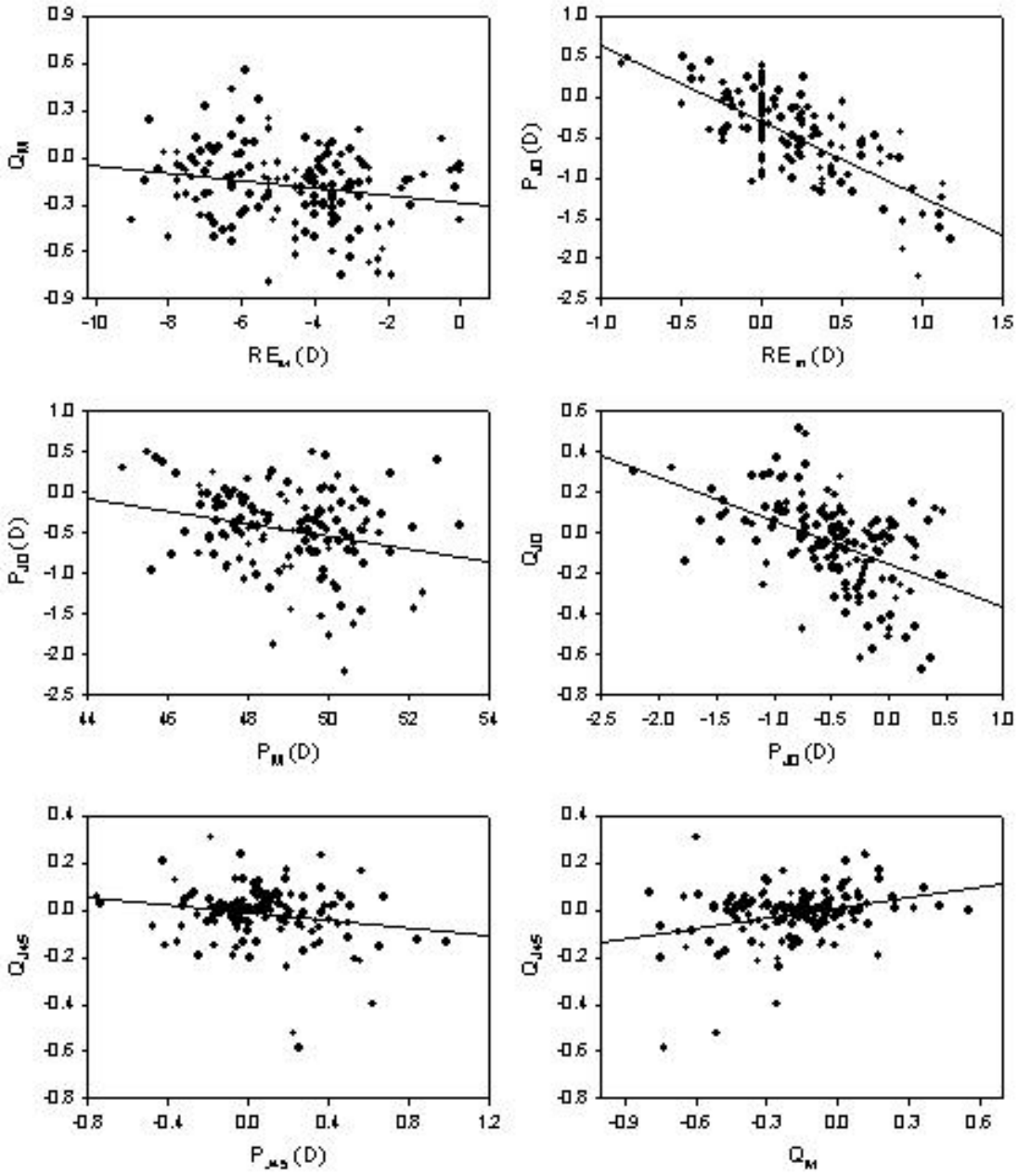

Figure 4.8: Data and Linear Fits for Q_M vs. RE_M, P_{J0} vs. RE_{J0}, P_{J0} vs. P_M, Q_{J0} vs. P_{J0}, Q_{J45} vs. P_{J45} and Q_{J45} vs. Q_M

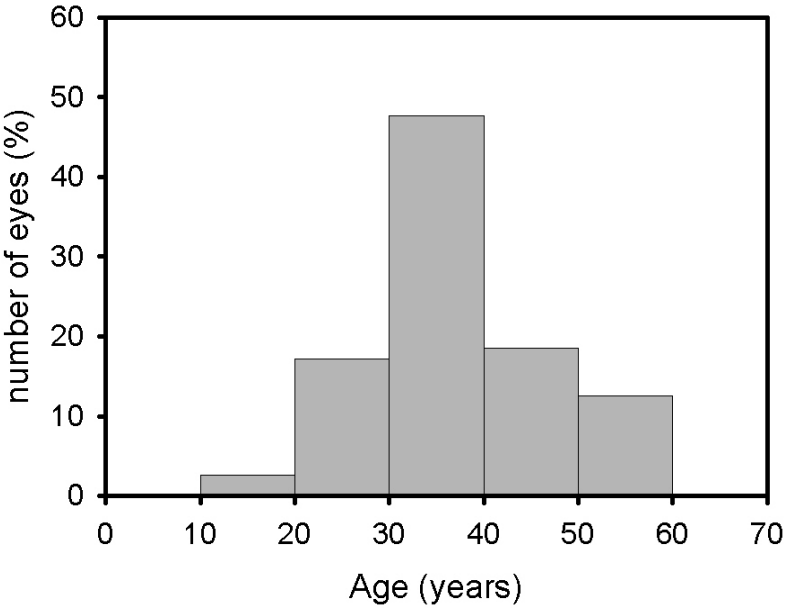

Figure 4.9: Age histogram of the 151 eyes whose anterior corneal shape was quantified with JCC components

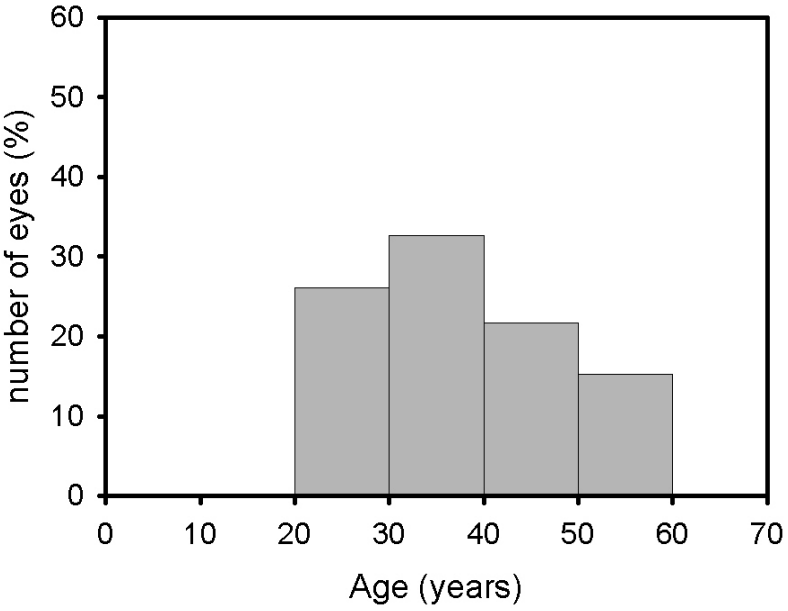

Figure 4.10: Age histogram of the 48 eyes whose RE_M was less than -2 D and greater than -4 D

4.5 Discussion and Conclusions

The results from the shape test show that the fit provided by a biconic surface was generally statistically significantly more accurate than the other surfaces tested. For the cases where the increase in accuracy provided by adding asphericity parameters to the bispherical surfaces was not statistically significant, the asphericity values of these surfaces were not significantly different from zero (Table 4.7). In the cases where the increase in accuracy provided by a biconic over a bispherical surface with a single asphericity parameter, was not statistically significant, it can be seen (Table 4.7) that the mean asphericity of the biconic is not significantly different from the asphericity of the BS1Q surface and the range in asphericity values in the biconic is small. These results are not surprising since the bispherical surface is just a biconic where the asphericity parameters equal zero and the bispherical surface with one asphericity parameter is just a biconic where the asphericity parameters are equal. In all cases the biconic fit had a smaller RMSE and the cases where this increase in accuracy was not statistically significant were because these individual corneas were either nearly bispherical or their asphericity parameters were nearly equal. Consequently, a biconic surface would provide the most accurate means, over all the surfaces tested, to describe the shape of normal corneas.

On average, the best-fit biconic parameters (Table 4.4) found in this chapter are similar to the results of previous studies but statistically significant differences do exist. There is not a statistically significant difference ($p=0.4$) between the mean central radius of curvature (7.68 ± 0.25 mm) determined from the JCC analysis in this investigation and the results from Kiely, et al. (1982), Carney, et al. (1997) and Budak, et al.(1999). A statistically significant difference ($p<0.05$) was found between the mean asphericity (-0.18 ± 0.24) found in this investigation and the results of Kiely, et al., Carney, et al. and Budak, et al. Studies that reported the average conic parameters of the principal meridians were also compared. A statistically significant difference ($p<0.05$) was found between the average central radius of curvature values in this study and the results of Guillon, et al. (1986) and Douthwaite, et al. (1999) for both principal meridians. A statistically significant difference ($p<0.05$) was also found for the average asphericity values for both principal meridians between the results from this study and those of Guillon, et al. A similar difference was not shared between the results

Table 4.7: Asphericity Parameters of the Rotationally Asymmetric Surfaces from the Shape Test. The shaded rows highlight cases in which the more complex surfaces were not found to provide a statistically significantly better fit.

	BS1Q	BC	
Subject	Q	Q_M	ΔQ
1	-0.080	-0.079	0.252
2	-0.195	-0.222	0.570
3	-0.131	-0.143	0.871
4	-0.448	-0.456	0.205
5	-0.160	-0.176	0.511
6	-0.560	-0.522	1.551
7	-0.058	-0.061	0.106
8	-0.278	-0.280	0.122
9	0.100	0.103	0.153
10	0.023	0.016	0.297
11	0.186	0.092	1.056
12	-0.118	-0.115	0.114

from this study and those of Douthwaite, et al. ($p>0.1$). The observed differences could be due to the different measurement techniques and analyses that were performed in the different studies and differences in the populations (like age and refractive error distributions for instance).

The myopic population studied in this chapter could also be different from other studies since these subjects had elected to undergo laser refractive surgery. While the myopic topographies were all acquired preoperatively, it's possible that they could be skewed from normal measurements and this could be the reason these subjects elected to have surgery. The age distribution could also make this study different from previous studies. Approximately 50% of the eyes, studied here, were between 30 and 40 years-old. Most of the previous studies did not discuss how age was distributed throughout their range and how this might affect the results.

It should be noted that many of the studies, compared for differences, contained data from two eyes from the same subject. This will adversely affect the statistical tests that were performed since two data points from the same subject cannot be considered to be independent. Proper test for significant differences could not be performed without access to the raw data. Despite this fact,

the analysis that was performed indicates that the data presented here is different from previous reports.

To facilitate the process of correlating corneal shape and refractive error, it was desirable to have these quantities defined with independent parameters. A Zernike polynomial expansion would provide a description with independent parameters and a 4th order series was found to be sufficient for describing a normal cornea (Iskander, et al., 2001b). An asymmetrical conic shape similar to the BS1Q surface was found to provide a more accurate fit of normal anterior corneal shape than 4th and 8th order Zernike series (Preussner, et al., 2003). Since I found a biconic was slightly more accurate than the BS1Q surface I concluded that a biconic would provide an accurate enough representation of normal anterior corneal shape. A method was then implemented to describe biconic shape with independent, JCC parameters.

Describing the refractive error and paraxial corneal power in JCC terms was a straightforward process. To describe the asphericity in JCC terms required the assumption that the error term in equation 4.38 was small. This occurred when the variation in paraxial corneal power with orientation was small or the variation in asphericity was small with a moderate variation in paraxial power. Based on the "quarter wavelength" rule a scheme was devised that determined if the biconic representation of individual corneal shapes could be described in JCC terms and simultaneously give an accurate estimate of wavefront error. Along with the maximum change in wavefront error (ΔW) associated with the approximated surface, the maximum error in asphericity (Q_E), the difference in paraxial power and asphericty (ΔP and ΔQ) were also calculated.

Of the 159 eyes tested only 8 eyes from 8 subjects were found to have $\Delta W > ¼ \lambda$. Even though these cases can be accurately described with a biconic surface (subject 1 was subject 6 in the shape test) it would not be appropriate to describe their shape in JCC terms and they were not included in the correlation analysis.

The eight excluded eyes were found to all have Q_E, ΔP and ΔQ values that significantly exceeded the average values of the remaining eyes (Table 4.3). It was also observed that if $\Delta W > ¼ \lambda$ then $Q_E \geq 0.035$. I conclude that an anterior corneal surface can only be accurately described as a biconic surface in JCC terms if the magnitude of the difference in its paraxial power and asphericity

between the principal meridians is not large enough to cause the maximum error in the asphericity term to exceed 0.035. No error larger than 0.04 was introduced into the asphericity term by the JCC approximation. This implies that if the allowable error in aberration were relaxed to $\Delta W < 1/3\ \lambda$, the JCC approxiamtion could be used for all normal corneas at a 5 mm pupil diameter.

The association between corneal power and refractive error has been well established. A weak but statistically significant correlation has been shown to exist, such that corneal power increases with increasing myopia (van Alphen, 1961; Garner, et al., 1990; Goss, et al., 1990; Goh and Lam, 1994; Grosvenor and Scott, 1994; Carney, et al., 1997; Goss, et al., 1997; Budak, et al., 1999). Consequently the correlation between RE_M and P_M was expected. Correlations between RE_{J0} and P_{J0} and RE_{J45} and P_{J45} would also be expected since the cornea is the most powerful optical element in the eye and the spatial distribution of its refractive power would be expected to greatly influence the spatial distribution of ocular power. While a very strong correlation was found between RE_{J0} and P_{J0}, no correlation was found between RE_{J45} and P_{J45}. The lack of correlation between the J45 terms may be due to the fact that only 18% of the eyes that were analysed had refractive cylinders that were located more than 20° away from the horizontal or vertical meridians. The size of the cylinder refractive error ($\leq$ 2.50 D) could also play a role.

No previous studies have used a non-rotationally symmetric surface descriptor to study how the shape of the anterior corneal surface changes with refractive error. Carney, et al. (1997) used linear regression to shown how a symmetrical conic descriptor of the anterior corneal surface shape changes with refractive error. The mean components from my asymmetrical study (RE_M, P_M, Q_M) correspond to the components of the symmetrical study (SE, P, Q). A comparison of the linear regression results of these studies is shown in Table 4.8. The slopes relating paraxial corneal power (P) to spherical equivalent (SE) are equivalent since the robust standard error (RSE) for my slope value was 0.07 while the difference between slopes is 0.032. Similarly the intercepts from this relationship are not significantly different since the RSE on my intercept value was 0.38 D and the difference was 0.33 D. The slopes relating Q to SE are equivalent while the intercepts are significantly different between these studies because I found RSE of 0.009 and 0.048 while the differences are 0.009 and 0.117 for the slope and intercept respectively. No specific tests for statistical significance could be performed since Carney, et al. did not report the standard errors of

their linear regression analysis. Neither study found a statistically significant correlation between central corneal power and asphericity.

The differences between the results of these two studies could be due to the statistically significant differences in the age of the subjects ($p<0.001$), except that age was not found to correlate with the results reported here. I believe it is more likely that the observed differences may be related to the different shape measuring techniques used by the TMS-1 and PAR CTS. Similar differences have been observed when these systems attempt to quantify the shape of calibrated aspheric test surfaces (Priest and Munger, 1998).

Contrary to the findings of this study and Carney, et al., Budak, et al. (1999) did not find any correlation between spherical equivalent refractive error and anterior corneal asphericity. This difference could be due to the range of refractive errors that were measured. Budak, et al. measured subjects with a wide range of refractive errors (-20.00 to 6.87 D) while this study and Carney, et al. included only emmetropes and moderate myopes (>-10 D). Budak, et al. did find that eyes with moderate myopia had more positive asphericities than emmetropic eyes which is the same trend observed by this study and Carney, et al.

Table 4.8: Comparison of Linear Regression Results

	Slope		Intercept		r^2		p-value	
	Priest	Carney	Priest	Carney	Priest	Carney	Priest	Carney
SE vs. P	-0.203	-0.235	48.09	48.42	0.073	0.067	0.005	0.008
SE vs. Q	-0.023	-0.032	-0.285	-0.402	0.041	0.076	0.011	0.005
P vs. Q	---	---	---	---	0.003	0.011	0.531	0.282

. The previously mentioned correlation between refractive error and central power of the anterior corneal surface reveals that anterior corneal shape plays a large role in determining the position of the eye's best focal plane. The asphericity of the anterior corneal surface is a large contributor to the eye's spherical aberration, which in turn affects the position of the best focal plane. Consequently, the asphericity of the anterior corneal surface would be expected to correlate with refractive error.

Even though there is no correlation between P_M and Q_M, statistically significant correlations were found between P_{J0} and Q_{J0} and P_{J45} and Q_{J45}. For a biconic surface defined in JCC terms, the variations of P and Q with azimuthal angle (θ) (equations 4.26 and 4.31) are similar. The minimum and maximum values of both P and Q will be located on the principal meridians. If both P and Q vary with azimuthal angle then a correlation between their J0 and J45 terms would be expected. The existence of these correlations in the empirical data further emphasizes that a biconic in JCC terms is a good descriptor of anterior corneal shape.

The statistically significant correlation between RE_M and RE_{J0} suggests that as the mean refractive error increased most subjects within this group have larger amounts of cylinder. This result has also been observed in two large populations (more than 2000 subjects in each) of all ages and may be due to increasing variance in astigmatism with increasing refractive error (Horner, et al., 2003). Consequently, it is not surprising that statistically significant correlations between RE_M and P_{J0} and P_M and P_{J0} were found since RE_M is correlated with P_M and RE_{J0} is correlated to P_{J0}.

Although the relations, given in Table 4.6, were statistically significant ($p<0.05$), the low coefficient of determination (r^2) indicates that only a small percentage of the variance could be accounted for by the correlation between these variables.

These results prove a rotationally asymmetric corneal shape versus refractive error model can be created. In the last chapter, refractive myopia was modelled by changing the central radius of curvature of the symmetrical, anterior corneal surface by 0.128 mm/D. The empirical results from Carney, et al., (1997) and this chapter found that the mean central radius of the curvature of the anterior corneal surface changed by 0.036 mm/D and 0.031 mm/D respectively. Based on the results from the symmetrical models, it can be seen that the empirical rate of change between the central radius of curvature of the anterior corneal surface and myopic refractive error will not account for the corresponding level of myopia. This indicates that a corresponding change in some other ocular parameters must also contribute to myopic refractive error. Axial length has been observed to increase with myopic refractive error (Carney, et al., 1997; Goss, et al., 1997). Results from this chapter suggest that the J0 component of central power and mean asphericity also change with refractive error. Eye models of cylindrical refractive error are also possible based on these results. It remains to be seen if utilizing a corneal model, based on the results from this chapter, will improve the previously defined eye models. This will be partially addressed in subsequent chapters.

5 Asymmetrical Models

5.1 Introduction

Chapter 3 described the development of average, young-adult, symmetrical, GRIN eye models as a function of myopia. These models were found to accurately predict the amount of symmetrical spherical aberration that has been observed in young adults. Due to their lack of asymmetrical aberrations, these models do not predict the overall amount of total high-order aberrations observed in young adults. Myopia was simulated through either a purely axial or refractive technique, which created myopic models that were not anatomically accurate. New models need to be developed which eliminate the inadequacies of the previous symmetrical models.

Studies of the wavefront aberration of human eyes have shown that there are real inter-subject differences in the amount and form of the measured aberrations. Generally, at moderate pupil sizes, asymmetric aberrations like coma are often more prominent in an individual eye than symmetrical (spherical) aberration (Charman, 1991a). If the wavefront errors of many eyes are averaged, then the results tend to display a much greater degree of rotational symmetry. The radial change in refractive power that can be deduced from such an average wavefront corresponds closely to that measured in experiments which assume only spherical aberration exists (Charman and Walsh, 1985).

As was described in Chapter 2, optical elements are not coaxial but a nominal optical axis and the line of sight, separated by an angle alpha (α), can be defined. Small tilts and decentrations of the crystalline lens and pupil from the nominal optical axis can then be identified. Artificial pupil decentration is known to produce marked degradation in optical performance for large pupil sizes (Van Meeteren and Dunnewold, 1983; Walsh, 1988; Artal, et al., 1996). The existence of angle α will affect the optical performance at the fovea (Van Meeteren, 1974; Van Meeteren and Dunnewold, 1983; Bing and Campbell, 1994; Atchison and Smith, 2000). In certain cases, pupil decentration could actually be helpful in reducing the aberrations of the eye at the fovea if the existence of angle α is considered (Bing and Campbell, 1994).

Pupil decentration with changing pupil size has been reported (Walsh and Charman, 1988; Wilson, et al., 1992; Yang, et al., 2002). Walsh made his measurements by aligning the limbus in photographic images. Pupil centration measurements by Wilson, et al. were made with respect to the achromatic axis and the limbus. Yang, et al. used the geometric centre of the cornea and the limbus as their reference.

The optical surfaces of the eye each reflect a portion of the incoming light, which forms a corresponding image. These reflected images, known as the Purkinje images, are usually referred to as PI, PII, PIII and PIV and arise from the anterior and posterior surfaces of the cornea and the anterior and posterior surfaces of the lens respectively. The fraction of incident light that is reflected from an optical surface is proportional to the refractive index change at the surface. Considering the refractive index change at the anterior corneal surface, 2.5% of the incident light will be reflected as PI. The refractive index changes within the eye are much smaller than at the anterior corneal surface and consequently PI is about one hundred times brighter than PII, PIII and PIV (Bennett and Rabbetts, 1989).

When all the ocular surfaces are aligned, the Purkinje images can be aligned along one direction. Conversely, as is normally found, if the ocular surfaces are not coaxial then the Purkinje images cannot be aligned. The relative positions of PI and PIV can be used to approximate a nominal optical axis (Le Grand and El Hage, 1980).

Tscherning (1924) first described the misalignment of the Purkinje images when he reported on lens tilt and angle α. He found angle α had a range of 4° to 7° in the horizontal meridian and 2° to 3° in the vertical meridian. This indicates that the line of sight is nasal and superior to the nominal optical axis defined by aligning Purkinje images PI, PIII and PIV.

Barry, et al. (1994a; 1994b) have utilized pattern evaluation of PI and PIV to determine ocular alignment. This work concentrated on measuring angle α at several fixation distances to investigate strabismus.

More recently Cui (1998) developed a relationship between the relative positions of PIII and PIV from PI as functions of lens tilt and decentration with respect to the cornea for the Gullstrand-Emsley (GE) unaccommodated eye model. The GE model consists of a single surface cornea and a

two surface lens with a constant refractive index and is adequate for calculating the positions of PI, PIII and PIV. PII was not included because it is difficult to empirically observe since it is dim and obscured by PI (Cui, 1998).

Calculation of the Purkinje image positions is accomplished by assuming their reflective surfaces behave like spherical mirrors. While the position of PI is simply determined by treating the anterior corneal surface like a convex mirror, the calculation of the other Purkinje image positions is complicated by the refracting surfaces that precede their reflecting surfaces. The calculation is simplified by replacing the optical surfaces with an equivalent spherical mirror. The images formed by the equivalent mirror will coincide with the image formed by the mirror and the refracting elements (Bennett and Rabbetts, 1989).

To perform the calculations, Cui defined an optical axis as the axis through the model cornea's apex, its centre of curvature and the centre of the pupil. This axis is identical to the optical axis of the centred, symmetrical eye model introduced in Chapter 3. In his models the origin of the coordinate system was set at the corneal apex and the optical axis served as a reference axis. The positions of the Purkinje images for the GE model were then determined as functions of lens tilt and decentration by paraxial calculations. Cui then rearranged his equations so that lens tilt and decentration could be derived from the relative positions of PIII and PIV from PI.

To empirically measure the tilt and decentration of the crystalline lens, pupil decentration and angle alpha, Cui (1998) used a Purkinje image photography system. This system included an imaging system, fixation target and four infrared light emitting diode sources that were used to create Purkinje images. The fixation target could be moved around a calibrated fixation plane that was perpendicular to the optical axis of the imaging system. The origin of the fixation plane was coaxial with the imaging system. The four Purkinje sources are equally spaced around the optical axis of the imaging system.

The measurement procedure Cui employed involved first aligning the subject until their PI images were equally spaced around the optical axis of the imaging system. The position of the fixation target was adjusted until the corresponding PI and PIV images were aligned. The line connecting PI and PIV was then used to define a nominal optical axis. Displacement of PIII from the nominal optical axis was then used to calculate lens tilt and decentration based on the equations

derived for the GE model. Pupil decentration was defined as the position of the geometrical centre of the pupil from the axis joining PI and PIV. The magnitude of angle α was determined from the position of the fixation target, which gives the aligned PI and PIV (this corresponds to the nominal optical axis). The position of the fixation target was measured relative to the origin of the fixation plane, which is the coaxially sighted corneal axis (this is the line joining the fixation point and the corneal Purkinge image). Cui argues that this angle will be close to the angle between the optical axis and the nodal axis. In turn for a distant fixation point, the nodal axis and the line of sight will be very close to parallel.

Utilizing this instrument, Cui (1998) reported measurements of the tilt and decentration of the crystalline lens, decentration of the pupil and position of the line of sight with respect to a nominal optical axis in the left eye of 21 emmetropic young adults that ranged in age from 17 to 35 years. The average age of these subjects was not reported. The mean values of these results are shown in Table 5.1. In the coordinate system used, the temporal and superior directions were considered positive.

Table 5.1: Average Values for the Misalignment of the Ocular Components. These values were determined from measurements made with respect to an axis joining PI and PIV.

	Horizontal		Vertical	
Misalignment Parameter	Average	SD	Average	SD
Lens Tilt (°)	0.88	0.97	-1.91	0.76
Lens Decentration (mm)	-0.05	0.06	0.12	0.05
Pupil Decentration (mm)	-0.31	0.19	-0.28	0.21
Angle α (°)	-5.25	0.96	-0.72	1.28

In another investigation, Marcos, et al. (Marcos, et al., 2001a) utilized a similar Purkinje image technique, to measure the pupil decentration, angle α and aberrations in 15 eyes from 9 normal subjects (aged 25-50, mean 34). Spherical refractive error ranged from 0 to -7D, and astigmatism from 0 to 1.5D. The total angle α measured ranged from 1.8 to 7.4°. Pupil decentration ranged from 0.05 to 0.40 mm. Average values were not reported. When the

misalignment parameters were correlated with the aberrations' RMS (excluding defocus) it was found that the magnitudes of angle α and pupil decentrations were individually not major contributors to the individual variability of the observed aberrations.

So far there have only been a few investigations involving asymmetry in eye models. Pupil decentration and the existence of an angle α have been used to produce coma in a reduced single-surface eye models (Thibos, et al., 1997). Simple symmetrical eye models, built from on-axis rotationally symmetric components have been shown to predict coma and larger amounts of RMS if their pupils are decentered (Atchison and Smith, 2000).

The only GRIN model with asymmetry is the model proposed by Liou and Brennan (1997). Liou and Brennan's model contained a pupil that was decentered 0.5 mm and an angle α of 5°. Both components were misaligned nasally from the optical axis. This model was used to calculate its modulation transfer function, which compared well to empirical data. There was no mention of the asymmetrical aberrations that the model predicted.

In the previous chapter it was shown that a more accurate description of the anterior corneal surface is obtained by using a rotationally asymmetrical shape. It was also shown how this surface changes with myopia.

This chapter describes the development of myopic, anatomically accurate, young adult, asymmetrical GRIN models. The goal is to develop a model that simulates myopia in an anatomically accurate fashion and to predict empirical asymmetrical aberrations while maintaining the accurate prediction of symmetrical aberrations that has already been established.

Investigations will concentrate on how tilting and decentering the crystalline lens and pupil, adding a line of sight away from the optical axis, utilizing a rotationally asymmetrical shape for the anterior corneal surface and simulating myopia by simultaneously changing both the corneal shape and axial length will affect the predicted aberrations. The aberrations predicted by the asymmetrical models will be compared to the young adult empirical aberrations and symmetrical model predictions that were introduced in Chapter 3.

5.2 Methods

The asymmetrical models described here are an extension of the symmetrical models introduced in Chapter 3. Optical component misalignment was based on the average values reported by Cui (1998). Since Cui's values were from left eyes while the empirical aberration data is from right eyes the directions of the misalignments were adjusted for bilateral symmetry. The adjustments consisted of changing the sign of the horizontal components since the nasal direction is positive in the conventional right eye coordinate system. Consequently the asymmetrical models described here are for right eyes.

Along with the equations described in the introduction to this chapter, Cui (1998) also developed an equation to calculate the angle between the line connecting PI and PIV (nominal optical axis for empirical measurements) and the optical axis of the centred eye for the GE model as a function of lens tilt and decentration. Cui's average empirical values for lens tilt and decentration predict that the average angle between the nominal optical axis and the optical axis of the centred eye would have an absolute difference of less than 0.1°. Since this value is so small I have assumed that the nominal optical axis in my asymmetrical models can be approximated by the optical axis of the centred eye. Figure 5.1 depicts the misalignment of the optical components in relation to the nominal optical axis.

The modeling process was initiated by sequentially adding the average misalignment parameters (Table 5.1) to the emmetropic symmetric model introduced in Chapter 3. First angle α was added by changing the field angle of the point object. Pupil decentration was added next by displacing its centre from the model's nominal optical axis. Lastly the lens was misaligned by tilting and decentering it with respect to the nominal optical axis. At each step the model's aberrations were calculated and compared to the empirical results.

The corneal shape changes described in Chapter 4 were then utilized to develop two sets of asymmetrical models as a function of refractive error. The first set had its anterior corneal shape described by a symmetrical conic (SC). The second set used a biconic (BC) shape for its anterior corneal surface.

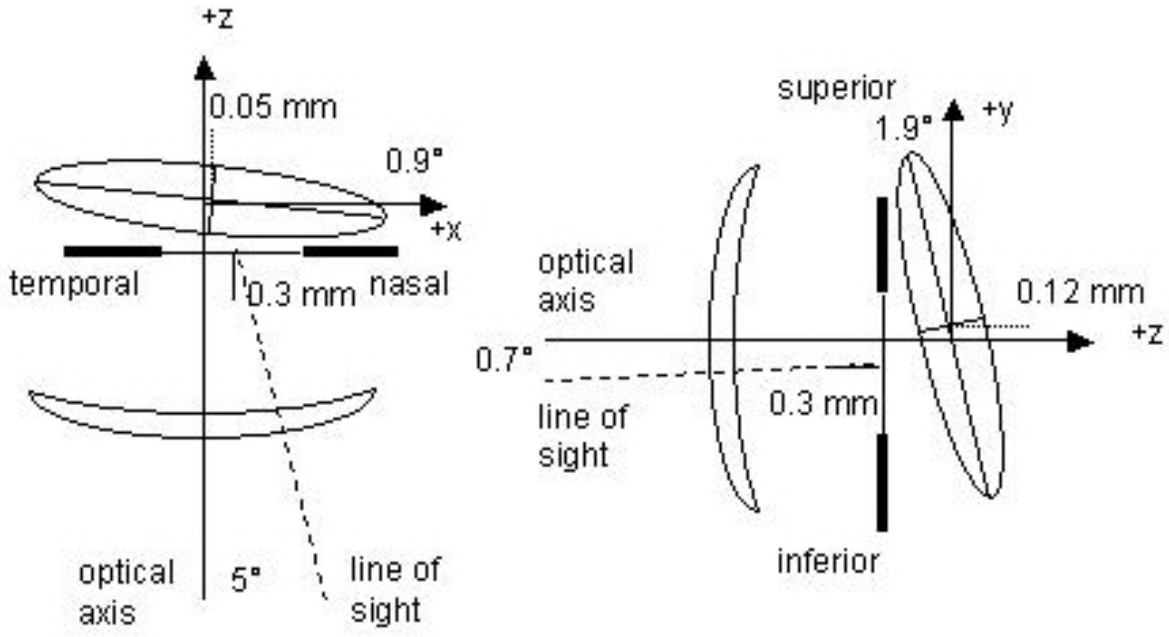

Figure 5.1: Misalignment of the Ocular Components. Angle α is the angle between the optical axes and line of sight. Pupil and lens decentration are defined as the distance separating their centres from the optical axis. Lens tilt is also referenced with respect to the optical axis. The numerical values depicted are defined in Table 5.1. In the coordinate system used, the nasal and superior directions were considered positive.

A couple of studies (Pardhan and Beesley, 1999; Guirao, et al., 2000) designed to investigate the dependence of anterior corneal shape on age found that the average corneal radius of curvature decreased with age while the cornea became more spherical. The corneal topography data in Chapter 4 was measured in a group of 151 eyes that ranged in age from 19 to 62 years. After removing 8 emmetropic eyes that were all less than 30 years old, no statistically significant correlations between age and refractive error or anterior corneal shape were found. This study was not designed to look for age dependence. The age of its subjects was not evenly distributed throughout its range, which could have masked an existing dependence, although in a similar study age was also not found to correlate with the shape of the anterior corneal surface (Douthwaite, et al., 1999). If the results from Chapter 4 are added to the model, the magnitude of corneal shape parameters may not be exactly anatomically accurate for a young adult. The possibility of adding an accurate relationship between corneal shape and refractive error, which may improve the model's ability to predict aberrations, is more important than absolute anatomical accuracy.

The anterior corneal shape of the SC models was determined by assuming the mean paraxial power (P_M) and mean asphericity (Q_M) from the biconic fits in Chapter 4 could represent the paraxial power and asphericty of the symmetrical conic surfaces. The necessary shape parameters could then be determined from the linear regression results between RE_M and P_M and RE_M and Q_M reported in Chapter 4. Central radius of curvature values were calculated from the paraxial power by rearranging equation 4.19. Table 5.2 displays the values that were used.

Empirical corneal topography results, in Chapter 4, were also used to create biconic anterior corneal surfaces. The empirical aberration data, originally introduced in Chapter 3, was from subjects with low amounts of cylinder (≤ 1.25 D). The difference in the paraxial power between the principal meridians of the anterior corneal surface of the 125 eyes from the topography subjects in Chapter 4 with cylinder values equal to or less than 1.25 D was 0.99 ± 0.60 D which is not significantly different from 1 D at a 0.05 significance level. Consequently, the models' biconic anterior corneal surfaces were designed to have a difference of 1 D between the paraxial power of their principal meridians.

The topography subjects, in Chapter 4, were also found to have average values of 0.03 ± 0.23 D, 0.06 ± 0.27 D and -0.02 ± 0.11 measured for RE_{J45}, P_{J45} and Q_{J45}, respectively. The J45 values are not significantly different from zero at a 0.01 significance level. Consequently the model's J45 terms from the JCC descriptions of anterior corneal shape were set to zero. This corresponds to locating the biconic's principal meridians on the x and y-axes.

The biconic shape parameters were calculated by first setting RE_{J0} equal to 0.50 D, which is equivalent to a 1 D difference in the paraxial power of the principal meridians. P_{J0} of the anterior corneal surface is then calculated from its linear regression relationship with RE_{J0} from Chapter 4. The paraxial power of the principal meridians was calculated from

$$P_2 = P_M - P_{J0} \qquad 5.1$$

$$P_1 = P_2 + 2P_{J0} \qquad 5.2$$

Asphericity was determined by first calculating Q_{J0} from its linear regression results with P_{J0}. The asphericity of the principal meridians was then determined from

$$Q_2 = Q_M - Q_{J0} \quad 5.3$$

$$Q_1 = Q_2 + 2Q_{J0} \quad 5.4$$

The biconic parameter values are also shown in Table 5.2.

Table 5.2: Anterior Corneal Shape Parameters

	SC Model			BC Model					
RE_M (D)	P_M (D)	R_M (mm)	Q_M	P_2 (D)	P_1 (D)	R_2 (mm)	R_1 (mm)	Q_2	Q_1
0	48.09	7.819	-0.285	48.85	47.32	7.698	7.945	-0.291	-0.279
-1	48.29	7.787	-0.262	49.05	47.53	7.666	7.911	-0.268	-0.256
-2	48.49	7.754	-0.239	49.25	47.73	7.634	7.878	-0.245	-0.233
-3	48.69	7.722	-0.216	49.45	47.93	7.603	7.845	-0.222	-0.210
-4	48.90	7.690	-0.192	49.66	48.13	7.572	7.812	-0.198	-0.186
-5	49.10	7.658	-0.169	49.86	48.34	7.541	7.779	-0.175	-0.163
-6	49.30	7.627	-0.146	50.06	48.54	7.511	7.746	-0.152	-0.140
-7	49.50	7.595	-0.123	50.26	48.74	7.480	7.714	-0.129	-0.117
-8	49.71	7.565	-0.100	50.47	48.94	7.450	7.682	-0.106	-0.094

The anterior corneal shape in the emmetropic symmetrical model, in Chapter 3, was based on empirical values averaged across a large range of refractive error. In Chapter 4, the anterior corneal shape was determined as a function of refractive error. Consequently, the shape of the emmetropic anterior corneal surface is different between the symmetrical model and the measurements in Chapter 4. If all of the remaining biometric parameters are kept constant when creating the asymmetric models, the axial length and spherical aberration (Z_4^0) prediction will differ between the emmetropic symmetrical and asymmetrical models. To maintain the good spherical aberration prediction achieved with the symmetrical model and to facilitate a comparison between the symmetrical and asymmetrical models, the shape of the posterior corneal surface and depth of the aqueous chamber were adjusted, within anatomical limits, until the emmetropic asymmetrical models' spherical aberration prediction and axial length were similar to the values of the emmetropic symmetrical model.

The aberrations of the SC and BC models were calculated for a 5 mm pupil and fit with a series of Zernike polynomials. Comparisons were made between the aberrations of the asymmetrical models, the symmetrical models and the young subjects, from Chapter 3, with metrics that represent spherical aberration, coma and all high-order aberrations. Spherical aberration (SA) was represented by the coefficient of the symmetrical 4th order term (Z_4^0). Coma was calculated as the RMS (RMS_C) of the two 3rd order coma terms (Z_3^{-1} & Z_3^1). The size of the high-order aberrations (HOA) was represented as the RMS (RMS_{HO}) of all the terms greater than the 2nd order. These three metrics describe most of the observed aberrations since coma and SA were the dominant 3rd and 4th order aberrations respectively.

The Zernike coefficients that define the wavefront aberrations of individual subjects can take on both positive and negative values (Porter, et al., 2001). RMS calculations (equation 2.6) involve squaring the Zernike defined wavefront aberrations before taking a square root. Consequently, Zernike defined wavefront aberrations with the same magnitude but opposite sign would have the same RMS. An empirical RMS value determined by averaging the RMS of individual subjects could be significantly larger than a value that was determined by averaging the individual Zernike coefficients and then calculating the RMS.

The models developed here were intended to predict average empirical aberrations. To provide a complete comparison between model predictions and empirical results, average aberration values were calculated with two methods. The first method involves calculating the RMS for each individual subject and then averaging across subjects ($RMS_{C\bar{S}}$ & $RMS_{HO\bar{S}}$). In the second method the averages of the individual Zernike terms are calculated first and then used to calculate RMS values. ($RMS_{C\bar{T}}$ & $RMS_{HO\bar{T}}$).

5.3 Results

When the misalignment parameters were added to the emmetropic symmetrical model the resulting wavefront aberrations were first fit with a series of Zernike polynomials that were inclusive up to the 6^{th} order terms. The coefficients of the 5^{th} and 6^{th} order terms were observed to be equal to or less than 10% of the value of the 3^{rd} and 4^{th} order terms. Consequently a 4^{th} order series of Zernike polynomials was used to describe the wavefront aberrations of the asymmetrical models described in this chapter.

The effect of sequentially misaligning ocular components for an emmetropic model was observed by comparing the predicted aberrations after each misalignment was added. The spherical aberration of the models remained relatively constant as it increased by 5.4% after angle α was added to the model, stayed constant when the pupil was decentered and then reduced to an increase of 2.7% from the symmetrical model's value when the lens model was tilted and decentered.

The addition of an angle α induced a significant amount of coma in the emmetropic model. Decentering the pupil decreased the induced coma by 42%. The misalignment of the crystalline lens increased the induced coma by 8% from the model with only an angle alpha and pupil decentration.

Adding angle α increased the high-order RMS above the symmetrical model prediction by a factor of 1.4. Decentering the pupil reduced the increase in RMS_{HO} by a factor of 0.61. Tilting and decentering the crystalline lens changed the overall increase in the RMS_{HO} from the symmetrical model to a factor of 0.68.

In Figure 5.2, the model's RMS_C and RMS_{HO} predictions were compared to the two types of average RMS_C and RMS_{HO} values for 4 emmetropes from the young subjects in Chapter 3. In each model the predicted RMS_C was significantly less than the $RMS_{C\bar{S}}$ value observed in the emmetropic subjects. The asymmetrical model with the three component misalignments predicted a $RMS_{C\bar{T}}$ value of 0.041 μm, which compares well to the empirical value calculated after averaging aberrations across subjects of 0.055 ± 0.159 μm.

The empirical emmetropic average RMS_{HO} values were both observed to be significantly larger than the model predictions. When the average was taken across subjects ($RMS_{HO\bar{S}}$) the value was 6 times larger than the emmetropic asymmetrical model prediction. The value of the high-order RMS averaged across the Zernike terms ($RMS_{HO\bar{T}}$) was 4 times larger than the emmetropic asymmetrical model prediction.

Since the emmetropic shape of the anterior corneal surface in the asymmetrical models was different than the symmetrical model, the shape of the posterior surface and depth of the aqueous was changed to create emmetropic asymmetrical models that had an axial length and Z_4^0 term similar to the emmetropic symmetric model. A trial and error process revealed that these requirements could be met if the central radius of curvature of the posterior corneal surface was changed from 6.3 to 6.5 mm and its asphericity was changed from -0.3 to -0.5. The depth of the aqueous was also reduced from 3.4 to 3.3 mm.

Table 5.3 displays the aberrations and axial length (AL) of the SC models as a function of refractive error when the object was positioned at both infinity and the model's far point. The high-order aberrations from the BC models were nearly identical to the corresponding SC models, as the coefficients of individual Zernike terms from corresponding models never differed by more than 0.006 μm.

The results in Table 5.3 show that moving the object to the far point caused an increase in the predicted SA that ranged from 10 to 35%. Changing the object position had virtually no effect on the predicted coma. The change in the predicted SA caused the high-order RMS to increase by 10 to 20%.

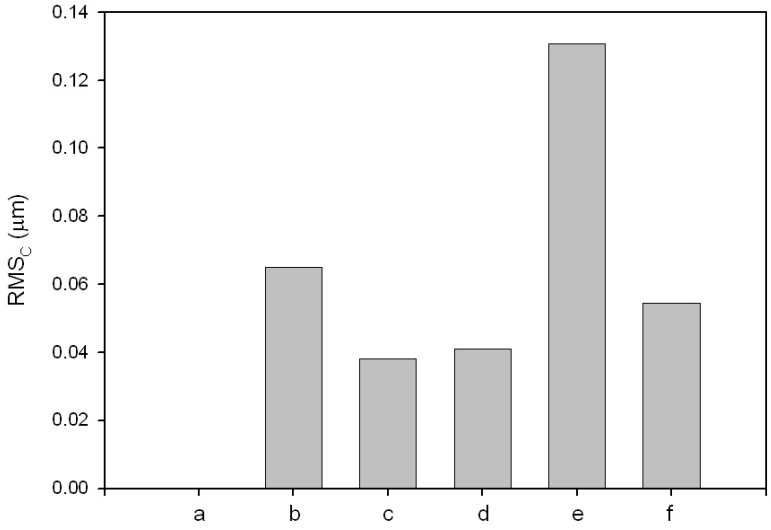

a: symmetrical model from Chapter 3

b: asymmetrical model with angle α

c: asymmetrical model with angle α + pupil decentration

d: asymmetrical model with angle α + pupil decentration + lens tilt & decentration

e: empirical average across subjects

f: empirical average across Zernike terms

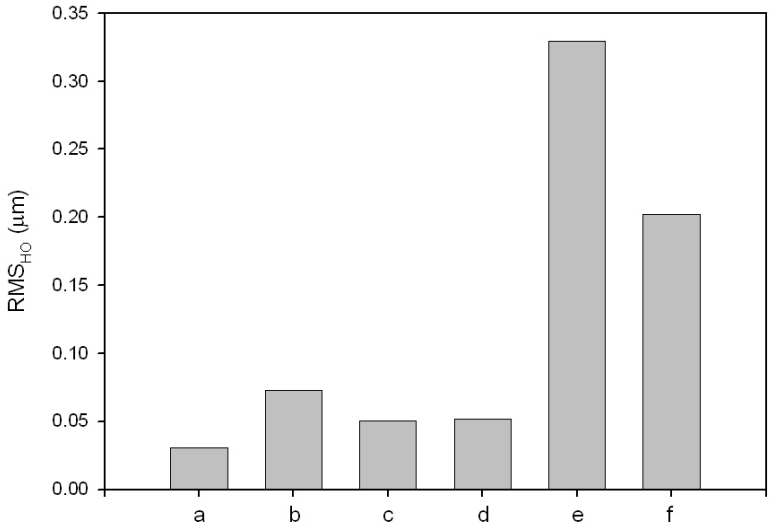

Figure 5.2: Comparison of Coma and High Order RMS Between Models Built by Sequentially Adding Misalignment Parameters and Average Empirical Values from Emmetropic Subjects.

Table 5.3: Results from the SC models when the object is placed at both infinity and the far point. AL refers to the axial length.

SE (D)	AL (mm)	Z_4^0 (μm)		RMS_C (μm)		RMS_{HO} (μm)	
		infinity	far point	infinity	far point	infinity	far point
0	24.07	0.030		0.038		0.048	
-1	24.35	0.036	0.040	0.036	0.039	0.051	0.056
-2	24.63	0.043	0.051	0.039	0.043	0.059	0.067
-3	24.93	0.050	0.062	0.047	0.051	0.069	0.081
-4	25.23	0.058	0.074	0.057	0.061	0.081	0.096
-5	25.54	0.065	0.085	0.069	0.072	0.095	0.112
-6	25.87	0.073	0.097	0.082	0.085	0.110	0.129
-7	26.20	0.081	0.109	0.096	0.097	0.126	0.146
-8	26.55	0.090	0.121	0.111	0.111	0.143	0.164

The shape of the anterior corneal surface and axial length were the components simultaneously altered to create the refractive error of the asymmetrical models. To determine each components' contribution to the models' aberrations two additional models were created that contained only the refractive or axial components. The refractive only model had the cornea of the -8 D model and emmetropic axial length, giving a refractive error of -2 D. The axial only model contained the emmetropic cornea and the axial length of the -8 D model, giving a refractive error of -6 D. A comparison of the aberrations between the refractive, axial, emmetropic and -8 D models is shown in Table 5.4.

The refractive and axial models revealed that changing the corneal shape contributed to approximately 25% of the refractive error in the -8 D model while increasing the axial length accounted for 75%. The SA of the -8 D model increased by 200% from the emmetropic value. In comparison, the refractive model predicted an increase of 243% while the axial model predicted a decrease of 43%. The increase in RMS_C was totally due to the change in anterior corneal shape. Similar to the SA, the increase in RMS_{HO} was due to changing the anterior corneal shape but increasing the axial length reduced the amount of change. These results are similar to the symmetrical models in Chapter 3, where adding 8 D of refractive myopia caused an increase in the SA of 183%. The asymmetrical models differ from the symmetrical models because adding 8 D of axial myopia to the symmetrical models caused the SA to increase by 52%.

Figures 5.3, 5.4 and 5.5 show comparisons between Z_4^0, RMS_C and RMS_{HO} of the young adult subjects and the models. In these graphs ASC represents the asymmetrical models with symmetrical corneas (SC) when the object was positioned at infinity. AFP is the data from the asymmetrical SC models when the object was positioned at the far point. SR and SA symbolize the symmetrical models with refractive and axial defocus from Chapter 3. The results from the ASC and the asymmetrical models with biconic corneas were so similar that their predicted aberration values would overlap in the graphs and consequently have not been shown.

Table 5.4: Contribution to Predicted Aberrations from the Components used to Simulate Refractive Error. SE is spherical equivalent. SA is spherical aberration.

Model	SE (D)	SA (μm)	RMS_C (μm)	RMS_{HO}(μm)
emmetropic	0.00	0.030	0.038	0.048
-8 D	-8.00	0.090	0.111	0.143
refractive	-2.03	0.103	0.112	0.152
axial	-6.04	0.017	0.038	0.041

The emmetropic asymmetrical model was designed so that its prediction of spherical aberration was similar to the prediction of the emmetropic symmetrical model. Similar to the axial and refractive symmetrical models the predicted SA of the asymmetrical models increased as a function of refractive error. The predicted SA increased by rates of the 0.002, 0.013, 0.008 μm/D of myopia for the axial symmetrical, refractive symmetrical and asymmetrical models. Predicted SA increased at a rate of 0.012 μm/D when the object was moved to the far point. Mann-Whitney Rank Sum Tests revealed there is not a statistically significant difference between the mean SA of the young adult subjects and asymmetrical models with the object at either infinity or the far point (p-values of 0.13 and 0.35 respectively). The difference in the rate of change (slope) in the SA with myopia between the empirical data and the SC models was not statistically significant (ASC: $p=0.41$, AFP: $p=0.26$). A statistically significant difference was observed in the change in SA with myopia between the ASC and AFP models ($p<0.001$).

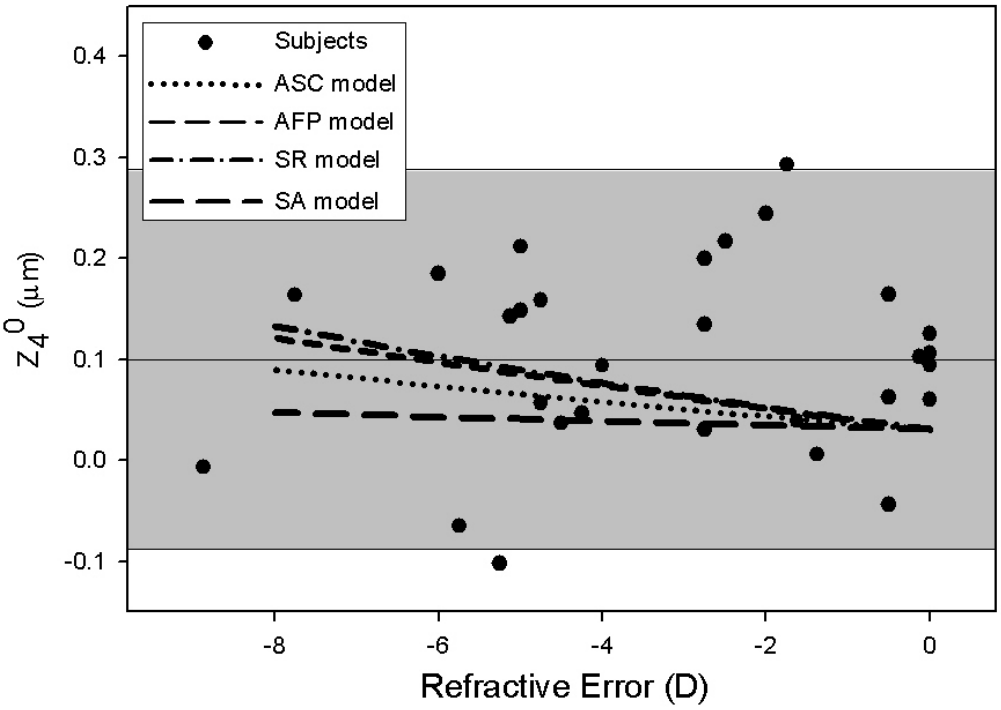

Figure 5.3: Spherical Aberration of the subjects, asymmetrical and symmetrical models. The shaded area highlights the empirical data that are within 2 standard deviations of their mean.

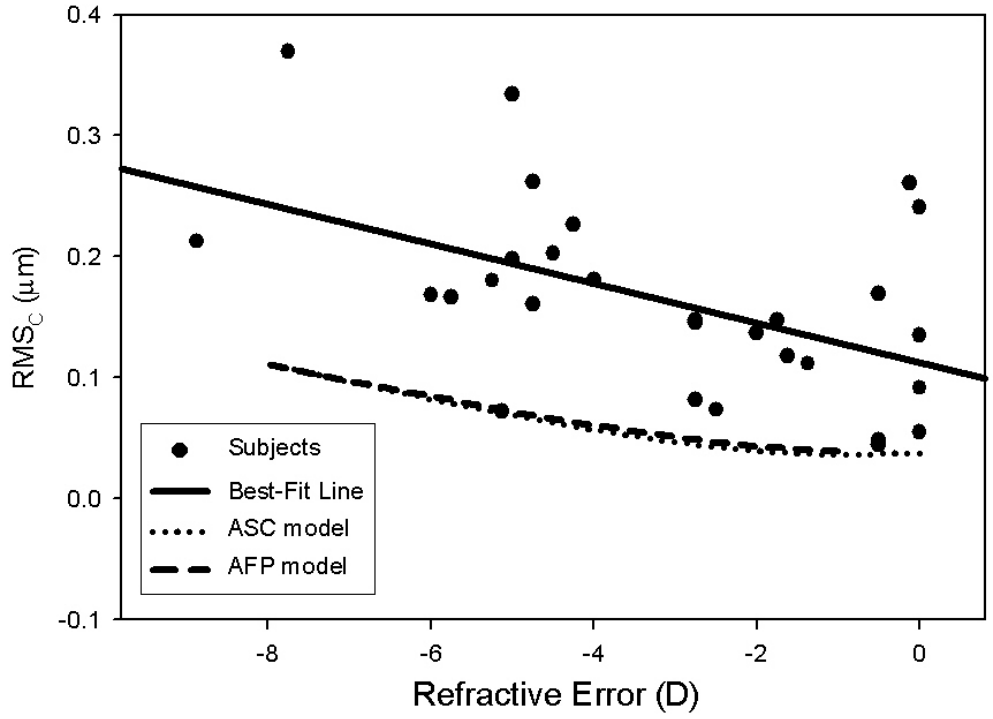

Figure 5.4: Coma RMS of the subjects and asymmetrical models

Both the coma (p=0.005) and high-order (p=0.015) RMS, from the young adult subjects, show a statistically significant correlation to their spherical equivalent (Figures 5.4 and 5.5). The coma and high-order RMS of both the ASC and AFP data also increase linearly with myopia. The actual data of the models is almost identical so statistical analysis was only performed on the ASC model data. Linear regression of the SC model data with the object at infinity revealed the predicted coma and the high-order RMS also have a statistically significant correlation to their spherical equivalent (p<0.001). A comparison of the linear regression results is shown in Table 5.5. T-tests revealed the intercepts of the empirical and model data for both the coma (p=0.029) and high-order RMS (p<0.001) were statistically significantly different. Similar tests show that the slopes of the empirical and model data from both the coma (p=0.513) and high-order (p=0.177) RMS are not statistically significantly different. When the object was positioned at the far point of the model the RMS_{HO} increased at a rate of 0.015 μm/D of myopia, which was also not statistically significantly different from the corresponding increase observed in the young adults (p=0.693). The slope of the empirical data will be reduced somewhat when spectacle magnification (Campbell, et al., 2003).

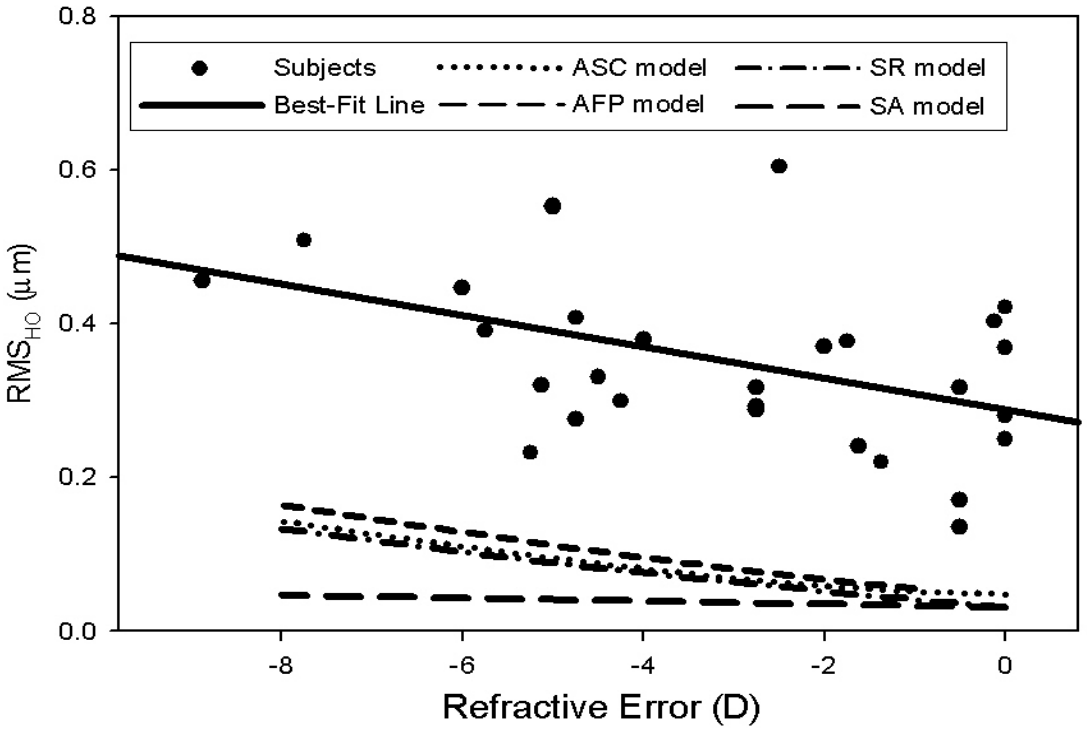

Figure 5.5: High-order RMS of the subjects and models

Table 5.5: Comparison of the Linear Regression Results Between Subject Data and SC models when the object was at infinity (ASC).

		Slope		Intercept	
		Coefficient	Std. Error	Coefficient	Std. Error
RMS_C	Subjects	-0.016	0.005	0.113	0.021
	SC Models	-0.010	0.001	0.025	0.005
RMS_{HO}	Subjects	-0.021	0.008	0.288	0.031
	SC Models	-0.019	0.001	0.060	0.006

To compare the results of determining average Zernike terms across subjects prior to calculating RMS values, the results were separated into three refractive error categories. This grouping was used because the empirical RMS_C and RMS_{HO} were found to correlate with refractive error. Table 5.6 displays how the groups were defined along with empirical and model data from the three groups. A graphical representation of the groups aberrations are shown in Figure 5.6

Table 5.6: Empirical and ASC Model Data for the Three Refractive Error Groups

Group		Emmetropic	Low Myopia	Moderate Myopia
Range (D)		0.0 ≥ SE > -1.0	-1.0 ≥ SE ≥ -4.5	-4.50 > SE > -9
Number	Subjects	8	11	10
	Models	1	4	4
SE (D)	Subjects	-0.20 ± 0.25	-2.75 ± 1.08	-5.83 ± 1.40
	Models	0.00 ± ------	-2.50 ± 1.29	-6.50 ± 1.29
SA (μm)	Subjects	0.084 ± 0.062	0.122 ± 0.101	0.089 ± 0.111
	Models	0.030 ± -------	0.047 ± 0.009	0.077 ± 0.010
$RMS_{C\bar{T}}$ (μm)	Subjects	0.013 ± 0.164	0.081 ± 0.132	0.076 ± 0.227
	Models	0.038 ± --------	0.043 ± 0.018	0.089 ± 0.020
$RMS_{HO\bar{T}}$ (μm)	Subjects	0.102 ± 0.132	0.188 ± 0.312	0.155 ± 0.420
	Models	0.048 ± --------	0.064 ± 0.020	0.118 ± 0.023

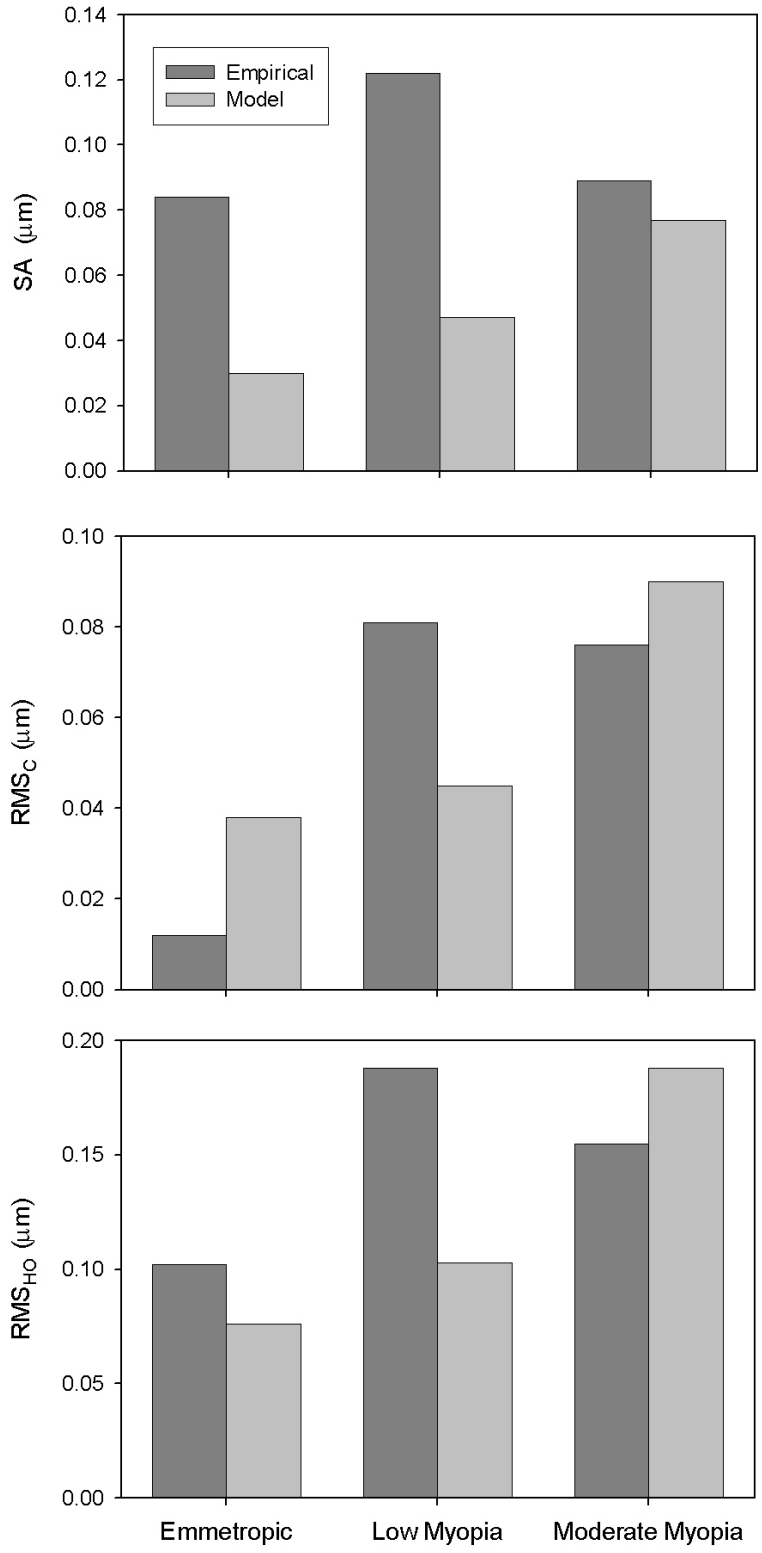

Figure 5.6: Comparison of Empirical and Model Aberrations Calculated by Averaging the Coefficients of Individual Zernike Terms

One-Way analysis of variance (ANOVA) was used to determine if there was a statistically significant difference between the empirical and model aberrations, calculated from average Zernike terms, of the refractive error groups. The results from the ANOVA tests are shown in Table 5.7. For each of the empirical metrics it was observed that there was not a statistically significant difference between the values for each group. The model metrics were all found to increase significantly with myopia. Statistically significant differences were not found between the empirical and model metrics for each level of myopia. While no statistical tests could be performed on the emmetropic model metrics since they consist of only a single value, these values were found to be within the standard deviation of the average empirical values (Table 5.7).

Table 5.7: One-Way ANOVA Results. The shaded cells highlight the tests that found statistically significant differences.

Groups	Metric	p-value	Power
All	SA	0.63	---
Empirical	$RMS_{C\bar{T}}$	0.68	---
	$RMS_{HO\bar{T}}$	0.87	---
Models	SA	0.01	0.95
Moderate &	$RMS_{C\bar{T}}$	0.01	0.80
Low Myopia	$RMS_{HO\bar{T}}$	0.01	0.83
Models &	SA	0.17	---
Empirical	$RMS_{C\bar{T}}$	0.58	---
Low Myopia	$RMS_{HO\bar{T}}$	0.45	---
Models &	SA	0.84	---
Empirical	$RMS_{C\bar{T}}$	0.91	---
Moderate Myopia	$RMS_{HO\bar{T}}$	0.87	---

5.4 Discussion and Conclusions

The addition of an average angle α to the symmetrical model instigated the prediction of asymmetrical aberrations. Decentering the model's pupil, by an average amount, reduced the predicted asymmetrical aberrations. These were the expected results, predicted by Bing and Campbell (1994).

The emmetropic axial length of the asymmetrical model was set to 24.1 mm by utilizing a posterior corneal radius of curvature (R_{PC}) of 6.5 mm and aqueous depth (AD) of 3.3 mm. The axial length of this model matched the average young adult value of 24.1 mm found by Grosvenor (1987). Average empirical values for R_{PC} have been found to range between 5.8 and 6.5 mm (Lowe and Clark, 1973; Royston, et al., 1990; Rivett and Ho, 1991; Dunne, et al., 1992; Patel, et al., 1993; Lam and Douthwaite, 1997; Liu, et al., 1999; Seitz, et al., 2001; Dubbelman, et al., 2002). An average young adult empirical AD value of 3.2 ± 0.3 mm (Fontana and Brubaker, 1980) has been observed. The values for R_{PC} and AD that were used in the asymmetrical model are within these anatomical limits. Average young adult empirical AD values of 3.5 mm (Grosvenor, 1987), 3.35 ± 0.15 mm (Kortez, et al., 1989) and 3.10 ± 0.37 mm (Dubbelman, et al., 2001) have also been observed.

To match the SA predicted by the emmetropic symmetrical model the asphericity of the posterior corneal surface (Q_{PC}) was set to -0.5. Average empirical Q_{PC} values of -1.5 (Dunne, et al., 1992), -0.44 (Patel, et al., 1993), -0.66 (Lam and Douthwaite, 1997) have been determined from measurements of the anterior corneal surface shape and corneal thickness. My Q_{PC} value is no longer anatomically accurate with respect to the average, empirical, young adult value of -0.28 ± 0.15 found by Dubbelman, et al. (2002) with a digital slit lamp technique.

A series of myopic, asymmetrical models were created by utilizing average, empirical values for the anterior corneal shape and adjusting the axial length. The paraxial power of the anterior cornea and axial length of the -8 D SC model were 49.7 D and 26.6 mm respectively. These values compare well to the values of 50.3 D and 26.2 mm that were determined from regression analysis of empirical data (Carney, et al., 1997). This shows that simulating myopia by this method produces

myopic models that are more anatomically accurate than models where myopia was simulated by either a purely axial (27.5 mm) or refractive technique (56.6 D).

The aberrations predicted by the asymmetric models with biconic anterior corneas were identical to the corresponding models with symmetrical corneas. This result could be due to the fact that the model's biconic anterior corneal shape was designed to contain the average amount of asymmetry as subjects with 1 D of cylinder refractive error. This amount of cylinder refractive error was chosen since the model's predictions were to be compared to empirical data with low amounts of cylinder (≤1.25 D). To test this hypothesis, the sag of the model's conic and biconic anterior corneal surfaces was calculated at a radial distance of 2.5 mm from their apex with equations 2.10 (conic) and 4.4 (biconic) and the data from Table 5.2. Biconic sag was calculated at both principal meridians. For each corresponding set of models it was found that the sag of the biconic surface at the principal meridians only differed from the conic surface by ±7 μm. This indicates that adding a biconic cornea with a small amount of asymmetry does not change the corneal surface enough from a conic to change the model's predicted aberrations. Future models with larger amounts of corneal astigmatism will have to be made to see their effect on the predicted aberrations.

The SA, coma and high-order RMS of the asymmetrical models increased as a function of refractive error. Increase in SA was slow and may be below measurement sensitivity. While the refractive error in the asymmetrical models was found to be primarily due to their increased axial length, the increase in the higher order aberrations was caused primarily by the change in anterior corneal shape. The empirical RMS_C and RMS_{HO} of the individual subjects were observed to increase as a function of refractive error. While the asymmetrical models underestimated the magnitude of the RMS_C and RMS_{HO} of the individual subjects, the predicted rates of increased aberrations matched the empirical observations. Since it was found that increasing the axial length did not change the model's prediction of coma and caused the SA to decrease with refractive error, the model's anterior corneal shape must change to predict the empirical results. Contrary to the postulate of Cheng, et al. (2003) from a reduced eye model, axial length changes cause little change in high order aberrations. Refractive changes drive the observed change in high order aberrations. This further emphasizes that myopia must be modeled by combining changes in axial length and anterior corneal shape.

Similar to Chapter 3, the aberrations of the asymmetrical models with symmetrical corneas were also calculated when the object was positioned at the models' far point. Unlike the results

from the symmetrical models in Chapter 3, moving the object to the model's far point caused their SA and consequently RMS_{HO} to significantly increase. For the -8 D model the SA increased by 34% and the RMS_{HO} increased by 15%. This result is consistent with the current theory that states that wavefront aberrations will usually be different for rays with different object points with the same position in the exit pupil (Smith and Atchison, 1997). While the increase in aberrations caused by moving the object to the models' far point did not affect the models' ability to predict the empirical SA, it did not account for the difference between the RMS_{HO} of the models and the individual subjects.

Cheng, et al. (2003) have used a single surface (reduced) eye model to investigate how SA changed with axial myopia. For their calculations the object was only placed at their model's far point. Over a range from emmetropia to -10 D their model's SA significantly increased from approximately 0.1 μm to 0.3 μm. Their large change in SA is not consistent with empirical measurements and the models introduced here (0.03 μm to 0.12 μm). This discrepancy also emphasizes the importance of including an appropriate GRIN crystalline lens in an eye model that accurately predicts empirical aberrations.

An empirical RMS value determined by averaging the RMS of individual subjects could be significantly larger than a value that was determined by averaging the individual Zernike coefficients and then calculating the RMS since the Zernike coefficients that define the wavefront aberrations of individual subjects can take on both positive and negative values (Figure 5.7). This was the case observed in this chapter.

When the model predictions were compared to the empirical measurements, the models were found to provide a good prediction of empirical SA. The average individual RMS_C and RMS_{HO} of the young adult subjects ($RMS_{C\bar{S}}$ and $RMS_{HO\bar{S}}$) were seen to be significantly larger than the corresponding model predictions. But the models provided good predictions if the average RMS_C and RMS_{HO} were calculated by first averaging the appropriate Zernike terms ($RMS_{C\bar{T}}$ and $RMS_{HO\bar{T}}$). This shows that asymmetrical models built with average misalignment parameters can predict empirical aberrations derived by averaging individual Zernike terms but underestimate the amount of asymmetrical aberrations that are observed in individual subjects.

This raises the question of what an average eye model can be expected to predict. When wavefront aberrations are averaged over many eyes, asymmetrical Zernike terms tend to be averaged out since they can take on both positive and negative values (Charman and Walsh, 1985; Porter, et al., 2001; Castejon-Mochon, et al., 2002). Modelling parameters like lens tilt and decentration that account for the prediction of asymmetrical aberrations also take on both positive and negative values (Cui, 1998). If the sign of the modelling parameters is taken into account when creating an average eye model then the sign of the aberrations that the model should predict, needs to be considered when average metrics are calculated.

It was previously described how a RMS calculation is not sensitive to the sign of the Zernike terms that define the wavefront aberrations. Zernike defined wavefront aberrations with the same magnitude but opposite signs would have the same RMS. If the sign of modelling parameters are considered when creating an average eye model then Zernike coefficients, that define the wavefront aberrations the model should predict, need to be averaged before RMS calculations are performed.

An average eye model created by averaging modelling parameters, including their sign, would be expected to predict RMS aberrations that are calculated after averaging the Zernike coefficients (sign included) and would not predict average RMS values that are averaged after the RMS is calculated (sign excluded). This was the case in this chapter.

It has been observed that angle α and pupil decentration do not individually correlate with RMS aberration (Cui, 1998; Marcos, et al., 2001b). The models developed here incorporate the interaction between angle α, pupil decentration and lens decentration and tilt. Utilizing average misalignment parameters created an average asymmetrical model that predicted empirical aberrations that were calculated by averaging Zernike terms thus averaging out variations about a minimum value. This indicates that some of the aberration in the human eye is due to random misalignments about a minimum level.

To create these models a few assumptions were made that could have affected their aberration predictions. The shape of the posterior cornea and crystalline lens remained constant in all models but may change with myopia. Misalignments of the ocular components were measured for a group of emmetropes. The average values of misalignment parameters may also change with myopia.

Figure 5.7 compares the Zernike coefficients that define the high-order aberrations in 2 subjects, with refractive errors of -4 D and -4.25 D, and the -4 D ASC model. This graph shows the diversity and variety in the high-order aberrations of individual subjects. The asymmetrical models, developed in this chapter, only predict significant coefficient values for the Zernike terms used to define coma and spherical aberration (Z_3^{-1}, Z_3^1 & Z_4^0). If more complex descriptions, like Zernike polynomials, are used to define anterior corneal shape, its possible that models could be built that predict other high-order aberrations. But, when aberrations are averaged, high-order terms are generally averaged out to a relatively insignificant amount (Charman and Walsh, 1985; Porter, et al., 2001; Castejon-Mochon, et al., 2002). Similarly high-order Zernike terms defining corneal shape could be averaged out and any advantage they may provide would be lost. It remains to be seen whether this will be the case.

Average eye models can only be expected to predict average aberrations. Average asymmetrical aberrations are significantly smaller than those observed in individual subjects. An average eye model cannot be expected to predict individual aberrations. It will probably take individualized models to accomplish this. Considering these expectations the eye models presented here provide an accurate means of predicting average aberrations.

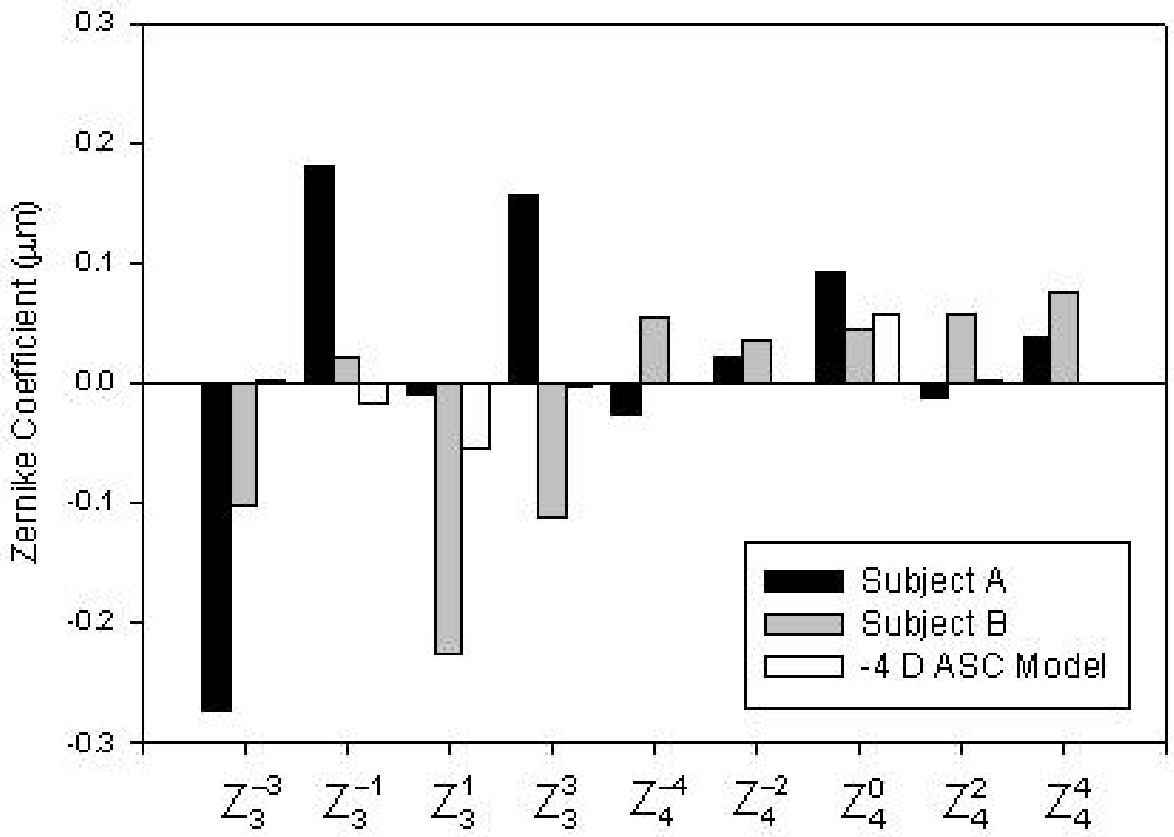

Figure 5.7: Comparison between high-order Zernike coefficients between two subjects and a corresponding asymmetrical model. Subjects A and B had refractive errors of -4 D and -4.25 D respectively

6 Modeling Laser Refractive Surgery

6.1 Background and Introduction

The goal of refractive surgery is to eliminate a patient's dependence on spectacles or contact lenses. In terms of aberrations, this means primarily removing defocus but eliminating astigmatism is also a goal. Recently control of high-order ocular aberrations has become a secondary goal (MacRae, 2000). Correcting refractive error requires changing the focusing power of the ocular optics. This is achieved by reshaping a central zone on the anterior surface of the cornea. For a myopic subject, flattening the cornea reduces the eye's power. Conversely, hyperopic subjects are corrected by steepening the cornea.

Throughout its history, numerous refractive surgical techniques have been developed. Initially, in a procedure named refractive keratotomy, incisions were distributed radially around the corneal surface to induce a mechanical flattening (Thorton, 1999). Lamellar techniques were then introduced where corneal shape is altered by removing tissue with a blade (Swinger, 1999). When lasers were introduced to ophthalmology it was discovered that ultraviolet wavelengths could be used to reshape the corneal surface by ablating tissue. This discovery has had the greatest impact on the development of refractive surgery and has led to the techniques that are predominately used today.

The eye has developed to allow radiation from a portion of the optical spectrum to penetrate its tissue. Consequently, light energy could be a useful tool in ocular surgery once the ability to control its delivery and intensity has been established. This criterion was met when lasers became available. Initially laser energy was used to photocoagulate the retina to treat pathological conditions (O'Brart and Marshall, 1999). As laser technology developed, it was implemented in new techniques to improve existing ophthalmic surgical procedures including refractive surgery.

Normally, a healthy transparent cornea transmits optical radiation from 400 to 1400 nm with little absorption. Theoretically lasers with emission in the far ultraviolet (UV) or far infrared (IR) could be used for operating on the corneal surface. At present it is pulsed UV excimer lasers that appear to have the most potential and are used commercially.

Excimer lasers are named after the physical state of their lasing medium, which consists of two atoms of an inert gas bound in a highly excited state with halogen atoms (excited dimers). Decay of these molecules produces the emission of very energetic UV photons. Generally, clinical ophthalmic excimer lasers use an argon-flouride (ArF) gas mixture, which has an emission wavelength of 193 nm. Excimer lasers are typically pulsed, with duration of 10 nsec, a frequency between 1 and 100 Hz and energies of 20 to 200 mJ (O'Brart and Marshall, 1999).

Theories, based on thermal vibration and molecular decomposition, have been proposed to explain the effect caused by excimer laser photons absorbed by corneal tissue (Garrison and Srinivasan, 1985). In the thermal theory, super-heated molecules break apart due to vibration. Photon induced molecular decomposition (ablation) suggests that molecules are ejected from the tissue surface when their intermolecular bonds are broken by the absorption of photons. Individual photons, at 193 nm, would be capable of ablation since they have energy in excess of 6 eV, which is greater than the binding energy of some proteins (O'Brart and Marshall, 1999).

At any biological interface, excimer UV photons are virtually all absorbed within the first few microns of the surface. Consequently, each 193 nm pulse can remove from 0.25 to 1 micron of tissue by varying the pulse energy (O'Brart and Marshall, 1999)

Typically, clinical lasers are focused to achieve the energy concentration (power) required for tissue damage. Since individual excimer photons have enough energy to ablate tissue these lasers do not need to be focused. Consequently, relatively large corneal areas can be treated simultaneously with wide excimer laser beams (O'Brart and Marshall, 1999).

By precisely controlling the laser energy (number of pulses) delivered to specific locations within the ablation zone the cornea can be reshaped to achieve a desired change in refraction. A myopic correction requires a flattened surface, so the energy concentration delivered and amount of tissue removed within the ablation zone will be highest centrally and gradually decline towards the periphery. A hyperopic correction requires a steepened surface that is achieved by removing more tissue peripherally than centrally within the ablation zone (O'Brart and Marshall, 1999). Algorithms have been developed that describe the ablation depths and profiles necessary to correct both myopic and hyperopic refractive errors (Munnerlyn, et al., 1988).

Several techniques that depend on the beam diameter of the laser have been developed commercially to control the number of laser pulses (energy) delivered to a given location within the ablation zone. When a broad beam (5-7 mm diameter) is used, control is achieved with either an ablatable mask or by progressively opening or closing an iris diaphragm. Pulse density is achieved with a smaller beam by scanning it over the ablation zone.

Since the cornea is composed mostly of stromal cells while epithelial cells undergo continuous cell turnover throughout adult life, a permanent change in corneal shape can only be attained with laser ablation by removing stroma. There are two techniques commonly used to expose the stroma for treatment.

In photorefractive keratectomy (PRK) the epithelial cells are completely removed, within the central 6.5 to 9.5 mm, by either mechanical, chemical or laser means. Visual improvements are usually seen after re-epithelization, which will occur in 2 to 4 days after a myopic treatment while patients heal in 3 to 9 days after hyperopic PRK. Refractive stability is achieved in 3 to 6 months after myopic PRK and 6 to 9 months for hyperopic PRK (Jackson, 2001).

Laser in situ keratomileusis (LASIK) involves creating a flap in the cornea by making a lateral incision with a device called a keratome or a laser. The flap, which is thick enough to include the epithelium, is then lifted exposing the stroma underneath. After the ablation, the flap is replaced and patients usually achieve good uncorrected visual acuity within a day or two. Recently, PRK has been largely abandoned for LASIK due to its many apparent advantages such as minimal discomfort, rapid corneal healing and stabilization of refraction (Jackson, 2001).

Although it is difficult to compare data from one commercial laser system to another, several studies have shown that generally over 90% of low to moderate myopic patients ($\geq$ -10 D) are found to be within 1 D of emmetropia after PRK (Hersh, et al., 1998; Zadok, et al., 1998; Amoils, 1999; Hadden, et al., 1999; McDonald, et al., 1999; Pallikaris, et al., 1999; Kapadia and Wilson, 2000; Pop and Payette, 2000; Jackson, 2001). A number of prospective trials have shown that the efficacy of removing refractive error with LASIK is very similar to that of PRK and that LASIK is not superior to PRK except in the first few post postoperative weeks (Hersh, et al., 1998; El Danasoury, et al., 1999; Pop and Payette, 2000).

A survey of 690 PRK patients revealed that 92% of patients were satisfied with the results, even though 55% experienced significant daytime glare and 32% reported a decrease in night vision (Brunnette, et al., 2000). A comparison of pre and one year post-PRK visual acuities has shown that most high-contrast visual acuities worsened after PRK even though they were still within a normal range. Most subjects lost low-contrast visual acuities after PRK and many of the post-op values were below the normal range (Verdon, et al., 1996). Low-contrast visual acuity losses were also found to exceed high-contrast losses in a similar prospective PRK study (Casson, et al., 1995).

The observed post refractive surgical loss in visual acuity has led many researchers to investigate if there exists unexpected surgically induced changes in corneal shape and aberrations that could account for the loss of vision.

To investigate how laser refractive surgery altered the asphericity of the anterior corneal surface, Hersh, et al. (1996) compared pre and postoperative corneal topographies from 132 patients. These subjects underwent PRK for myopia with a broad beam excimer laser system (Summit Technology Inc.) with either a 4.5 mm or 5.0 mm beam diameter and attempted corrections ranging from 1.50 to 6.00 D. Topography measurements were made with a videokeratoscope (EyeSys Laboratories) preoperatively and 1 year postoperatively. These measurements were used to estimate the power differences between the patient's cornea and an idealized aspheric model ($Q = -0.26$) at each ring location in the reflected image along 360 semi-meridians. The asphericity along each semi-meridian was determined by fitting an aspheric curve to the power differences over the central 4.5 mm. The reported asphericities were the average of the semi-meridians' values. Following PRK, all corneas exhibited a positive central asphericity and the mean postoperative asphericity was 1.05. A significant association was found between achieved refractive correction and increased postoperative positive asphericity. This indicates that the normally prolate anterior corneal contour became oblate after PRK.

Since laser refractive surgery structurally compromises the cornea by removing tissue and previously described unexpected changes have been observed in the shape of the anterior corneal surface, investigations were performed to see if the posterior corneal surface changes postoperatively. Kamiya, et al. (2000) described refractive and posterior corneal surface changes in 37 eyes from 21 patients (average age 33 ± 10 years). Their mean preoperative SE was -5.28 ± 1.74 D (range -2.00 to -9.75 D). PRK was performed on these patients with a 20/20 broad beam

excimer laser system (VISX). Measurements of the posterior corneal topography and corneal thickness were obtained on an Orbscan pre and postoperatively. Refractive change in the posterior surface was determined by comparing the pre and postoperative mean powers within the central 2.0 mm. Difference maps were used to determine if any surgically induced changes occurred in the posterior corneal topography. These maps were constructed by comparing the pre and postoperative topographies assuming that a peripheral annular zone (7-10 mm from the corneal apex) was unaffected by the surgical procedure. Change in the elevation of the posterior corneal surface was assessed at the centre of the difference map generated from pre and post-op topographies. Three months after PRK, the mean SE was found to be -0.41 ± 0.34 D. The mean central corneal thickness had reduced to 430.1 ± 62.8 μm from 544.4 ± 35.2 μm. The power of the posterior cornea was found to significantly decrease by 0.41 ± 0.34 D. The position of the posterior corneal apex was found to significantly shift anteriorly by 54.3 ± 4.0 μm. There was a correlation between the refractive change and the forward shift of the posterior corneal surface. The residual corneal thickness individually correlated with both the amount of posterior corneal refractive change and the degree of forward shift.

Naroo and Charman (2000) also examined changes in the anterior and posterior corneal surfaces, anterior corneal power and central corneal thickness after PRK. This study included 16 eyes from 16 subjects with a mean age of 30 ± 9 years (range of 20 to 47 years). PRK was performed with an EC-5000 scanning beam excimer laser system (Nidek). The ablated optical zone diameter was 6.5 mm, with a blended transition zone out to 7.5 mm. The mean attempted correction SE was -3.66 D (range of -1.73 to -6.43 D). Anterior corneal power changes were measured with an autokeratometer (ARK900S, Nidek). Ultrasound pachymetry (Humphrey) was used to monitor changes in the central corneal thickness. Topographic changes in the curvature of the anterior and posterior corneal surfaces, measured by an Orbscan, were determined by comparing the radii of curvature of best-fit spheres (BFS) derived for the central 5 mm. At 12 weeks postoperatively, linear regression between the change in anterior corneal power and the intended correction revealed a slope of -0.66, an intercept of 0.85 D and a $p < 0.01$. The changes in central corneal thickness were approximately the magnitude of theoretical calculations from the equations of Munnerlyn, et al. (1988). The radius of curvature of the anterior BFS was found to flatten linearly with attempted correction. The slope, intercept and p-value from linear regression were -0.19 mm/D, 0.11 mm and <0.01 respectively. The curvature of the posterior BFS was found to

steepen after surgery. Linear regression between the posterior BFS radius of curvature and attempted correction produced a slope of 0.19 mm/D, an intercept of -0.36 mm. This correlation was significant at a p=0.05 level.

To assess the changes in posterior corneal power and asphericity after myopic LASIK, Seitz, et al. (2001) examined the corneal topographies of 57 eyes of 29 subjects. LASIK was performed with a Keratom II broad beam excimer laser (Schwind). The SE of the attempted corrections ranged from -1 to -15.50 D with a mean of -5.06 ± 3.84 D. The ablation zone diameters ranged from 5.0 to 8.1 mm. Mean age at the time of surgery was 33 ± 9 years. Corneal topography and thickness were measured on an Orbscan preoperatively and 3 months postoperatively. Posterior power and asphericity were determined by decomposing topographic height data within the central 6 mm into a set of Zernike polynomials by a previously developed technique (Langenbucher, et al., 1999). At 3 months postoperatively, the power of the posterior corneal surface was found to become more negative, changing significantly from -6.28 ± 0.22 D to -6.39 ± 0.23 D (p=0.02). Asphericity was also found to change significantly from -0.02 ± 0.07 to 0.14 ± 0.20 (p<0.0001). The change in posterior corneal power correlated significantly with the change in refractive SE (p=0.004). Preoperatively the asphericity ranged from -0.14 to 0.22 and 50% of the values were less than zero indicating a predominantly prolate surface. At 3 months postoperatively asphericity values were found to range from -0.02 to 1.44. Half of these values were more than 0.14, indicating that the posterior corneal surface was predominately oblate after surgery. They did not attempt to correlate changes in asphericity with attempted correction.

Before ocular aberration measurements became widely available, corneal first surface aberrations, estimated from topographic measurements, were investigated (Oliver, et al., 1997; Martinez, et al., 1998; Oshika, et al., 1998).

Oliver, et al., (1997) reported the pre and one year post-op corneal first surface aberrations of 50 subjects who underwent six dioptres of myopic PRK in one eye. The surgery was performed on an Omnimed excimer laser (Summit Technology) with either a 5 mm or 6 mm single zone or a 6 mm double pass mutlizone broad beam ablations (16, 18 and 16 eyes respectively). The double pass mutlizone ablation consisted of a -5 D correction over 4.6 mm zone and a -1 D correction over a 6 mm zone. The central ablation depth of the mutlizone ablation is equal to the -5 D single zone

treatment but it has a blended edge. Corneal first surface aberrations were estimated from TMS-1 topography measurements and quantified with Zernike polynomials (Hemenger, et al., 1995). The results showed that besides defocus, only spherical aberration and coma were significantly altered by PRK for a 5.5 mm pupil diameter. Spherical aberration and coma were both found to increase in direct proportion to the change in refractive error. On average, the corneal first surface spherical aberration was found to double after 1 year post-PRK for the 6 mm ablation zone while it increased by over 3 times for 5 mm and multizone ablations. The coma was found to double for all three ablation types.

In a similar study, Martinez, et al. (1998) measured the corneal topographies in 112 eyes of 89 patients who had broadbeam myopic excimer PRK (VISX Inc.) performed with an ablation zone diameter of 5 mm. The average age and preoperative spherical equivalent of these subjects was 38.9 ± 0.9 years (19 to 62) and -3.9 ± 0.14 D (-.25 to -8.9). The average attempted correction was 3.7 D (1.5 to 6). Corneal topography was measured with TMS-1 preoperatively (n=112), and at 1 (n=93), 3 (n=103), 6 (n=91), 12 (n=60), 18 (n=53), and 24 months (n=44) postoperatively. Corneal first surface aberrations were determined at pupil diameters of 3 and 7 mm and quantified with Zernike polynomials. This study found that the variance of 3rd order terms for a 3 mm pupil increased slightly at 1 month post-op but returned to preoperative values by 3 months. For a 7 mm pupil 3rd order aberrations increased 4 fold 1 month postoperative, then decreased to 2.9 times by 3 months before stabilizing at 2.7 times the preoperative values at 24 months after surgery. The variance of 4th order terms was found to significantly decrease for a 3 mm pupil following surgery. For a 7 mm pupil 4th order aberrations were found to increase 30 fold 1 month postoperatively, decrease to 19 times the preoperative value at 3 months and then stabilize at 24 times at 24 months. The total high-order aberrations (sum of 3rd and 4th order variances) were found to not change significantly for a 3 mm pupil but they increased 11 fold postoperatively for a 7 mm pupil. 3rd order were dominant before and after surgery for a 3 mm pupil. However, for a 7 mm pupil, while 3rd order aberrations were dominant before surgery, 4th order aberrations became dominant after surgery. The magnitude of the induced increase in aberrations was found to correlate with the attempted correction.

Utilizing the same technique as Martinez, et al. (1998), Oshika, et al. (1999a) compared the corneal first surface aberrations induced in 22 patients, with bilateral myopia, who received broadbeam PRK on one eye and LASIK on the other. The surgeries were performed with an EC-

5000 excimer laser (Nidek Co.). The PRK procedure had an ablation zone diameter of 5.5 mm and a transition zone giving a total ablated diameter of 7 mm while the LASIK ablation zone was 6.5 mm. Corneal topographies were measured with a TMS-1 preoperatively (n=22), 2 weeks (n=19), 6 weeks (n=19), 3 months (n=20), 6 months (n=19), and 12 (n=20) postoperatively. In this study, both PRK and LASIK were found to significantly increase the high-order corneal first surface aberrations at all postoperative points for both 3 and 7 mm pupils. For a 3 mm pupil, there was no statistically significant difference between the post-LASIK and post-PRK eyes at any post-operative point. While there was no postoperative change in the 4th order aberrations, the 3rd order and total high-order aberrations were found to significantly increase by 2.0 and 1.7 times on average. For a 7 mm pupil, the LASIK eyes exhibited increases of 24.3 and 9.0 times in their 4th order and high-order aberrations. These increases were significantly larger than the corresponding increases of 19.6 and 6.6 times that were found for the 4th order and total high-order aberrations for the PRK eyes. There was no difference between the increase in the 3rd order aberrations between the LASIK and PRK eyes, which was found to be 3.6 times. The authors postulated that LASIK induced larger post-op aberrations than PRK in this study because the overall size of the PRK ablation zone (including transition zone) was larger.

In 1998, the first, direct, objective measurements of ocular wavefront aberrations after PRK were reported (Campbell, et al., 1998). This study used Hartmann-Shack measurements to show that optical image quality was worse after PRK when compared to normal non-operated eyes for pupil diameters of 4 mm and larger.

PRK induced changes in ocular optical aberrations were first quantified with Zernike polynomials by Mierdel, et al. (1999). In their study, the optical aberrations of 12 eyes from 12 subjects (aged 21 to 45 years) were measured pre and 1-3 months postoperatively with an instrument based on the Tscherning aberroscope. PRK was performed on a broad beam excimer laser (Multiscan, Schwind) with at least a 6 mm ablation zone. The SE of the correction was 6 D or less. Ocular aberrations were measured with dilated pupils of at least 6 mm. All eyes in this study showed considerable changes after surgery. In particular, the Zernike coefficients corresponding to spherical aberration and coma were found to significantly increase. The sizes of these changes were of the same order of magnitude as in the study by Martinez, et al. (1998).

Seiler, et al. (2000) investigated the correlation between PRK induced changes in ocular aberrations and visual acuity (VA). This study included 15 eyes with an average preop SE of -4.81 ± 1.21 D (-2.25 to -7.0 D) and refractive astigmatism of -0.83 ± 0.8 D (-0.25 to -2.5 D). The laser system and aberration measurement techniques were the same as in the study by Mierdel, et al. (1999). Aberrations were quantified by the RMS of 3rd order, 4th order and total high-order aberrations. Three months after PRK the subject's SE was reduced to +0.41 ± 0.7 D and their refractive astigmatism was -0.21 ± 0.3 D. The 3rd order, 4th order and high-order wavefront errors were observed to significantly increase by factors of 4.7, 4.1 and 4.2 respectively. The correlation coefficients between the increase in high-order wavefront error and best-corrected visual acuity (BCVA), low contrast VA and glare VA were found to be -0.50, -0.89 and -0.52. Significance levels of 0.02, 0.001 and 0.03, respectively show that the increase in high-order wavefront error is significantly correlated with the loss in best-corrected, low contrast and glare VA.

Once the link between laser refractive surgery and aberrations was established, the introduction of new surgical technology led to investigations of their impact on post-op aberrations. This was the case when Moreno-Barriuso, et al. (2001) studied 22 eyes from 12 subjects who had undergone LASIK with a narrow-beam (scanning spot) excimer laser (Chiron Technolas 217-C, Bausch & Lomb Surgical). The ablation zone consisted of a 6 mm optical zone and a transition zone out to 9 mm. An eye tracker assisted the surgery in 20 of the 22 eyes. The average age of these subjects was 28 ± 5 years. Their preoperative refractive error ranged from -2.5 to -13 D and their astigmatism was less than 2.5 D. Aberration measurements were made with a laser ray-tracing technique at a 6.5 mm pupil and quantified with Zernike polynomials. Zernike coefficients were also recalculated for a 3 mm pupil size. In 20 of the 22 eyes the high-order RMS was significantly higher postoperatively for a 6.5 mm pupil. The average 3rd order, 4th order and high-order RMS increased by factors of 2.1, 2.5 and 1.9 for a 6.5 mm pupil. For a 3 mm pupil the same measures increased by factors of 1.8, 1.7 and 1.7. Preoperative refractive error was found to directly correlate with the increment of spherical aberration ($p<0.0001$) while it did not correlate with the increase in coma. No significant increases were found in the 5th and higher order terms after surgery for either the 6.5 or 3 mm pupils.

Marcos, et al. (2001b), have made comparisons of the corneal first surface and total ocular aberrations induced by laser refractive surgery. The laser system and ocular aberration measurement

techniques were the same as in the study by Moreno-Barriuso, et al., (2001). Corneal topography measurements were made with the Atlas Mastervue (Humphrey Instruments-Zeis). This study included 14 eyes from 8 subjects (age range 29 ± 5 years). The average preoperative SE was -6.8 ± 2.9 D (-2.5 to -13 D) and preoperative astigmatism was less than 2.5 D. The reported aberrations were for a 6.5 mm pupil. The postoperative increase in 3^{rd}, 4^{th} and high-order RMS was by factors of 2.0, 2.5 and 1.9 for the ocular aberrations. Corneal first surface aberrations were found to increase by factors of 2.7, 3.9 and 3.7 respectively. When postoperative ocular and corneal aberrations were compared, it was shown that they had a significant linear relationship with a slope of 1.01 ($p<0.0001$). A similar comparison for the spherical aberration shows a significant linear relationship between the ocular and corneal aberrations with a slope of 1.22 ($p<0.0001$). Both postoperative ocular ($p=0.0003$) and corneal ($p<0.0001$) spherical aberration were found to inversely correlate with preoperative spherical equivalent. The authors hypothesized that since larger amounts of spherical aberration were induced in the cornea than in the whole eye that changes in the posterior corneal surface could account for this difference. By using previously described measurements (Seitz, et al., 2001) they calculated an induced change in the posterior corneal surface spherical aberration of -0.103 μm. This value was very similar to the average difference between ocular and anterior corneal spherical aberration that was measured experimentally.

Several other researchers have also modeled refractive surgery in an attempt to explain the unexpected changes observed in corneal shape and aberrations post-surgery. Gatinel, et al. (2001) investigated the effect that myopic ablations, defined by Munnerlyn, et al. (1988), would have on the asphericity of theoretical anterior corneal surfaces. Fifteen preoperative corneal surfaces were defined as conic sections with apical radius of curvature (R_1) values of 7.5, 7.8 and 8.1 mm and asphericity (Q_1) values of -0.6, -0.25, 0, 0.2, and 0.4. Postoperative anterior corneal surfaces were defined by subtracting the theoretically calculated ablation depths across a 6 mm diameter ablation zone for treatments ranging from -1 to -12 D. The apical radius of curvature (R_2) and asphericity (Q_2) of the conic section that best-fits the calculated post-op surface, within the ablation zone, quantified the shapes of the postoperative anterior corneal surfaces. The calculated values for R_2 were found to be independent of the preoperative asphericity values (Q_1). For corneas that were initially prolate, prolateness increased postoperatively ($Q_2 < Q_1 < 0$). Conversely the oblateness of preoperatively oblate corneas was found to increase ($Q_2 > Q_1 > 0$) after the theoretical surgery. This trend was directly correlated to the magnitude of the treatment and decreased as the initial apical

radius of curvature (R_1) increased. The results of previously described investigations do not match the predictions made by Gatinel, et al. This indicates that either the Munnerlyn algorithm is not used clinically or some other factors, such as biomechanical changes in the cornea (Roberts, 2002), are affecting the results of laser refractive surgery.

Schwiegerling and Snyder (2000) used a previously described schematic eye model (Schwiegerling, et al., 1996) to investigate the spherical aberration induced by PRK and propose customized ablation patterns to compensate for this aberration. Their schematic model consisted of a two surface cornea and a two surface lens with a constant refractive index. Pre and post-surgical (9 weeks post-op) corneal topographies were obtained, with a TMS-1, from 16 patients who had PRK with an OmniMed excimer laser (Summit). The ablation zone in all procedures was 6.0 mm and the attempted corrections ranged from -1.25 to -6.12 D. Topographic measurements from the TMS-1 were decomposed into a set of Zernike polynomials by previously described techniques (Schwiegerling, et al., 1995; Brenner, 1997). Only the rotationally symmetric Zernike terms were then used to represent anterior corneal surfaces in pre and postoperative schematic eye models. Exact ray tracing, in optical design software (Code V), was then used to determine the longitudinal spherical aberration (LSA) in these models. The surgically induced change in LSA was found by comparing the LSA of corresponding pre and post-op models. Code V's optimization routines were then used to propose ablation patterns that would provide the best overall optical performance. The LSA was found to increase after PRK and it correlated with the amount of attempted correction such that approximately 0.25 D of LSA was induced for each dioptre of attempted correction for a 4 mm pupil. The proposed ideal ablation patterns were found to be slightly deeper centrally than current patterns but maintained the same central curvature. While, the authors did not quantify how the proposed ablations would change corneal shape, they suggested that deeper ablations would cause increased peripheral flattening that could compensate for spherical aberration

Since it had been established that laser refractive surgery induced a strong increase in high-order optical aberrations that correlated with a significant decrease in the quality of vision, research was initiated to develop ablation profiles that could control or eliminate high-order aberrations. Meanwhile, scanning spot lasers that precisely remove tissue in an area less than 1 mm in diameter and aberrometers that measure the aberrations of individual patients have become clinically available. The availability of these instruments has led researchers to develop wavefront-guided

ablations, which are customized to remove the aberrations of an individual (MacRae, et al., 1999; MacRae, 2000). The steps involved in wavefront-guided refractive surgery include measurement of the wavefront aberrations with an aberrometer and the mathematical transfer of the aberrations into an adequate ablation pattern to be performed by a scanning-spot excimer laser (Mrochen, et al., 2001).

The efficacy of a clinical application of wavefront-guided LASIK was investigated by Mrochen, et al. (2001b). This study reported on 31 eyes from 24 patients who had received customized surgery with an Allegretto excimer laser (WaveLight Laser Technologie), which has a 1.0 mm scanning-spot and an eye-tracker. Aberration measurements were made with a Tscherning aberrometer and described with Zernike polynomials for a pupil size of 5.0 mm in diameter. The mean age of these subjects was 31 ± 7 years (range 20 to 44). The mean spherical correction was -4.8 ± 2.3 D (range -1.0 to -9.5 D) and the mean cylinder correction was -1.1 ± 2.3 D (range 0 to -3.5 D). Preoperatively 100% of the eyes had an uncorrected visual acuity (UCVA) worse than 20/40. At 3 months UCVA of 20/16 or better was reported in 64.5% (n=20) of the eyes. All eyes had a best spectacle corrected visual acuity (BSCVA) of at least 20/25. A BSCVA of 20/10 or better was achieved in 16.1% of the eyes (n=5). Low contrast visual acuity (LCVA) was reported to decrease in 19.4% (n=6), not change in 54.8% (n=17) and increase in 25.8% of the eyes (n=8). Glare visual acuity (GVA) was found to decrease in 25.8% (n=8), not change in 51.6% (n=16) and increase in 22.6% of the eyes (n=7). On average, the high-order RMS was not significantly altered at 3 months compared to preoperative values (increase factor 1.44 ± 0.74; $p=0.2$). The RMS values for all high-order aberrations showed no significant difference 3 months after surgery except for the 4^{th} order RMS (increase factor of 2.02 ± 1.35; $p<0.05$). Analysis of the aberrations in each individual eye revealed a decrease in higher-order aberrations in 22.5% (n=7). The 3^{rd} order aberrations were reduced in 48.4% (n=15) but only 9.7% showed a decrease in 4^{th} order aberrations. Based on their desired goal to correct all high-order aberrations, the authors reported that although they achieved a fair correction of coma, their ability to correct spherical aberration was insufficient.

As new surgical techniques are developed their efficacy could be tested if an eye model existed that has been shown to accurately predict postoperative aberrations. To develop such a model, I simulated laser refractive surgery by changing the shape and thickness of the cornea in the previously defined asymmetric myopic model (Chapter 5) by two techniques.

Initially, I calculated the change in corneal shape and thickness that would occur from theorectical ablations defined by Munnerlyn, et al. (1988) and developed eye models based on the results. It was probable that these eye models would not predict the clinically observed postoperative aberrations since it has been shown that the postoperative anterior corneal asphericity predicted by these equations (Gatinel, et al., 2001) do not match clinical observations (Hersh, et al., 1996). Regardless, the aberrations predicted by postoperative models developed from ablation equations could provide insight that leads to more accurate models.

Based on the results from the ablation equation models, I decided to simulate postoperative corneal shape and postoperative eye models by utilizing clinical measurements. Comparisons of pre and postoperative corneal topographies were used to determine average shape changes in the anterior corneal surface and to predict postoperative aberrations as a function of preoperative refractive error.

6.2 Methods

Refractive surgery is modeled by simulating the surgically induced changes in the shape of the anterior corneal surface. Shape changes will be calculated from ablation equations (Munnerlyn, et al., 1988) and by comparing pre and postoperative corneal topographies. The effect of these simulations on the aberrations of eye models will be determined by replacing the anterior corneal surface of the asymmetrical models introduced in Chapter 5, with the new postoperative corneal surfaces.

6.2.1 Post-surgery Models Developed from Ablation Equations

Refractive surgery was simulated with ablation equations by first assuming that the anterior corneal surface could be described by a symmetrical conic surface. This is a reasonable assumption since the ablation equations were designed to correct only a spherical refractive error (Munnerlyn, et al., 1988). The simulation can then be simplified by describing the shape of the anterior corneal surface of the model with the contour of a single semi-meridian. In the future, asymmetrical ablations providing astigmatic corrections could be analyzed by extending this methodology.

Seven myopic (-2 to -8 D) preoperative, anterior, corneal contours were defined. Each corneal contour consists of a series of data points defining their radial distance from the apex (r) and aspheric sag (Z_{PRE}). The spatial coordinates range from 0 to 2.5 mm and are separated by 0.1mm. The preoperative sag was calculated as

$$Z_{PRE}(r) = z_o - \frac{R_{PRE} - \sqrt{R_{PRE}^{\ 2} - (1+Q_{PRE})r^2}}{1+Q_{PRE}} \qquad 6.1$$

The values of R_{PRE} and Q_{PRE} were taken from the asymmetrical models with symmetrical corneas (SC) that were introduced in Chapter 5 (Table 5.2). z_o is a constant offset that is used to simplify the modeling process.

The effect of refractive surgery is defined as the change in anterior corneal elevation or ablation depth at each data point in the corneal contours. The ablation depth (AD) was calculated from equations 6.2 and 6.3 originally developed by Munnerlyn, et al. (1988).

$$R_{PST-C}(Rx) = \frac{R_{PRE}(n-1)}{R_{PRE}Rx + (n-1)} \qquad 6.2$$

$$AD(r) = \sqrt{R_{PRE}{}^2 - r^2} - \sqrt{R_{PST-C}{}^2 - r^2} - \sqrt{R_{PRE}{}^2 - (D/2)^2} + \sqrt{R_{PST-C}{}^2 - (D/2)^2} \qquad 6.3$$

R_{PST-C} represents the post-op central radius of curvature of the anterior corneal surface that would be required to correct a refractive error of Rx if the preoperative central radius of curvature was R_{PRE}. n is the refractive index of the cornea. D, the diameter of the ablation zone, was chosen to be 6.0 mm since this is a common clinically used value and so that the corneal contours, modeled within a 5 mm diameter, were completely encompassed within the ablation zone.

The elevations of post-op, anterior corneal contours were calculated by subtracting the ablation depth from the preoperative elevation at each point ($Z_{PST}(r) = Z_{PRE}(r) - AD(r)$). The shape of the postoperative corneal contours, defined by their central radius of curvature (R_{PST-F}) and asphericity (Q_{PST-F}), was then determined by fitting a conic sag equation (similar to equation 6.1) to its elevation data. This whole process was performed with the software package Mathcad (MathSoft, Inc.).

Postoperative eye models were then built by replacing the anterior corneal surface of the asymmetrical SC models with the newly calculated postoperative anterior corneal surfaces. Corneal thickness was reduced by the calculated apical ablation depth (AD(0)). No changes were made to the shape of the posterior corneal surface or any other parameter in the preoperative models. The aberrations predicted by the postoperative models were calculated, for a 5mm pupil, and then compared to the corresponding preoperative model predictions and empirical results.

6.2.2 Surgically Induced Changes in Corneal Topography

Postoperative corneal topographies were obtained from 143 eyes of 97 subjects from the group originally introduced in Chapter 4. PRK had been performed on these subjects at the University of Ottawa Eye Institute with a STAR excimer laser (VISX Inc.). This laser utilizes an expanding diaphragm and all surgeries had an ablation diameter of 6 mm. The surgery attempted to correct both spherical and cylindrical refractive errors but the exact surgical algorithm was unavailable. Postoperative measurements of refractive error and corneal topography were obtained six months after the surgery was performed.

Topography of the anterior corneal surface was once again measured on a PAR CTS. These measurements were fit with a biconic and the surface parameters were converted to JCC components by the procedure previously described in Chapter 4. The approximation needed to transform the biconic surface parameters to JCC terms was once again considered valid if the corresponding error in the aberration of the surface did not exceed ¼λ. In cases where the error in aberration exceeded ¼λ, the approximation was considered invalid and these topographies were removed from the remaining analysis.

Similar to the method described by Thibos and Horner (2001) for refractive error, the surgically induced change (Δ) in the JCC components of both refractive error and anterior corneal shape were determined by subtracting the preoperative component from the postoperative component. Statistically significant correlations between the changes in JCC components of anterior corneal shape and ocular refraction and the amount of preoperative spherical equivalent ($RE_{M\text{-}PRE}$) were determined with the same statistical tests that were performed in Chapter 4.

Based on the statistically significant linear correlations, the average changes in paraxial power (ΔP_M) and asphericity (ΔQ_M) of the anterior corneal surface were determined as a function of preoperative refractive error. The average, topographically measured, postoperative anterior corneal shape parameters ($P_{PST\text{-}T}$ and $Q_{PST\text{-}T}$) were then determined, as a function of preoperative refractive error, by adding the average surgically induced changes to the average preoperative shape parameters (P_{PRE} and Q_{PRE}) from Chapter 4.

Postoperative eye models were built by replacing the anterior corneal surface of the asymmetrical models with symmetrical corneas with the newly calculated average postoperative anterior corneal surfaces. Although the surgeries examined here did attempt to correct the cylinder as well as the spherical refractive error, the subjects studied were restricted to those with preoperative cylinder of less than or equal to 2.50 D. Since no data on the change in corneal thickness for these subjects exists, the corneal thickness of the models was reduced by the calculated apical ablation depth (AD(0)) from Section 6.3.1. Once again, no changes were made to the shape of the posterior corneal surface or any other parameter in the preoperative models. The aberrations that these models predict were calculated, for a 5mm pupil, and then compared to the preoperative and ablation equation model predictions and empirical results.

6.3 Results

6.3.1 Postoperative Corneal Shape Derived from Ablation Equations

Table 6.1 displays the shape parameters of the corneal contours from the simulation ablation equations. Figure 6.1 displays the pre and postoperative corneal contours for an -8D myope. The postoperative asphericity (Q_{PST-F}) values are seen to become slightly more prolate after the surgery simulation.

Table 6.1: Results from the Ablation Equation Simulation. R_{PST-C} is the calculated postoperative central radius of curvature. AD(0) is the calculated central ablation depth. R_{PST-F} and Q_{PST-F} represent the central radius of curvature and asphericity of the conic section that were the best fit to the calculated postoperative corneal elevation data.

Rx (D)	R_{PRE} (mm)	Q_{PRE}	R_{PST-C} (mm)	AD(0) (mm)	R_{PST-F} (mm)	Q_{PST-F}
-1	7.787	-0.262	7.952	0.013	7.952	-0.281
-2	7.754	-0.239	8.088	0.027	8.087	-0.275
-3	7.722	-0.216	8.229	0.040	8.229	-0.267
-4	7.690	-0.192	8.375	0.054	8.375	-0.255
-5	7.658	-0.169	8.526	0.067	8.526	-0.241
-6	7.627	-0.146	8.684	0.080	8.683	-0.224
-7	7.595	-0.123	8.846	0.093	8.845	-0.203
-8	7.565	-0.100	9.016	0.107	9.016	-0.178

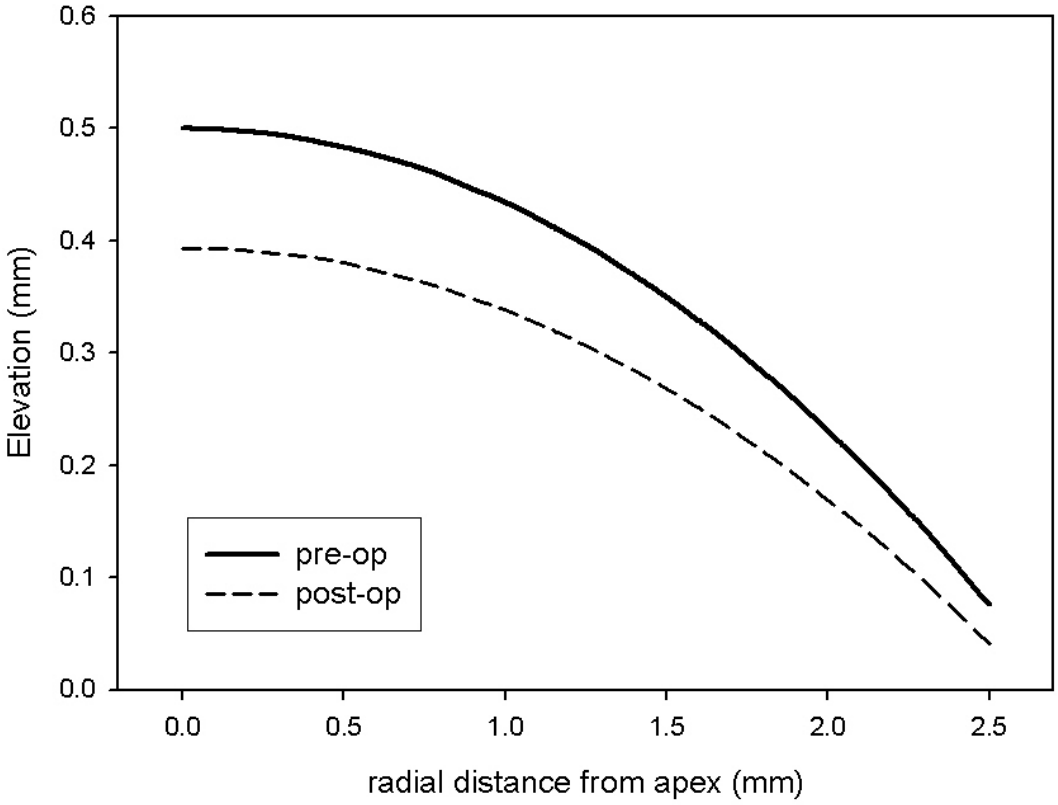

Figure 6.1: Pre and Postoperative Anterior Corneal Contours for an -8 D myope. The conic parameters defining these contours are displayed in Table 6.1

6.3.2 Surgically Induced Changes in Corneal Topography

Within the group of 143 eyes that underwent refractive surgery, 7 eyes of 7 subjects were removed during the analysis in Chapter 4 because the JCC approximation of their preoperative cornea introduced an error in aberrations (ΔW) that exceeded the allowable limit of $\frac{1}{4}\lambda$. Potential aberration errors greater than $\frac{1}{4}\lambda$ were found when the postoperative anterior corneal shapes of 11 eyes from 10 subjects were described with JCC components. The results from these subjects are shown in Table 6.2. The error in the asphericity approximation (Q_E) and the changes in the paraxial power ($\Delta P = P_2 - P_1$) and asphericity ($\Delta Q = \left|Q_2 - Q_1\right|$) between principal meridians in each of the cases shown in Table 6.2 are much larger than the average values of $Q_E = 0.012 \pm 0.015$, $\Delta P = 1.15$

± 0.66 D and ΔQ = 0.84 ± 0.74 for the remaining subjects. Five of the cases were found to have substantially larger ΔW (>½λ, <λ) than the other 6 cases. In these cases it can also be seen that the ΔP and ΔQ were also substantially larger. For these 5 eyes, Q_E varied between 0.13 and 0.22.

Table 6.2: Postoperative Cases that Violate the ¼ λ Rule

Sub	Eye	SE_{PRE} (D)	SE_{POST} (D)	ΔW (λ)	Q_E	ΔP (D)	ΔQ
1	OS	-4.50	-1.75	0.72	0.164	3.74	3.89
2	OD	-4.50	0.13	0.38	0.084	3.22	2.34
2	OS	-5.25	-0.75	0.29	0.069	2.93	2.09
3	OS	-5.13	0.00	0.29	0.067	2.55	2.32
4	OD	-5.25	-0.25	0.28	0.076	2.81	2.29
5	OD	-6.00	-0.25	0.87	0.216	4.02	4.55
6	OD	-6.25	0.00	0.74	0.170	3.66	4.06
7	OS	-6.25	0.25	0.29	0.076	1.72	3.66
8	OD	-6.25	-1.00	0.73	0.165	3.87	3.73
9	OD	-6.75	0.00	0.25	0.071	2.19	2.67
10	OD	-7.38	0.75	0.59	0.135	3.65	3.27

The age and refractive error of the remaining 125 eyes from 80 subjects that had their postoperative anterior corneal topography described with JCC components are shown in Table 6.3. Since the JCC refractive error parameters did not follow a normal distribution, Rank Sum Tests were used to compare pre and postoperative median values. Both RE_M and RE_{J0} were found to have a surgically induced statistically significant decrease ($p<0.001$). Although RE_{J45} was observed to decrease postoperatively, its change was not statistically significant ($p=0.35$) possibly because it was so small to begin with.

Table 6.3: Refraction Statistics of the Refractive Surgery Subjects

	Age	RE_M (D)		RE_{J0} (D)		RE_{J45} (D)	
	(years)	pre-op	post-op	pre-op	post-op	pre-op	post-op
Average	38	-4.80	-0.07	0.19	0.02	0.04	0.00
SD	9	1.90	0.33	0.39	0.07	0.23	0.03
Maximum	62	-1.38	1.25	1.17	0.25	0.96	0.19
Minimum	21	-9.00	-0.75	-0.88	-0.23	-0.87	-0.11

Table 6.4: Correlation Coefficients. The shaded values represent correlations that were tested for statistical significance.

	ΔRE_M	ΔRE_{J0}	ΔRE_{J45}	ΔP_M	ΔP_{J0}	ΔP_{J45}	ΔQ_M	ΔQ_{J0}	ΔQ_{J45}
RE_{MPRE}	0.974	-0.454	-0.208	0.892	-0.278	-0.001	-0.491	0.105	0.103
ΔRE_M		-0.351	-0.155	0.910	-0.241	0.010	-0.481	0.091	0.076
ΔRE_{J0}			0.221	-0.315	0.550	0.034	0.118	-0.264	-0.071
ΔRE_{J45}				-0.104	-0.033	-0.022	-0.051	0.175	-0.036
ΔP_M					-0.288	0.069	-0.674	0.169	0.060
ΔP_{J0}						-0.147	0.224	-0.831	-0.081
ΔP_{J45}							-0.149	0.165	-0.278
ΔQ_M								-0.209	-0.088
ΔQ_{J0}									0.086

The correlation coefficients between the preoperative mean refractive error and the change in the JCC components of refractive error and shape of the anterior corneal surface are shown in Table 6.4. The statistical significance of the relationships where the absolute value of their correlation coefficient is greater than 0.2 was determined with regression analysis with a Huber/White robust estimate of variance. This test was used since it accounts for instances when data points originate from the right and left eyes of the same subject. The results of the regression analysis are shown in Table 6.5.

Very strong positive correlations are seen between $RE_{M\text{-}PRE}$ and ΔRE_M, $RE_{M\text{-}PRE}$ and ΔP_M and ΔRE_M and ΔP_M. Strong negative correlations were also found between ΔP_M and ΔQ_M and ΔP_{J0} and $\Delta Q_{J0.}$ Figure 6.2 displays the linear regressions with R^2 greater than 0.4.

The shape of the topography driven postoperative anterior corneal surfaces in the model (Table 6.6) was determined by first using the linear regression results to determine the average change in refractive error and shape parameters. The average change in mean refractive error (ΔRE_M) was determined from its relationship to preoperative mean refractive error ($RE_{M\ PRE}$). The average change in the mean central power (ΔP_M) was then determined from ΔRE_M. This relationship was used because its correlation coefficient (0.91) was larger than the correlation coefficient for ΔP_M and $RE_{M\ PRE}$ (0.89). The average change in the mean asphericity (ΔQ_M) was then determined from its relationship to ΔP_M because their correlation coefficient (-0.67) was larger than the correlation coefficients for $RE_{M\ PRE}$ (-0.49) and ΔRE_M (-0.48). Postoperative conic shape parameters ($R_{PST\text{-}T}$, $Q_{PST\text{-}T}$) were determined from

$$R_{POST-T} = (n-1)\left(\frac{n-1}{R_{PRE}} + \Delta P_M\right)^{-1} \qquad 6.4$$

$$Q_{POST-T} = Q_{PRE} - \Delta Q_M \qquad 6.5$$

where R_{PRE} and Q_{PRE} are the shape parameters of the anterior corneal surface in the preoperative models and n is the refractive index of the cornea.

The asymmetric parameters of the anterior corneal surface in the postoperative topography models could be determined by starting with the relationship between ΔRE_{J0} and ΔRE_M or RE_{MPRE}. But the corresponding preoperative asymmetric models with biconic anterior corneal shape, developed in Chapter 5, were designed to have a constant cylinder refractive error while the empirical data, introduced in Chapter 4, revealed a correlation between RE_M and RE_{J0}. It would be inappropriate to use ΔRE_{J0} values calculated from its relationship to ΔRE_M or RE_{MPRE} from Chapter 4 data for postoperative models that had constant RE_{J0} preoperatively. Instead the relationship between ΔRE_{J0} and RE_{J0PRE} should be used.

Although it was not included in the original analysis, linear regression between ΔRE_{J0} and RE_{J0PRE} revealed a p-value of less than 0.0001, a R^2 of 0.952, a slope of -0.974 and an intercept of 0.042. The asymmetric models with biconic anterior corneas were designed to have RE_{J0} of 0.5 D, P_{J0} of 0.765 D and Q_{J0} of -0.006 preoperatively. Based on their preoperative values and the linear regressions between ΔRE_{J0} and RE_{J0PRE}, ΔP_{J0} and ΔRE_{J0} and ΔQ_{J0} and ΔP_{J0} (Table 6.5) values for P_{J0} and Q_{J0}, for the postoperative models, were determined to be 0.372 D and 0.439. These values fall within the postoperative ranges of the topography subjects which are 1.07 D to -1.38 D for P_{J0} and 1.07 to -1.83 for Q_{J0}.

Compared to the preoperative models, the shape of the anterior cornea in the postoperative models shows a smaller change in paraxial power and a larger change in the asphericity between principal meridians. The sag of postoperative conic and biconic anterior corneal surfaces was calculated as it was in Chapter 5 for the preoperative models. Similar to the preoperative case the sag at the principal meridians of the postoperative biconic surfaces differed from corresponding posteroperative conic surfaces by only ± 7 μm. Since the difference between the corresponding postoperative conic and biconic surfaces was similar to the preoperative cases and the small amount of asymmetry in the biconic corneas of the preoperative models did not affect their predicted aberrations, I assumed that the small amount of asymmetry in the postoperative biconic corneas would not affect the postoperative model's predicted aberrations. Consequently I decided to base my topography driven postoperative models on the asymmetrical models with the symmetrical conic anterior corneal surfaces.

Table 6.5: Linear Regression Results. The regression results were considered statistically significant if their p-value was less than 0.05.

Independent	Dependent	F(1,79)	p-value	R^2	Slope	Intercept
$RE_{M\ PRE}$	ΔRE_M	1348.51	<0.001	0.948	0.993	0.388
	ΔRE_{J0}	15.50	<0.001	0.206	-0.086	-0.270
	ΔRE_{J45}	1.94	0.168	0.043		
	ΔP_M	307.60	<0.001	0.796	1.064	0.115
	ΔP_{J0}	6.79	0.011	0.077	-0.092	-0.273
	ΔQ_M	19.52	<0.001	0.241	-0.202	-0.135
ΔRE_M	ΔRE_{J0}	8.21	0.005	0.123	-0.065	-0.135
	ΔP_M	410.74	<0.001	0.829	1.064	-0.335
	ΔP_{J0}	4.89	0.030	0.058	-0.078	-0.170
	ΔQ_M	18.97	<0.001	0.231	-0.194	-0.011
ΔRE_{J0}	ΔRE_{J45}	2.79	0.099	0.049		
	ΔP_M	10.19	0.002	0.099	-1.979	-5.025
	ΔP_{J0}	79.68	<0.001	0.303	0.956	0.033
	ΔQ_{J0}	18.89	<0.001	0.070	-0.369	0.114
ΔP_M	ΔP_{J0}	9.05	0.004	0.083	-1.042	-5.161
	ΔQ_M	43.96	<0.001	0.455	-0.232	-0.342
ΔP_{J0}	ΔQ_M	6.84	0.011	0.050	0.279	0.848
	ΔQ_{J0}	143.87	<0.001	0.690	-0.669	0.183
ΔP_{J45}	ΔQ_{J45}	11.30	0.001	0.077	-0.206	0.077
ΔQ_M	ΔQ_{J0}	4.35	0.040	0.044	-0.135	0.172

Table 6.6: Shape Parameters for the Postoperative Topography Simulation

$RE_{M\ PRE}$	ΔRE_M	ΔP_M	ΔQ_M	R_{PRE}	Q_{PRE}	R_{PST-T}	Q_{PST-T}
-2	-1.598	-2.035	0.130	7.754	-0.239	8.094	-0.109
-3	-2.591	-3.092	0.375	7.722	-0.216	8.245	0.160
-4	-3.583	-4.149	0.621	7.690	-0.192	8.403	0.428
-5	-4.576	-5.205	0.866	7.658	-0.169	8.566	0.697
-6	-5.569	-6.262	1.111	7.627	-0.146	8.736	0.965
-7	-6.562	-7.319	1.356	7.595	-0.123	8.913	1.234
-8	-7.554	-8.375	1.602	7.565	-0.100	9.097	1.502

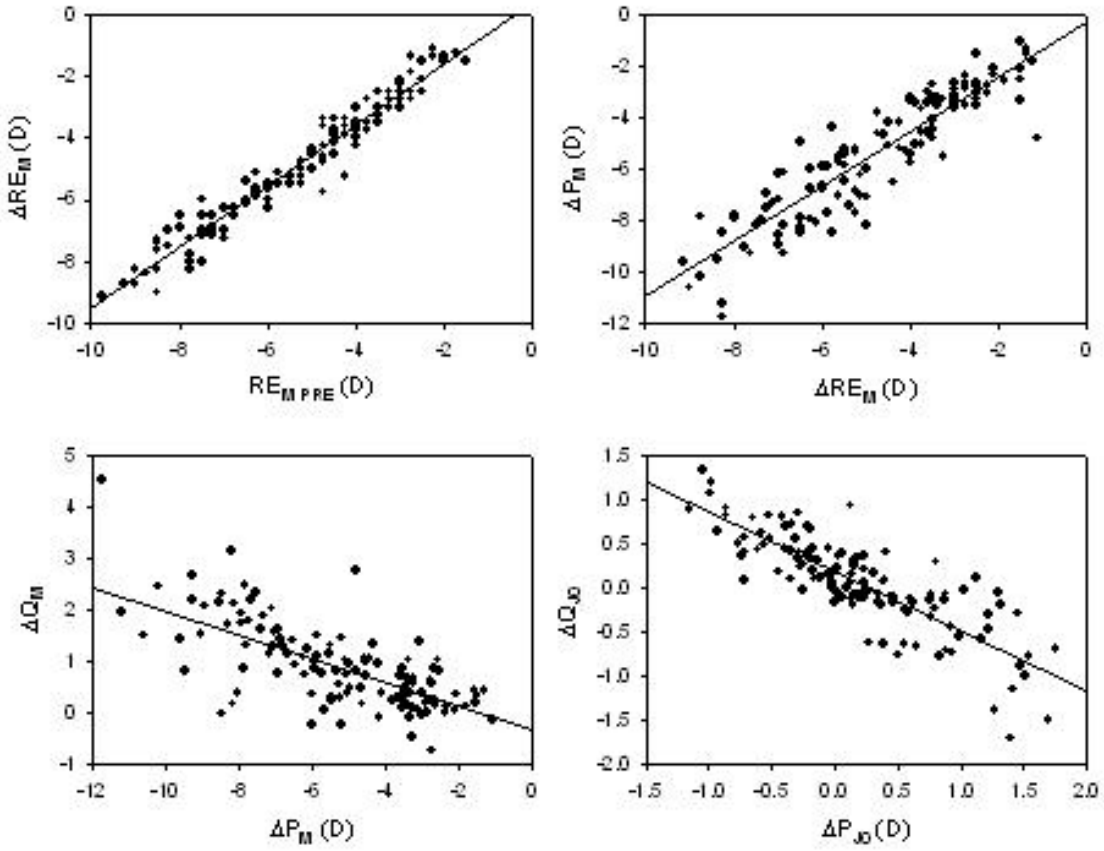

Figure 6.2: Data and Linear Fits for ΔRE_M vs. $RE_{M\text{-}PRE}$, ΔP_M vs. ΔRE_M, ΔQ_M vs. ΔP_M and ΔQ_{J0} vs. $\Delta P_{J0.}$ The correlations, shown here, are the most significant ($R^2 > 0.4$) that were found. Table 6.5 lists all the correlations that were significant. Some of these correlations show that correcting the refractive cylinder (ΔRE_{J0}) caused a change in the asymmetry of the anterior corneal surface (ΔP_{J0}, ΔQ_{J0}). These results were not included in the postoperative topography models since it was determined that the asymmetry in the postoperative biconic anterior corneal surfaces did not change their shape significantly compared to corresponding postoperative conic surfaces defined by ΔP_M and ΔQ_M.

6.3.3 Aberrations of the Postoperative Eye Models

Table 6.7 and Figure 6.3 display the aberrations of the pre and the two types of postoperative models. The refractive error of the ablation equation models ($Post_E$), calculated from the postoperative Z_2^0 coefficient, was observed to be increasingly overcorrected, while their spherical aberration, coma RMS and high-order RMS all decreased as the myopic refractive error of their corresponding preoperative models increased. The calculated refractive errors of the corresponding postoperative topography models ($Post_T$) were increasingly undercorrected while their spherical aberration, coma RMS and high-order RMS all significantly increased.

Table 6.7: Aberrations of the Pre and Postoperative Eye Models

Refractive Error (D)	Pre	-2	-3	-4	-5	-6	-7	-8
	$Post_E$	0.19	0.27	0.34	0.40	0.45	0.49	0.53
	$Post_T$	-0.03	-0.27	-0.47	-0.66	-0.82	-0.95	-1.06
Spherical Aberration (μm)	Pre	0.043	0.050	0.058	0.065	0.073	0.081	0.090
	$Post_E$	0.020	0.016	0.013	0.010	0.007	0.005	0.003
	$Post_T$	0.066	0.131	0.191	0.248	0.299	0.345	0.385
Coma RMS (μm)	Pre	0.039	0.047	0.057	0.069	0.082	0.096	0.111
	$Post_E$	0.028	0.023	0.018	0.012	0.008	0.009	0.014
	$Post_T$	0.074	0.194	0.307	0.414	0.510	0.597	0.673
High-Order RMS (μm)	Pre	0.093	0.108	0.129	0.150	0.174	0.200	0.226
	$Post_E$	0.055	0.045	0.035	0.025	0.018	0.017	0.023
	$Post_T$	0.157	0.370	0.572	0.763	0.936	1.092	1.228

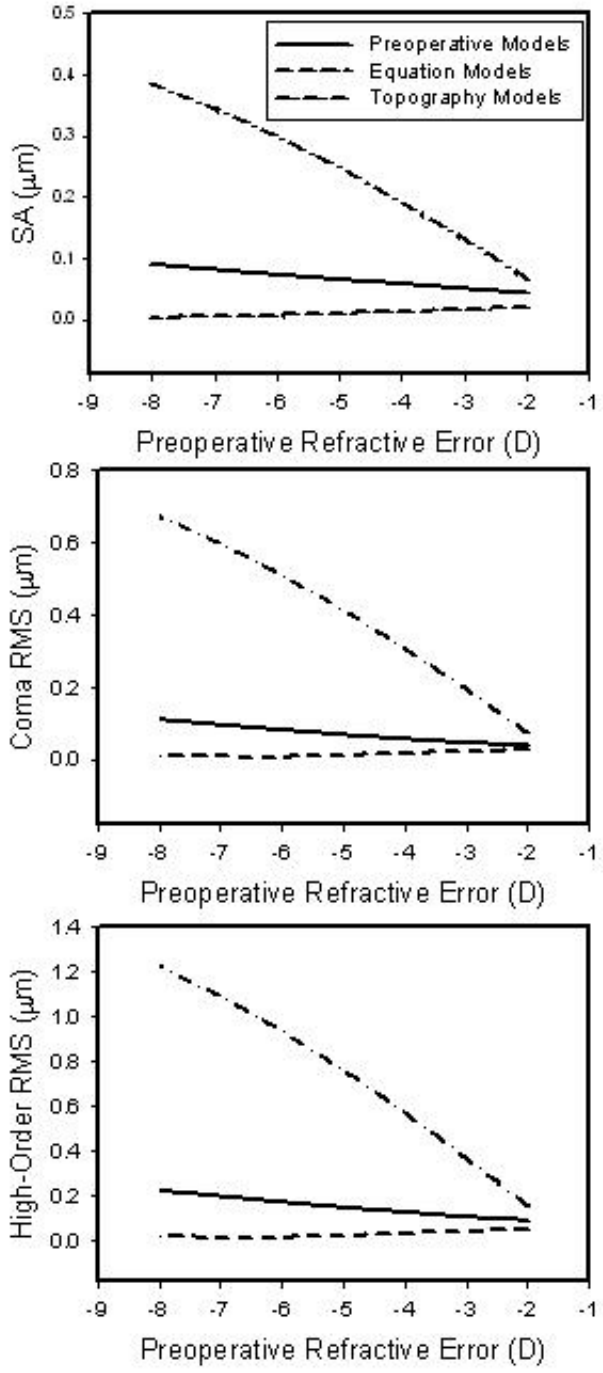

Figure 6.3: Aberrations of the Pre and Postoperative Models

6.4 Discussion and Conclusions

When PRK was simulated with the equations developed by Munnerlyn, et al. (1988), the preoperative prolate asphericity values of the anterior corneal surface used in my models became increasingly more prolate as a function of attempted correction. This result was expected (Gatinel, et al., 2001) but is not consistent with the clinical observation that the asphericity of the anterior cornea becomes oblate postoperatively (Hersh, et al., 1996), which demonstrates that the postoperative shape predicted by the Munnerlyn equations is not anatomically accurate.

Postoperative eye models, based on the anterior corneal shape from the equation simulation predicted that Zernike defocus would be slightly over corrected but that high-order aberrations would decrease. While correcting defocus within 0.5 D models empirical results (Jackson, 2001), the predicted decrease in high-order aberrations is not the clinically observed result. The increased prolateness of the postoperative anterior corneal surface also did not match with empirical measurements. This result led me to develop postoperative eye models by incorporating anterior corneal surface shape derived from clinical measurements.

Clinical topographic and refraction measurements were made on 143 eyes 6 months after the PRK surgery described in the Methods. 125 eyes were analysed as described in the methods. The SE of 91% of the original cases and 94% of the eyes used in the correlation analysis were found to be within 0.5 D of emmetropia. Refractive surgical procedures are considered to be successful if postoperative SE is within 0.5 D of emmetropia (Dr. Munger, personal communication, 2004). Any conclusions drawn from this investigation can be attributed to a surgical application that was considered successful at removing refractive error but did not aim to correct aberrations. Corneal topography and aberration calculations were made for a 5 mm pupil diameter while the PRK had an ablation zone diameter of 6 mm. Consequently the transition between ablated and unablated areas has been ignored and the results correspond to changes in the anterior corneal topography and ocular aberrations within the ablation zone.

The average change in the anterior corneal shape, caused by this particular PRK surgery, was determined, as a function of preoperative SE, by comparing pre and postoperative JCC biconic surface parameters. Of the 136 eyes that had their postoperative biconic surfaces described in JCC terms, 11 eyes from 10 subjects had an error in their aberration estimate (ΔW) greater than $\frac{1}{4}\lambda$. Since this exceeded the allowable limit these eyes were removed from the remaining analysis.

Similar to the preoperative cases in Chapter 4, the eleven excluded eyes were found to all have an error in the JCC estimate of the asphericity of the meridian half way between the principal meridians (Q_E), and the difference in power (ΔP) and asphericity (ΔQ) between principal meridians that significantly exceeded the average values of the remaining eyes. It was also observed that their Q_E values all significantly exceeded the maximum allowable limit of 0.035 that was proposed for the preoperative cases in Chapter 4. This suggests that even after successful PRK, anterior corneal surface shapes can exist that have differences in central power and asphericity between the principal meridians that are too large to be accurately quantified with biconic JCC parameters. Removing these cases eliminates the chance that these surfaces could be skewing the remaining results. Regardless, the anterior surface shape of 88% of the postoperative corneas could be described with the JCC formalism.

The spherical equivalent refractive error in the remaining eyes was statistically significantly reduced by the surgery and consequently the strong correlation between $RE_{M\text{-}PRE}$ and ΔRE_M was expected. Similarly the significant reduction in cylinder would result in a strong correlation between $RE_{J0\text{-}PRE}$ and ΔRE_{J0}. Since RE_{J45} was not found to have a statistically significant decrease postoperatively, ΔRE_{J45} was not expected to correlate with any of the other parameters. The lack of preoperative oblique cylinders in this group of subjects (Chapter 4) would account for this result.

In Chapter 4, it was observed that for this group of subjects RE_M correlated with RE_{J0} but not with RE_{J45} preoperatively. It is not surprising then that $RE_{M\text{-}PRE}$ correlated with ΔRE_{J0} but not with ΔRE_{J45}. Part of the correlation may also be due to a surgical correction of the preoperative cylinder.

The surgically induced changes in refractive error (ΔRE_M, ΔRE_{J0}) were directly related to corresponding change in central anterior corneal power (ΔP_M, ΔP_{J0}). Linear regression revealed

slopes of 1.06 and 0.96 for the relationships between ΔRE_M and ΔP_M and ΔRE_{J0} and ΔP_{J0} respectively. These results indicate that the induced refractive change can be accounted for by the change in the central power of the anterior cornea. Even though postoperative changes in the central curvature of the posterior corneal surface have been previously reported, their effect on the overall change in refractive power will not be as great as changes to the shape of the anterior corneal surface. These linear regressions are understandable since the change in refractive index (Δn) at the anterior corneal surface is significantly greater than the Δn at the posterior corneal surface (Munger, 2001). From this analysis, any changes in posterior corneal power would be expected to either be small or independent of the induced change in refractive error.

Changes in the mean and J0 JCC asphericity parameters (ΔQ_M and ΔQ_{J0}) are negatively correlated, individually, with the reductions in the mean and J0 JCC components of both central anterior corneal power (ΔP_M and ΔP_{J0}) and refractive error (ΔRE_M and ΔRE_{J0}). ΔQ_{J45} only correlated negatively with ΔP_{J45}. These relationships indicate that removing corneal tissue to decrease refractive error by decreasing central anterior corneal power causes the asphericity of the anterior corneal surface to increase. The magnitude of the increase in asphericity is directly related to the amount of tissue removed.

The mean asphericity (Q_M) was found to change at a rate of -0.19 per dioptre of the change in mean refractive error (ΔRE_M). The variation in asphericity (Q_{J0}) with corneal meridian was found to change at rate of -0.37 per dioptre of the change in the angular variation in refractive error (ΔRE_{J0}). This shows that correcting astigmatism changed the postoperative asphericity twice as much as correcting a comparable amount of the mean refractive error. From this result, anterior corneal surfaces would, on average, have larger variations in asphericity with corneal meridian postoperatively. This was confirmed by comparing the average difference in the asphericity between the principal meridians (ΔQ). ΔQ was 0.38 ± 0.32 preoperatively and 0.84 ± 0.74 postoperatively by means of a t-test. The surgically induced change in ΔQ is statistically significant ($p<0.001$).

The subjects studied here had low amounts of astigmatism, preoperatively, compared to their mean refractive error. The linear regression slope indicates that, on average, ΔRE_{J0} was only 7% of ΔRE_M. On average, the change in asphericity is dominated by the change in Q_M. It could

prove interesting to examine how larger amounts of preoperative astigmatism effect the surgically induced change in anterior corneal shape.

Hersh, et al. (1996) reported the magnitude of postoperative asphericity as a function of attempted correction. To compare their results to the data reported in this chapter, linear regression was applied between the postoperative Q_M and attempted correction. Attempted correction was assumed to have the same magnitude as preoperative RE_M but with opposite sign. Linear regression revealed a significant relationship ($p<0.0001$) with a slope of 0.24 and an intercept of -0.44 while Hersh's results have a slope of 0.22 and an intercept of 0.09. T-tests revealed that the slopes were not statistically significantly different ($p=0.71$) but the intercepts were ($p=0.01$). The difference between these results could be related to the different PRK surgeries particularly given the changes in surgical methods since the study by Hersh, et al. (1996) (particularly ablation zone size), and the different corneal topographers and measurement techniques used in these investigations.

An alternative approach to determining average postoperative corneal shape as a function of preoperative spherical equivalent (SE_{PRE}) would be to investigate the correlation between the JCC components of postoperative corneal shape and SE_{PRE}. Applying this approach to the 125 eyes that were investigated here revealed coefficients of 0.68, -0.54 and -0.68 for the correlations between SE_{PRE} and $P_{M\text{-}POST}$, SE_{PRE} and $Q_{M\text{-}POST}$ and $P_{M\text{-}POST}$ and $Q_{M\text{-}POST}$ respectively. The coefficients for the correlations between SE_{PRE} and ΔP_M, SE_{PRE} and ΔQ_M and ΔP_M and ΔQ_M are 0.89, -0.49 and -0.67. The relationships between SE_{PRE} and ΔQ_M or $Q_{M\text{-}POST}$ have similar levels of correlation. Similarly the correlations between ΔP_M and ΔQ_M and $P_{M\text{-}POST}$ and $Q_{M\text{-}POST}$ are nearly identical. But SE_{PRE} has a significantly stronger correlation to ΔP_M than to $P_{M\text{-}POST}$. Better estimates of the average postoperative corneal shapes were determined by using the relationships with the stronger correlation.

To create the postoperative topography eye models, the anterior corneas of the asymmetric models with symmetrical corneas were replaced with the postoperative surfaces determined from surgically induced changes in clinical topographic measurements as a function of preoperative spherical equivalent. Symmetrical conic surfaces were used since the sag of postoperative biconic anterior corneal surfaces was not significantly different from corresponding postoperative conic surfaces and it was shown, in Chapter 5, that similar biconic and conic preoperative models

predicted identical aberrations. Low amounts of asymmetry in the anterior corneal surface have negligible effect on the predicted aberrations. Along with examining larger amounts of astigmatism it could prove interesting to examine models with larger amounts of asymmetry in the shape of the anterior corneal surface.

Central corneal thickness was also reduced as a function of preoperative refractive error. Since empirical data from the postoperative topography subjects did not exist, corneal thickness was reduced by amounts calculated from the equations of Munnerlyn, et al. (1988). Utilizing this assumption is valid since it has been observed that postoperative changes in central corneal thickness have the same magnitude as the theoretical calculations (Naroo and Charman, 2000).

Postoperative eye models, based on clinical topographic measurements, predicted that refractive defocus would be slightly undercorrected but high-order aberrations would increase significantly. Since the postoperative aberrations from the topography subjects were not available, comparisons were made to previously published empirical results of PRK (Seiler, et al., 2000) and LASIK (Marcos, et al., 2001a). Figure 6.4 displays the comparison of the surgically induced increase in the RMS of the 3rd order, 4th order and high-order aberrations. My postoperative model predicts induced differences in the aberrations that are similar to the empirical results but the results from Seiler, et al. (2000) are consistently larger while the 3rd and high-order aberrations observed by Marcos, et al. (2001a) are smaller.

The results of this comparison are difficult to interpret since there are many different variables within these investigations. For example, the aberrations were determined for a pupil diameter of 6 mm in the study by Seiler, 6.5 mm in the Marcos study and 5 mm in this investigation. The studies with the larger pupil sizes would observe larger aberrations, which could cause greater postoperative differences to be seen. The edge of the ablation zone in each of these studies is also very close to the edge of their pupil, which could also cause the aberrations to increase postoperatively.

The type of refractive surgery and how it is applied could also play a role in the size of the induced aberrations since it has been shown that the size of the ablation zone in PRK significantly affects the amount of induced corneal first surface aberrations (Oliver, et al., 1997). It has also been

shown that an application of LASIK induced more spherical and high-order anterior corneal aberrations than a similar application of PRK (Oshika, et al., 1999a).

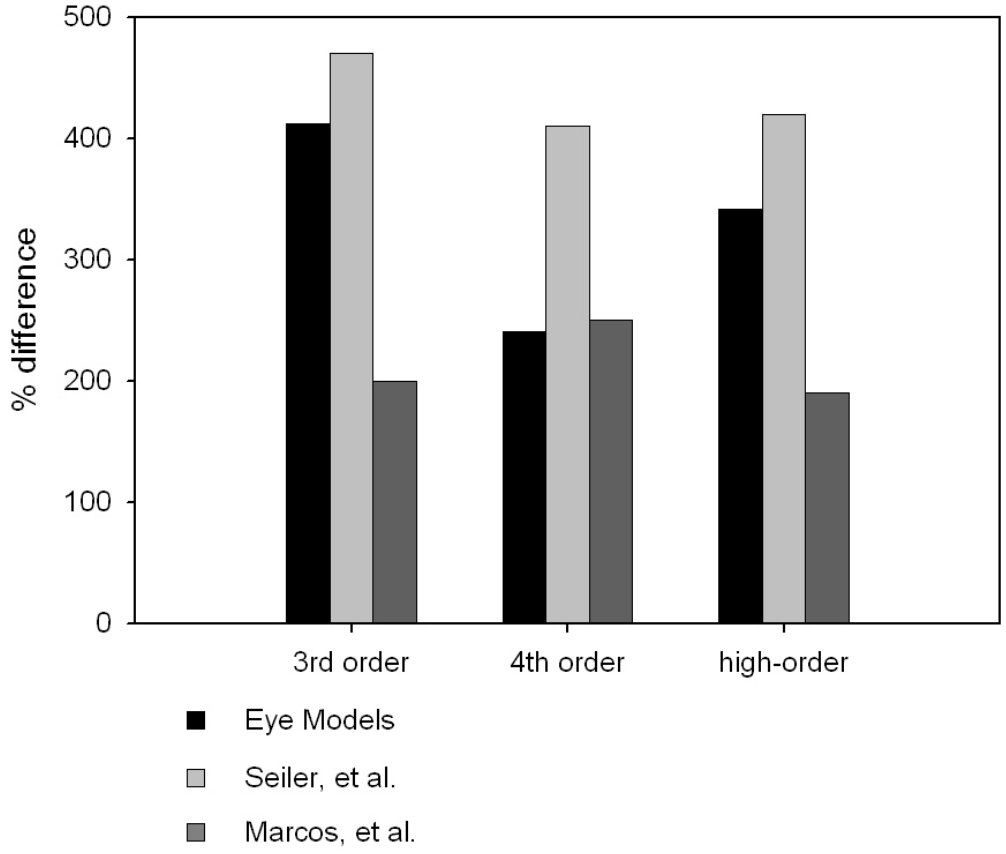

Figure 6.4: Comparison of the average surgically induced increases in the 3rd, 4th and high-order aberrations between model predictions and empirical results

The surgeries in the Seiler study and this investigation were both broad beam PRK with a 6 mm ablation zone diameter but the pupil size I used was smaller than Seiler's. Consequently I conclude that this model makes a good prediction of the induced aberrations after this type of refractive surgery since its predictions are similar to but slightly less than the empirical measurements induced by a similar surgery measured over a larger pupil.

In the Marcos study, the surgery performed was scanning spot LASIK with an eye-tracker and aberrations were determined for a 6.5 mm pupil diameter. Since the surgery was LASIK and a

larger pupil size was used, postoperative aberrations would be expected to be larger than in PRK with a similar ablation technique. However, it has been shown that use of an eye-tracker will significantly reduce the amount of induced aberrations (Mrochen, et al., 2001a). Consequently my model predictions are consistent with the expected differences between surgeries.

The predicted refractive errors of the models have been calculated from the value of the Z_2^0 coefficient by using equation 2.21 for a 5 mm pupil. The refractive errors of the postoperative topography models were slightly myopic and the level of residual myopia was observed to increase with preoperative refractive error. Figure 6.5 displays the relationship between pre and postoperative refractive error for both the topography models and the empirical data from the subjects studied in this chapter. The empirical data, which was measured by subjective refraction, shows that, on average, the refractive error was corrected by the surgery but even though most of the residual refractive error was within 0.5 D of emmetropia it can still be described as a function of the preoperative SE. Linear regression of the empirical data revealed a significant best-fit line ($p<0.001$) with a slope of -0.06 and an intercept of -0.37 D.

While the postoperative topography models predict that at least 85% of the preoperative refractive error will be corrected, the predicted residual refractive error does not correspond to the empirical results. The difference between empirical SE and model predictions were greatest at the largest preoperative refractive errors, which were predicted to have the most postoperative high-order aberrations.

Zernike polynomials represent balanced aberrations (Guirao and Williams, 2003). This means that the Zernike term representing defocus (Z_2^0) takes into account not only the paraxial power of the optical system but also the effect that high-order aberrations have on the position of the best focal plane. A recent study of 6 young normal eyes revealed that refractive errors calculated from a Zernike polynomial description of their wavefront aberrations had a mean absolute difference of 0.5 D from their subjective refraction and increased with increases in high-order aberrations. Furthermore, the difference between objective, wavefront based refraction and subjective refraction correlated with the amount of wavefront error across 146 subjects (Guirao and Williams, 2003). Since postoperative high-order aberrations are significantly larger than in normal eyes, the difference between subjective and Zernike wavefront derived refraction would be expected

to be even higher than 0.5 D and could account for the difference between the refractive error of the models and empirical data.

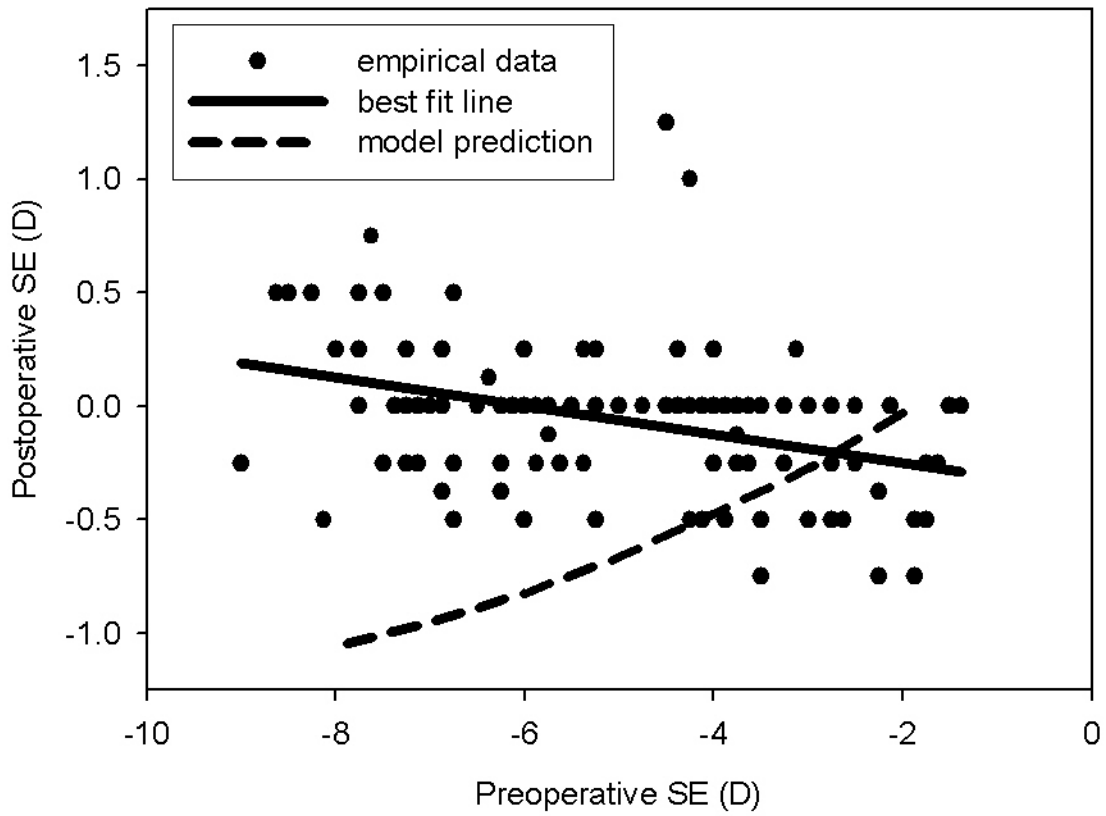

Figure 6.5: Pre and Postoperative Refractive Error of the Empirical Data and Topography Model. The empirical data was measured by subjective refraction while the topography model predictions were calculated from the defocus term in a Zernike polynomial series.

The postoperative topography models were created by changing only the shape of the anterior corneal surface and central corneal thickness. Previously, changes in the posterior corneal surface have been reported (Kamiya, et al., 2000; Naroo and Charman, 2000; Seitz, et al., 2001). Observed differences between the ocular and anterior corneal surface spherical aberration have been attributed to surgically induced changes in the shape of the posterior corneal surface (Marcos, et al., 2001a). Incorporating changes in the posterior corneal surface into the postoperative topography

model may enhance its ability to predict the induced changes in aberrations and residual refractive error. However, in this analysis, changes in the front surface of the cornea accounted for changes in the ocular aberrations. Differences observed by Marcos, et al. (2001a) may arise from systematic differences between the measurements of corneal and ocular aberrations.

To truly gauge the efficacy of creating a postoperative model by incorporating surgically induced changes in the cornea would require access to pre and postoperative measurements of anterior and posterior corneal surface shape, central corneal thickness and ocular aberrations from a single large group of subjects who had received the same refractive procedure. Unfortunately this information was not available but I was able to show that a postoperative eye model, which accurately incorporates anterior corneal surface changes between normal and postoperative populations, predicts how the surgery affects aberrations.

Previous reports of surgically induced changes in anterior corneal topography (Hersh, et al., 1996) utlilized a symmetrical conic to describe the shape of the anterior corneal surface and have focused on the changes in asphericity. To determine the surgically induced corneal shape changes, a biconic descriptor expressed in JCC terms was used. This type of description is useful because its orthogonal components provide a straightforward method to determine surgically induced changes (post-pre) and direct correlation of parameters describing changes in refractive error and corneal shape. The biconic is superior to other orthogonal descriptors, such as Zernike polynomials, because it has been shown that an asymmetric conic model provides a better description of normal corneal shape than a Zernike series (Preussner, et al., 2003).

The future of refractive surgery is customized ablations based on the unique aberrations of a specific patient. Eye models provide useful tools to plan and evaluate new procedures. The topography models, described here, would provide an excellent model to investigate new ablation algorithms because they show correlations between changes in refractive error and the shape of the anterior corneal surface. However, these models are limited since they are developed to be average eye models. In particular, the JCC description of corneal shape may not be able to adequately describe the shape of unusual corneas.

7 Summary

The goal of this research was to develop an anatomically based, GRIN eye model that predicts the average high-order aberrations of young adults as a function of myopia. The new models were then used to investigate the surgically induced high-order aberrations that have been clinically observed after laser refractive surgery.

It was shown that anatomically based, young adult, GRIN, symmetrical eye models can be built that accurately predict the average spherical aberration (SA) of emmetropic and myopic young adults. But these models do not predict the total amount of aberrations that have been clinically observed since they do not predict asymmetrical aberrations. When the object was moved from infinity to the model's far point, it was observed that the predicted SA by the GRIN models did not change appreciably. Slightly larger changes in the aberrations were observed if the GRIN was replaced with a constant refractive index.

The myopia in these models was simulated by either purely axial or refractive means, which caused the models to be anatomically inaccurate. This was not surprising, as myopia is known to be a combination of axial and refractive components. Even though the symmetrical models did accurately predict SA, which was their primary goal, enhancements were made to see if models could be developed that accurately predicted average asymmetrical aberrations and simulated myopia in an anatomically accurate manner while maintaining the SA prediction.

To enhance the symmetrical models, the shape of the anterior corneal surface was investigated. A biconic was found to provide a more accurate description of the shape of the anterior corneal surface in normal subjects than less complex surfaces. The improved accuracy provided by the biconic was statistically significant for a majority of subjects. In the cases where it was not significant, a specific corneal surface closely resembled a less complex surface.

Parameters describing the refractive error and the shape of the anterior corneal surface were described in Jackson Cross Cylinder (JCC) components to determine if correlations exist between anterior corneal surface shape and the components of refraction. Asphericity parameters could only be expressed in JCC terms by utilizing an approximation. The approximation was assumed to be

valid if the variation in central corneal power and asphericity were small enough that the spherical aberration of the approximated and real surfaces never differed by more than ¼λ. An expansion showed that the first approximation was valid when the square of the power variation and the asphericity difference with meridian were small.

Comparisons between the JCC parameters of refractive error and biconic shape of the anterior corneal surface revealed that mean refractive error correlated individually with mean central power and mean asphericity. The mean central power and mean asphericity of the anterior corneal surface were not related. The variation in refractive error with meridian correlated individually with both the meridian variation in the central power and asphericity. The variation with meridian in central power and asphericity also correlated. These correlations show that the biconic JCC description of corneal shape is useful to understanding refractive error variation in myopia and can be used to develop models as a function of myopia.

To create models that predicted asymmetrical aberrations, the symmetrical eye models were enhanced by misaligning their optical components and describing the shape of the anterior corneal surface with the biconic parameters as a function of myopia. Since the shape of the anterior corneal surface was now an anatomically more accurate function of myopia, the refractive error of the asymmetrical models was set by adjusting their axial length. A comparison to empirical results revealed that the dependence of the model's refractive error on axial length was anatomically accurate. It was also shown that adjusting the model's axial length accounted for two thirds of the change in refractive error and caused the model's high-order aberrations to decrease. Changing the shape of the anterior corneal surface as a function of refractive error accounted for a third of the predicted change in refractive error and was the primary source of the predicted increase in high-order aberrations. This proves that an average, anatomically accurate model must adjust both its anterior corneal surface and axial length to simulate myopia.

There was no difference in the aberrations predicted by the asymmetric models with a symmetrical conic cornea compared to those with a biconic anterior cornea with an average amount of asymmetry. Consequently the predicted asymmetrical aberrations resulted from the misalignment of the model's optical components.

Optical component misalignments were defined by the average of empirical measurements. An empirical wavefront defined by averaging the individual aberration terms contains less asymmetrical aberrations than individual subjects. The models, created by incorporating the average misalignments, underestimated the asymmetrical aberrations observed in the individual subjects but provided a good prediction of the average empirical aberrations.

Refractive surgery was modeled by changing the shape of the anterior corneal surface in the asymmetrical models with symmetrical corneas. Changes in corneal shape and aberrations of corresponding models defined by the Munnerlyn equations (1988) did not match empirical observations.

Clinically measured changes in the anterior corneal topography caused by a particular PRK surgery were determined by comparing pre and postoperative biconic JCC parameters. Significant correlations revealed that decreasing refractive error by laser ablation decreases the paraxial power of the anterior corneal surface and causes its asphericity to increase.

Postoperative models based on the clinically measured changes in the anterior corneal topography predicted that myopia would be corrected to near emmetropia and the high-order aberrations would substantially increase. The models' residual refractive error calculated from the corresponding Zernike term, did not predict the exact relationship between pre and postoperative refractive error that was observed for the post-PRK subjects and the difference between model predictions and empirical results increased for larger levels of high-order aberrations.

Empirical refractive error was measured by subjective refraction while the models' refractive error was calculated from the Zernike polynomial quantification of their wavefront error. It has been shown that refractive error estimates from Zernike polynomials do not predict subjective refractions and the error increased with higher levels of high-order aberrations (Guirao and Williams, 2003). This could account for the difference between the refractive error of the postoperative models and empirical results. A method of relating wavefront error to subjective refraction, based on retinal image characteristics would likely improve the estimate.

Despite the postoperative refractive error inadequacy, these models make a good prediction of the induced increase in high-order aberrations that have been observed after a similar type of

surgery. A postoperative eye model that incorporates a symmetrical conic cornea and average tilts and decentrations of its ocular components accurately predicts changes in aberrations as a result of broad beam PRK.

Average, anatomically accurate, GRIN eye models have been developed that accurately predict the average aberrations of emmetropic and low to moderate myopic young adults and are useful for investigating the average effects of procedures like laser refractive surgery. These models underestimate the asymmetrical and total high-order aberrations that have been measured in individual subjects. To predict individual aberrations will undoubtedly require individualized eye models. While average eye models will not be able to accurately predict the aberration of an individual eye, the models developed here provide a useful tool for vision research since they demonstrate correlations between changes in biometric parameters like corneal shape and wavefront aberrations.

Appendix A: GRIN Calculation in CodeV

To incorporate a gradient refractive index (GRIN) in Code V requires creating a specialized subroutine that calculates the refractive index as a function of position within the lens. The subroutine is written in C-code and must be stored in a file named usergrn.c. This appendix repeats the values of the GRIN parameters that were used throughout the thesis and includes the C-code.

A.1: GRIN Parameter Values

Nc: Core Index 1.406

Ns: Surface Index 1.377

b: Length of semi-axis in equatorial plane 4.6 mm

a: Length of semi-axis along the optical axis 1.49 mm anterior 2.31 mm posterior

These values can also be found in Table 3.2

A.2: C-code

Following is the contents of the file usergrn.c that was used to calculate the GRIN within Code V. This file is a modified version of an example that is included with Code V. Most of the comments originated in the example file and have only been modified slightly

```
/*
Purpose: Evaluates n and n*GRAD(n) of a user-defined index of refraction gradient.

The function is of the form n(x,y,z), where (x,y,z) are the cartesian coordinates
of a point in the gradient. The origin of this coordinate system is the vertex of the surface to which
the gradient is attached. GRAD(n) is the three derivatives of the function n, (dn/dx, dn/dy, dn/dz).

The GRIN equations given in Chapter 3 (3.3 & 3.4) utilize a coordinate system where the lens core
is situated at the origin. Since this was not consistent with how CodeV operates, that equation was
modified appropriately

Parameters: The following is a brief description of the parameters in the call list. If the parameter is
designated as "input", its value is passed to the subroutine by the calling program. If it is designated
as "output", its value is supposed to be calculated or set by this subroutine and passed back to the
calling program.
```

KERROR - Error code (output). This is set to zero before this subroutine is entered. If there are any error conditions which prevent normal completion of the calculation (e.g., negative SQRT, etc.), KERROR should be set to a non-zero value.

BRIND - The base index (input). This is entered in the private catalog as the index of refraction.

COEF - The gradient coefficients (input). See Table 3.2 or section A.1. These are entered in the private catalog as the coefficients.
coef[1] = surface index
coef[2] = length of semi-minor axis (optical axis)
coef[3] = flag to determine front or back side of lens
flag >=0 for front side of lens, otherwise back side

S - The position vector (input). S is an array containing the three components (X,Y,Z) of the position of a ray as it is traced. Z is the optical axis.

RINDEX - The calculated index of refraction (output). This is the calculated value of the index of refraction at S using the equation programmed in this subroutine.

XNGRAN - The calculated n*GRAD(n) (output). XNGRAN is an array containing the three components of the calculated values of n*GRAD(n) at S using the equation programmed in this subroutine. Since n*GRAD(n) is equivalent to 0.5*GRAD(n**2), either form can be used, depending on which is more convenient.

*/

```
#include <math.h>

#ifdef sun
# define USERGRN usergrn_
#else
# define USERGRN usergrn
#endif

void usergrn(kerror, brind, coef, s, rindex, xngran)
int    *kerror;
double *brind;
double *coef, *s, *rindex, *xngran;
{
        const double b = 4.6;   //length of semi-major axis in equatorial plane

        static double No, Ns, a, flag;
        static double x, y, z;
        static double A, Ks, K;
        static double b2, a2, r2;
        static double z2, temp;
```

```
--xngran;
--s;
--coef;

*kerror = 0;

// input from private catalog
No = *brind;   // core index
Ns = coef[1];   // surface index
a = coef[2];      // length of semi-minor axis (optical axis)
flag = coef[3]; // >=0 - front side of lens, otherwise back side

if ( a == (double)0 )     // check for division by zero
{
        *kerror = 1;
        return;
}

b2 = pow(b,2);            // pow(x,y) calculates x to the power of y
a2 = pow(a,2);
x = s[1];
y = s[2];
r2 = pow(x,2) + pow(y,2);

// origin of equations not same as CodeV's
// fix origin of system depending on side of lens
if ( flag >= (double)0 )
        z = s[3] - a;
else
        z = s[3];

z2 = pow(z,2);

A = ( No - Ns ) / b2;
Ks = b2 / a2 - 1;         //Ks is also surface asphericity
K = Ks * ( z2 / a2 + r2 / b2 );

*rindex = No - A * ( ( 1 + K ) * z2 + r2 );

// N*Grad(N)

temp = Ks * z2 / b2 + 1;
xngran[1] = *rindex * ( -2 * A * x * ( temp ) );
xngran[2] = *rindex * ( -2 * A * y * ( temp ) );
temp = Ks * z2 / a2 + 1;
xngran[3] = *rindex * ( -2 * A * z * ( temp + K ) );

}
```

References

Ames, A. and Proctor, C. (1921) Dioptrics of the eye. *J. Opt. Soc. Am.,* 11**,** 22-85.

Amoils, S.P. (1999) Using a nidek excimer laser with a rotary epithelial brush and corneal chilling: Clinical results. *J Cataract Refract Surg,* 25**,** 1321-1326.

Applegate, R., Nunez, R., Buettner, J. and Howland, H. (1995) How accurately can videokeratographic systems measure surface elevation. *Optom Vis Sci,* 72**,** 785 - 792.

Artal, P., Marcos, S., Iglesias, I. and Green, D.G. (1996) Optical modulation transfer function and contrast sensitivity with decentered small pupils. *Vision Res.,* 6**,** 3575-3586.

Atchison, D.A. (1985) Modern optical design assessment and spectalce lenses. *Optica Acta,* 32**,** 607-634.

Atchison, D.A. and Smith, G. (2000) *Optics of the human eye*. Butterworth-Heineman, Oxford.

Barry, J.C., Effert, R., Kaupp, A. and Burhoff, A. (1994a) Measurement of ocular alignment with photographic purkinje i and iv reflection pattern evaluation. *Invest Ophthalmol Vis Sci,* 35**,** 4219-4235.

Barry, J.C., Effert, R., Reim, M. and Meyer-Ebrecht, D. (1994b) Computational principles in purkinje i and iv reflection pattern evaluation for the assessment of ocular alignment. *Invest Ophthalmol Vis Sci,* 35**,** 4205-4218.

Belin, M.W. and Misery, J.J. (1999) Technologies for corneal topography. In *Refractive surgery*(Eds, H.K. Wu, V.M. Thompson, R.F. Stienert, et al.) Thieme, New York, pp. 63-78.

Bennett, A.G. and Rabbetts, R.B. (1988) Schematic eyes - time for a change? *Optician,* 196**,** 14-15.

Bennett, A.G. and Rabbetts, R.B. (1989) *Clinical visual optics*. Butterworths-Heinemann, Oxford.

Bing, L. and Campbell, M.C.W. (1994) The change in monochromatic aberrations with lens tilt and decentration in a four aspheric surface model eye. *Invest. Ophthalmol. Visual Sci. (Suppl.),* 35**,** S1803.

Blaker, J.W. (1980) Towards an adaptive model of the human eye. *J. Opt. Sci. Am.,* 70**,** 220-223.

Born, M. and Wolf, E. (1999) *Principles of optics*. University Press, Cambridge.

Brenner, D. (1997) Modeling the cornea with the topographic modeling system videokeratoscope. *Optom Vis Sci,* 11**,** 895-898.

Brown, N. (1974) The change in lens curvature with age. *Exp Eye Res,* 19**,** 175-183.

Brunnette, I., Gresset, J., Boivin, J.F. and al., e. (2000) Functional outcome and satsifaction after photorefractive keratectomy. Part 2: Survey of 690 patients. *Ophthalmology,* 107**,** 1790-1796.

Budak, K., Khater, T., Friedman, T., Holladay, J. and Koch, D. (1999) Evaluation of relationships among refractive and topographic parameters. *J Cataract Refract Surg,* 25**,** 814-820.

Bueno, J.M., King, D., Campbell, M.C.W. and Simonet, P. (2002) Myopia and monochromatic aberrations in young adult subjects. *Vision Res.,* submitted

Cairns, G., McGhee, C.N.J., Collins, M.J., Owens, H. and Gamble, G.D. (2002) Accuracy of orbscan ii slit-scanning elevation topography. *J Cataract Refract Surg,* 28**,** 2181-2187.

Calver, R., Cox, M. and Elliott, D. (1999) Effect of aging on the monochromatic aberrations of the human eye. *J. Opt. Soc. Am. A,* 16**,** 2069-2078.

Campbell, M.C. (1984) Measurement of refractive index in an intact crystalline lens. *Vision Res.,* 5**,** 409-415.

Campbell, M.C., Bueno, J.M., Hunter, J.J. and Kisilak, M.L. (2003) Ophthalmic lens effects in hartmann-shack measurements. *Journal of Vision,* 3**,** 29.

Campbell, M.C.W. and Hughes, A. (1981) An analytic, gradient index schematic lens and eye for the rat which predicts aberrations for finite pupils. *Vision Res.,* 21**,** 1129-48.

Campbell, M.C.W., Harrison, E.M. and Simonet, P. (1990) Psychophysical measurement of the blur on the retina due to optical aberrations of the eye. *Vision Res.,* 30**,** 1587-1602.

Campbell, M.C.W., Haman, H., Simonet, P. and Brunnette, I. (1998) Optical image quality in eyes after excimer laser photorefractive keratectomy (prk). *Invest Ophthalmol Vis Sci,* 39**,** S466.

Carney, L.G., Mainstone, J. and Henderson, B. (1997) Corneal topography and myopia. *Invest Ophthalmol Vis Sci,* 38**,** 311-320.

Casson, E.J., Jackson, W.B. and Minsioulis, G. (1995) High and low contrast acuity following excimer photorefractive keratectomy. In *Vision science and its applications*, Vol. 1 Optical Society of America Technical Digest Series, Washington DC, pp. 45-48.

Castejon-Mochon, J., Lopez-Gill, N., Benito, A. and Artal, P. (2002) Ocular wave-front aberration statistics in a normal young population. *Vision Res.,* 42**,** 1611-1617.

Charman, W. (1991a) Wavefront aberration of the eye: A review. *Optom Vis Sci,* 68**,** 574-583.

Charman, W.N. and Walsh, G. (1985) The optical phase transfer function of the eye and the perception of spatial phase. *Vision Res.,* 25**,** 619-623.

Charman, W.N. (1991b) Optics of the human eye. In *Visual optics and instrumentation*, Vol. 1 (Ed, W.N. Charman) CRC Press, Boca Raton, pp. 449.

Cheng, X., Bradley, A., Hong, X. and Thibos, L.N. (2003) Relationship between refractive error and monochromatic aberrations of the eye. *Optom Vis Sci,* 80**,** 43-49.

Cho, P., Lam, A.K.C., Mountford, J. and Ng, L. (2002) The performance of four different corneal topographers on normal human corneas and its impact on orthokeratology lens fitting. *Optom Vis Sci,* 79**,** 175-183.

Clarke, R.C., Campbell, M.C.W. and Piers, P. (1998) Dependence of the refractive index in the human crystalline lens on age and time post-mortem. *Invest Ophthalmol Vis Sci,* 39**,** S1091.

Collins, M., Wildsoet, C. and Atchinson, D. (1995) Monochromatic aberrations and myopia. *Vision Res.,* 35**,** 1157-1163.

Cui, C. (1998) *The misalignment of ocular components and ocular monochromatic aberrations*. Thesis (Ph.D.). University of Waterloo.

Douthwaite, W.A., Hough, T., Edwards, K. and Notay, H. (1999) The eyesys videokeratoscopic assessment of apical radius and p-value in the normal human cornea. *Ophthal Physiol Opt,* 19**,** 467-474.

Douthwaite, W.A. (2003) The asphericity, curvature and tilt of the human cornea measured using a videokeratoscope. *Ophthal Physiol Opt,* 23**,** 141-150.

Drasdo, N. and Fowler, C.W. (1974) Non-linear projection of the retinal image in a wide-angle schematic model. *Br. J. Ophthalmol.,* 58**,** 709-714.

Dubbelman, M. and van der Heijde, G. (2001) The shape of the aging human lens:Curvature, equivalent refractive index and the lens paradox. *Vision Res.,* 41**,** 1867-1877.

Dubbelman, M., van der Heijde, G. and Weeber, H. (2001) The thickness of the aging human lens obtained from corrected scheimpflug images. *Optom Vis Sci,* 78**,** 411-416.

Dubbelman, M., Weeber, H., van der Heijde, R. and Volker-Dieben, H. (2002) Radius and asphericity of the posterior corneal surface determined by corrected scheimpflug photography. *Acta. Ophthalmol. Scand.,* 80**,** 379-383.

Duke-Elder, S. and Abrams, D. (1970) Opthalmic optics and refraction. In *System of ophthalmology*, Vol. 5 Kimpton, London.

Dunne, M.C.M., Royston, J.M. and Barnes, D.A. (1992) Normal variations of the posterior corneal curvature. *Acta Ophthalmologica,* 70**,** 255-261.

El Danasoury, M.A., Maghraby, A.E., Klyce, S.D. and Mehrez, K. (1999) Comparison of photorefractive keratectomy with excimer laser in situ keratomileusis in correcting low myopia (from -2.00 to -5.50 diopters). A radomized study. *Ophthalmology,* 106**,** 411-421.

Emsley, H.H. (1952) *Visual optics*. Hatton, London.

Fincham, W.H.A. and Freeman, M.H. (1980) *Optics*. Butterworths, London.

Fontana, S.T. and Brubaker, R.F. (1980) Volume and depth of the anterior chamber in the normal aging human eye. *Arch. Ophthalmol.,* 98**,** 1803-1808.

Francon, M. (1951) Aberration spherique chromatisme et pouvoir separateur de l'oel. *Rev. Opt.,* 30**,** 71-80.

Garner, L., Meng, C., Grosvenor, T. and Mohidin, N. (1990) Ocular dimensions and refractive power in malay and melanesian children. *Ophthal Physiol Opt,* 10**,** 234-238.

Garrison, B.J. and Srinivasan, R. (1985) Laser ablation of organic polymers: Microscopic models for photochemical and thermal process. *J. Applied Phys.,* 57**,** 2909-2914.

Gatinel, D., Hoang-Xuan, T. and Azar, D.T. (2001) Determination of the corneal asphericity after myopia surgery with the excimer laser: A mathematical model. *Invest Ophthalmol Vis Sci,* 442**,** 1736-1742.

Glasser, A. and Campbell, M.C.W. (1998) Presbyopia and the optical changes in the human crystalline lens with age. *Vision Res.,* 38**,** 209-229.

Glasser, A. and Campbell, M.C.W. (1999) Biometric, optical and physical changes in the isolated human crystalline lens with age in relation to presbyopia. *Vision Res.,* 39**,** 1991-2015.

Goh, W. and Lam, C. (1994) Changes in refractive trends and optical components of hong kong chinese aged 19-39 years. *Ophthal Physiol Opt,* 14**,** 378-382.

Goss, D., Cox, V., Herrin-Lawson, G., Nielsen, E. and Dolton, W. (1990) Refractive error, axial length, and height as a function of age in young myopes. *Optom Vis Sci,* 67

Goss, D.A., van Veen, H.G., Rainey, B.B. and Feng, B. (1997) Ocular components measured by keratometry, phakometry, and ultrasoonography in emmetropic and myopic optometry students. *Optom Vis Sci,* 74**,** 489-495.

Grosvenor, T. (1987) Reduction in axial length with age: An emmetropizing mechanism for the adult eye? *Am J Optom Physiol Opt,* 64**,** 657-663.

Grosvenor, T. and Scott, R. (1994) Role of the axial length/corneal radius ratio in determining the refractive state of the eye. *Optom Vis Sci,* 71**,** 573-579.

Guillon, M., Lydon, D.P.M. and Wilson, C. (1986) Corneal topography: A clinical model. *Ophthal Physiol Opt,* 6**,** 47-56.

Guirao, A. and Artal, P. (2000) Corneal wave aberration from videokeratography: Accuracy and limitations of the procedure. *J. Opt. Soc. Am. A,* 17**,** 955-965.

Guirao, A., Redondo, M. and Artal, P. (2000) Optical aberrations of the human cornea as a function of age. *J. Opt. Soc. Am. A,* 17**,** 1697-1702.

Guirao, A. and Williams, D.R. (2003) A method to predict refractive errors from wave aberration data. *Optom Vis Sci,* 80**,** 36-42.

Gullstrand, A. (1924) Appendices. In *Physiological optics*, Vol. 1 (Ed, H. Helmholtz) Optical Society of America, Rochester.

Hadden, O.B., Ring, C.P., Morris, A.T., Elder, M.J. and al., e. (1999) Visual, refractive, and subjective outcomes after photorefractive keratectomy for myopia of 6 to 10 diopters using the nidek laser. *J Cataract Refract Surg,* 25**,** 936-942.

Harris, W.F. (1990) Statistical inference on mean dioptric power:Hypothesis testing and confidence regions. *Ophthal Physiol Opt,* 10**,** 363-372.

Harris, W.F. (1991) Representation of dioptric power in euclidean 3-space. *Ophthal Physiol Opt,* 11**,** 130-136.

Harris, W.F. (1992) Testing hypotheses on dioptric power. *Optom Vis Sci,* 69**,** 835-845.

Hayashi, K., Hayashi, H., Oshika, T. and Hayashi, F. (2000) Fourier analysis of irregular astigmastism after implantation of 3 types of intraocular lenses. *J Cataract Refract Surg,* 26**,** 1510-1516.

He, J.C., Gwiazada, J.E., Held, R., Thorn, F., Ong, E. and Marran, L. (2000) Wave-front aberrations in the eyes of myopic and emmtropic school children and young adults. *Proceedings of the VIII International Conference on Myopia***,** 113-116.

Hersh, P., Shah, S. and Holladay, J. (1996) Corneal asphericity following excimer laser photorefractive keratectomy. *Ophthalmic and Surgical Lasers,* 27**,** S421-S428.

Hersh, P.S., Brint, S.F., Maloney, R.K. and al., e. (1998) Photorefractive keratectomy versus laser in situ keratomeliusis for moderate to high myopia. *Ophthalmology,* 105**,** 1512-1523.

Hilmantel, G., Blunt, R.J., Garret, B.P., Howland, H.C. and Applegate, R.A. (1999) Accuracy of the tomey topographic modeling system in measuring surface elevations of asymmetric objects. *Optom Vis Sci,* 76**,** 108-114.

Hjortdal, J., Erdmann, L. and Bek, T. (1995) Fourier analysis of video-keratographic data. A tool for the separation of spherical, regular astigmatic and irregular astigmatic corneal power components. *Ophthal Physiol Opt,* 15**,** 171-185.

Horner, D., Soni, P.S., Vyas, N. and Himebaugh, N. (2000) Longitudinal changes in corneal asphericity in myopia. *Optom Vis Sci,* 77**,** 198-203.

Horner, D., Foster, C., Thibos, L.N., Goss, D.A. and Martin, J. (2003) New thoughts on the correlation of astigmatism to spherical ametropia.

Howcroft, M.J. and Parker, J.A. (1977) Aspheric curvatures for the human lens. *Vision Res.,* 17**,** 1217-1223.

Howland, H. and Howland, B. (1977) A subjective method for the measurement of monochromatic aberrations of the eye. *J. Opt. Soc. Am. A,* 67**,** 1508-1518.

Iskander, D.R., Collins, M.J. and Davis, B. (2001a) Optimal modeling of the corneal surfaces with zernike polynomials. *IEEE Trans Biomed Eng,* 48**,** 87-95.

Iskander, D.R., Morelande, M.R., Collins, M.J. and Davis, B. (2002) Modeling of corneal surfaces with radial polynomials. *IEEE Trans Biomed Eng,* 49**,** 320-328.

Iskander, R., Collins, M., Davis, B. and Franklin, R. (2001b) Corneal surface characterization: How many zernike terms should be used? *Invest Ophthalmol Vis Sci,* 42**,** S896.

Ivanoff, A. (1956) About the spherical aberration of the eye. *J. Opt. Sci. Am.,* 46**,** 901-903.

Jackson, W.B. (2001) Photorefractive keratectomy: Indications, surgical techniques, complications, and results. *Ophthalmic Practice,* 19**,** 18-30.

Jalie, M. (1984) *The principles of ophthalmic lenses.* The Association of Dispensing Opticians, London.

Kamiya, K., Oshika, T., Amano, S., Takahasi, T., Tokunaga, T. and Miyata, K. (2000) Influence of the excimer laser photorefractive keratectomy on the posterior corneal surface. *J Cataract Refract Surg,* 26**,** 867-871.

Kapadia, M.S. and Wilson, S.E. (2000) One-year results of prk in low and moderate myopia: Fewer than 0.5% of eyes lose two or more lines of vision. *Cornea,* 19**,** 180-184.

Keller, P.R., McGhee, C.N.J. and Weed, K.H. (1998) Fourier analysis of corneal topography data after photorefractive keratectomy. *J Cataract Refract Surg,* 24**,** 1447-1455.

Kiely, P.H., Smith, G. and Carney, G. (1982) The mean shape of the human cornea. *Opt. Acta,* 29**,** 1027-1040.

Kolb, H., Fernandez, E. and Nelson, R. (2002) www.webvision.med.utah.edu.

Kooijman, A.C. (1983) Light distribution on the retina of a wide angle theoretical eye. *J. Opt. Sci. Am.,* 73**,** 1544-1550.

Koomen, M., Tousey, R. and Scolnik, R. (1949) The spherical aberration of the eye. *J. Opt. Sci. Am.,* 39**,** 370-376.

Kortez, J.F., Kaufman, P.L., Neider, M.W. and Goeckner, P.A. (1989) Accommodation and presbyopia in the human eye - aging of the anterior segment. *Vision Res.,* 29**,** 1685-1692.

Lam, A.K.C. and Douthwaite, W.A. (1997) Measurement of posterior corneal asphericity on hong kong chinese: A pilot study. *Ophthal Physiol Opt,* 17**,** 348-356.

Langenbucher, A., Seitz, B., Kus, M.K. and Naumann, G.O.H. (1999) Zernike representation of corneal topographic height data after nonmechanical penetrating keratoplasty. *Invest Ophthalmol Vis Sci,* 40**,** 582-591.

Langenbucher, A., Sauer, T. and Seitz, B. (2002a) Wavelet analysis for corneal topographic surface characterization. *Current Eye Research,* 24**,** 409-421.

Langenbucher, A., Seitz, B. and Naumann, G.O.H. (2002b) Three-axis ellipsoidal fitting of videokeratoscopic height data after penetrating keratoplasty. *Current Eye Research,* 24**,** 422-429.

Langenbucher, A., Viestenz, A. and Seitz, B. (2002c) Conoidal fitting of corneal topography height data after excimer laser penetrating keratoplasty. *J. Refractive Surg.,* 18**,** 63-71.

Le Grand, Y. and El Hage, S.G. (1980) *Physiological optics.* Springer-Verlag, Berlin.

Liou, H.L. and Brennan, N.A. (1996) The prediction of spherical aberration with schematic eyes. *Ophthal Physiol Opt,* 16**,** 348-354.

Liou, H.L. and Brennan, N.A. (1997) Anatomically accurate, finite model eye for optical modeling. *J. Opt. Soc. Am. A,* 14**,** 1684-1695.

Liu, Z., Huang, A. and Pflugfelder, S. (1999) Evaluation of corneal thickness and topography in normal eyes using the orbscan corneal topography system. *Br. J. Ophthalmol.,* 83**,** 774-778.

Long, W.F. (1982) Why is ocular astigmatism regular? *Am J Optom Physiol Opt,* 59**,** 520-522.

Lotmar, W. (1971) Theoretical eye model with aspherics. *J. Opt. Sci. Am.,* 61**,** 510-513.

Lowe, R.F. and Clark, B.A. (1973) Posterior corneal curvature. *Br. J. Ophthalmol.,* 57**,** 464-470.

MacRae, S.M., Schwiegerling, J.T. and Snyder, R. (1999) Customized and low spherical aberration corneal ablation design. *J. Refractive Surg.,* 15**,** S246-S248.

MacRae, S.M. (2000) Supernormal vision, hypervision and customized corneal ablation. *J Cataract Refract Surg,* 26**,** 154-157.

Marcos, S., Moreno-Barriuso, E., Llorente, L., Navarro, R. and Barbero, S. (2000) Do myopic eyes suffer from larger amounts of aberrations? *Proceedings of the VIII International Conference on Myopia,*

Marcos, S., Barbero, S., Llorente, L. and Merayo-Lloves, J. (2001a) Optical response to lasik surgery for myopia from total and corneal aberration measurements. *Invest Ophthalmol Vis Sci,* 42**,** 3349-3356.

Marcos, S., Burns, S.A., Prieto, P.M., Navarro, R. and Baraibar, B. (2001b) Investigating sources of variability of monochromatic and transverse chromatic aberrations across eyes. *Vision Res.,* 41**,** 3861-3871.

Martinez, C., Applegate, R., Klyce, S., McDonald, M.B., Medina, J. and Howland, H. (1998) Effect of pupillary dilation on corneal optical aberrations after photorefractive keratectomy. *Arch. Ophthalmol.,* 116**,** 1053-1062.

McDonald, M.B., Dietz, M.R., Frantz, J.M. and al., e. (1999) Photorefractive keratectomy for low to moderate myopia and astigmatism with a small-beam, tracker directed excimer laser. *Ophthalmology,* 106**,** 1481-1488.

McLellan, J.S., Marcos, S. and Burns, S.A. (2001) Age-related changes in monochromatic wave aberrations of the human eye. *Invest Ophthalmol Vis Sci,* 42**,** 1390-1395.

Mejia-Barabosa, Y. and Malacara-Hernandez, D. (2001) A review of the methods for measuring corneal topography. *Optom Vis Sci,* 78**,** 240-253.

Mierdel, P., Kaemmerer, M., Krinke, H. and Seiler, T. (1999) Effects of photorefractive keratectomy and cataract surgery on ocular optical errors of higher order. *Graefe's Arch Clin Exp Ophthalmology,* 237**,** 725-729.

Millodot, M. and Sivak, J. (1979) Contribution of the cornea and lens to the spherical aberration of the eye. *Vision Res.,* 19**,** 685-687.

Moffat, B.A., Atchinson, D.A. and Pope, J.M. (2002) Age-related changes in the refractive index distribution and power of the human lens as measured by magnetic resonance microimaging in vitro. *Vision Res.,* 42**,** 1683-1693.

Moreno-Barriuso, E., Merayo-Lloves, J., Marcos, S., Navarro, R., Llorente, L. and Barbero, S. (2001) Ocular aberrations before and after myopic corneal refractive surgery: Lasik-induced changes measured with laser ray tracing. *Invest Ophthalmol Vis Sci,* 42**,** 1396-1403.

Mrochen, M., Kaemmerer, M. and Seiler, T. (2001) Clinical results of wavefront-guided laser in situ keratomileusis 3 months after surgery. *J Cataract Refract Surg,* 27**,** 201-207.

Munger, R. (2001) The impact of the posterior corneal surface shape on the wavefront aberrations of the cornea following refractive surgery. *Invest Ophthalmol Vis Sci,* 42**,** S529.

Munnerlyn, C.R., Koons, S. and Marshall, J. (1988) Photorefractive keratectomy: A technique for laser refractive surgery. *J Cataract Refract Surg,* 14**,** 46-52.

Naroo, S. and Charman, W. (2000) Changes in the posterior corneal curvature after photorefractive keratectomy. *J Cataract Refract Surg,* 26**,** 872-878.

Navarro, R., Santamaria, J. and Bescos, J. (1985) Accommodation-dependent model of the human eye with aspherics. *J. Opt. Soc. Am. A,* 8**,** 1273-1281.

O'Brart, D. and Marshall, J. (1999) Background of excimer laser refractive surgery. In *Refractive surgery*(Eds, H. Wu, V. Thompson, R. Steinert, et al.) Thieme, New York, pp. 217-224.

Ogle, K.N. (1968) *Optics.* Thomas, Springfiled, IL.

Oliver, K., Hemenger, R., Corbett, M., O'Brart, D., Verma, S., Marshall, J. and Tomlinson, A. (1997) Corneal optical aberrations induced by photorefractive keratectomy. *J. Refractive Surg.,* 13**,** 246-254.

Olsen, T., Dam-Johnson, M., Bek, T. and Hjortdal, J. (1996) Evaluating surgically induced astigmatism by fourier analysis of corneal topography data. *J Cataract Refract Surg,* 22**,** 318-323.

Oshika, T., Tomidokoro, A., Maruo, K., Tokunaga, T. and Miyata, N. (1998) Quantitative evaluation of irregular astigmatism by fourier series harmonic analysis of videokeratographic data. *Invest Ophthalmol Vis Sci,* 39**,** 705-709.

Oshika, T., Klyce, S.D., Applegate, R.A. and Howland, H.C. (1999) Changes in corneal wavefront aberrations with aging. *Invest Ophthalmol Vis Sci,* 40**,** 1351-1355.

Pallikaris, I.G., Koufala, K.I., Siganos, D.S. and al., e. (1999) Photorefractive keratectomy with a small spot laser and tracker. *J. Refractive Surg.,* 15**,** 137-144.

Paquin, M., Haman, H. and Simonet, P. (2002) Objective measurement of optical aberrations in myopic eyes. *Optom Vis Sci,* 79**,** 285-291.

Pardhan, S. and Beesley, J. (1999) Measurment of the corneal curvature in young and older normal subjects. *J. Refractive Surg.,* 15**,** 469-474.

Patel, S., Marshall, J. and Fitzke, F.W. (1993) Shape and radius of the posterior corneal surface. *Refract. Corneal Surg.,* 9**,** 173-181.

Piers, P. (1997) *Gradient index optical models and spherical aberration of the human crystalline lens*. Thesis (M.Sc.). University of Waterloo.

Pierscionek, B.K. and Chan, D.Y.C. (1989) Refractive index gradient of human lenses. *Optom Vis Sci,* 66**,** 822-829.

Pierscionek, B.K. (1994) Refractive index of the human lens surface measured with a optical fibre sensor. *Opthal Res,* 26**,** 32-35.

Pierscionek, B.K. (1995) Variations in refractive index and absorbance of 670 nm light with age and cataract formation in human lenses. *Exp Eye Res,* 60**,** 407-414.

Pierscionek, B.K. (1997) Refractive index contours in the human lens. *Exp Eye Res,* 64**,** 887-893.

Pomarantzeff, O., Govignon, J. and Schepens, C.I. (1972) Wide-angle optical models of the eye. *Optica Acta,* 19**,** 387-388.

Pomarantzeff, O., Dufault, P. and Goldstein, R. (1983) Wide-angle optical model of the eye. In *Advances in diagnostic visual optics*(Eds, G.M. Breinin and I.M. Siegel) Springer, Berlin, pp. 12-21.

Pop, M. and Payette, Y. (2000) Photorefractive keratectomy versus laser in situ keratomileusis. *Ophthalmology,* 107**,** 251-257.

Porter, J., Guirao, A., Cox, I. and Williams, D.R. (2001) Monochromatic aberrations of the human eye in a large population. *J. Opt. Soc. Am. A,* 18**,** 1793-1803.

Preussner, P., Wahl, J. and Kramann, C. (2003) Corneal model. *J Cataract Refract Surg,* 29**,** 471-477.

Priest, D. and Munger, R. (1998) Comparative study of the elevation topography of complex shapes. *J Cataract Refract Surg,* 24**,** 741-750.

Raasch, T.W. (1995) Corneal topography and irregular astigmatism. *Optom Vis Sci,* 11**,** 809-815.

Rivett, A.G. and Ho, A. (1991) The posterior corneal topography. *Invest. Ophthalmol. Visual Sci. (Suppl.),* 32**,** 1001.

Roberts, C. (1994) Characterization of the inherent error in a spherically-biased corneal topography system in mapping a radially aspheric surface. *Refract. Corneal Surg.,* 10**,** 103-116.

Roberts, C. (1996) Corneal topography: A review of terms and concepts. *J Cataract Refract Surg,* 22**,** 624-629.

Roberts, C. (2002) Biomechanics of the cornea and wavefront-guided laser refractive surgery. *J. Refractive Surg.,* 18**,** S589-S592.

Royston, J.M., Dunne, M.C.M. and Barnes, D.A. (1990) Measurement of the posterior corneal radius using slit lamp and purkenje image techniques. *Ophthal Physiol Opt,* 10**,** 385-388.

Rubin, M.L. (1993) *Optics for clinicians.* Triad, Gainsville, FL.

Schober, H., Munker, H. and Zollies, F. (1968) Die aberration des menschlichen auges und ihre messung. *Optica Acta,* 15**,** 47-57.

Schwiegerling, J.T., Greivenkamp, J.E. and Miller, J.M. (1995) Representation of videokeratoscopic height data with zernike polynomials. *J. Opt. Soc. Am. A,* 12**,** 2105-2113.

Schwiegerling, J.T., Greivenkamp, J.E., Miller, J.M. and al., e. (1996) Optical modeling of the radial keratotomy incision patterns. *Amer. J. Ophthalmol.,* 122**,** 808-817.

Schwiegerling, J.T. and Snyder, R. (1998) Custom photorefractive keratectomy ablations for the correction of spherical and cylindrical refractive error and higher-order aberration. *J. Opt. Soc. Am. A,* 15**,** 2572-2579.

Schwiegerling, J.T. and Snyder, R. (2000) Corneal ablation patterns to correct for spherical aberration in photorefractive keratectomy. *J Cataract Refract Surg,* 26**,** 214-221.

Seiler, T., Kaemmerer, M., Mierdel, P. and Krinke, H. (2000) Ocular optical aberrations after photorefractive keratectomy for myopia and myopic-astigmatism. *Arch. Ophthalmol.,* 118**,** 17-21.

Seitz, B., Torres, B., Langenbucher, A., Behrens, A. and Suarez, E. (2001) Posterior corneal curvature changes after myopic laser in situ keratomileusis. *Ophthalmology,* 108**,** 666-673.

Smith, G., Pierscionek, B.K. and Atchinson, D.A. (1991) The optical modelling of the human lens. *Ophthal Physiol Opt,* 11**,** 359-369.

Smith, G. and Atchison, D.A. (1997) *The eye and visual optical instruments.* Cambridge University Press, Cambridge.

Smith, G. (2003) The optical properties of the crystalline lens and their significance. *Clin Exp Optom,* 86**,** 3-18.

Smith, W. (2000) *Modern optical engineering.* McGraw-Hill, New York.

Smolek, M.K. and Klyce, S.D. (2003) Zernike polynomial fitting fails to represent all visually significant corneal aberrations. *Invest Ophthalmol Vis Sci,* 44**,** 4676-4681.

Swinger, C.A. (1999) Background of lamellar refractive surgery. In *Refractive surgery*(Eds, H.K. Wu, V.M. Thompson, R.F. Stienert, et al.) Thieme, New York, pp. 371-391.

Thibos, L.N., Ye, M., Zhang, X.X. and Bradley, A. (1992) The chromatic eye: A new reduced-eye model of ocular chromatic aberration in humans. *Appl. Opt.,* 31**,** 3594-3600.

Thibos, L.N., Ye, M., Zhang, X.X. and Bradley, A. (1993) In *Opt. Photon. News*, Vol. 4.

Thibos, L.N., Wheeler, W. and Horner, D. (1994) A vector method for the analysis of astigmatic refractive error. In *Vision Science and Its Application*, Vol. 2 Optical Society of America, pp. 14-17.

Thibos, L.N., Ye, M., Zhang, X. and Bradley, A. (1997) Spherical aberration of the reduced schematic eye with elliptical refracting surface. *Optom Vis Sci,* 74**,** 548-556.

Thibos, L.N., Applegate, R.A., Schwiegerling, J.T. and Webb, R. (2002) Standards for reporting optical aberrations of the eye. *J. Refractive Surg.,* 18**,** S652 - S660.

Thorton, S.P. (1999) Background of incisional refractive surgery. In *Refractive surgery*(Eds, H.K. Wu, V.M. Thompson, R.F. Stienert, et al.) Thieme, New York, pp. 127-134.

Tscherning, M. (1924) *Physiologic optics.* Keystone Publishing Co., Philadelphia.

van Alphen, G. (1961) On emmetropia and ametropia. *Opthalmologica,* 142(Suppl.)**,** 1-92.

Van Meeteren, A. (1974) Calculations of the optical modulation transfer function of the human eye for white light. *Optica Acta,* 21**,** 395-412.

Van Meeteren, A. and Dunnewold, C.J.W. (1983) Image quality of the human eye for eccentric pupils. *Vision Res.,* 23**,** 573-579.

Vaughan, D., Asbury, T. and Riordan-Eva, P. (1999) *General ophthalmology.* Appleton & Lange, London.

Verdon, W., Bullimore, M. and Maloney, R.K. (1996) Visual perfromance after photorefractive keratectomy. *Arch. Ophthalmol.,* 114**,** 1465-1472.

Walsh, G. and Charman, W. (1985) Measurement of the axial wavefront aberration of the human eye. *Ophthal Physiol Opt,* 5**,** 23-31.

Walsh, G. (1988) The effect of mydriasis on the pupillary centration of the human eye. *Ophthal Physiol Opt,* 8**,** 178-182.

Walsh, G. and Charman, W.N. (1988) The effect of pupil centration and diameter on ocular performance. *Vision Res.,* 28**,** 659-665.

Watkins, R.D. (1972) *A finite aperture model of the optical system of the human eye.* Thesis (PhD). Flinders University.

Welford, W.T. (1986) *Aberrations of optical systems.* Adam Hilger, Bristol.

Wilson, M.A., Campbell, M.C.W. and Simonet, P. (1992) Change in pupil centration with change in illumination and pupil size. *Optom Vis Sci,* 69**,** 129-136.

Yang, Y., Thompson, K. and Burns, S.A. (2002) Pupil location under mesopic, photopic, and pharmacologically dilated conditions. *Invest Ophthalmol Vis Sci,* 43**,** 2508-2512.

Ye, N., Zhang, X.X., Thibos, L.N. and Bradley, A. (1993) A new single-surface model eye that accurately predicts chromatic and spherical aberrations of the human eye. *Invest. Ophthalmol. Visual Sci. (Suppl.),* 34**,** 777.

Zadok, D., Haviv, D., Vishnevskia-Dia, V. and al., e. (1998) Excimer laser photoastigmatic refractive keratectomy: Eighteen-month follow-up. *Ophthalmology,* 105**,** 620-623.